DESIGN AND CHARACTERIZATION

OF

LOW-COST KA-BAND AMPLIFIER ANTENNA ARRAYS

by

TODD STEVEN MARSHALL

B.S., University of Colorado at Boulder, 1992

M.S., University of Colorado at Boulder, 1996

A thesis submitted to the

Faculty of the Graduate School of the

University of Colorado in partial fulfillment

of the requirements for the degree of

Doctor of Philosophy

Department of Electrical and Computer Engineering

2000

This thesis entitled:

Design and Characterization of Low-Cost Ka-band Amplifier Antenna Arrays

written by Todd Steven Marshall

has been approved for the Department of Electrical and Computer Engineering

Zoya Popović

Edward F. Kuester

Date

The final copy of this thesis has been examined by the

signators, and we find that both the content and the form

meet acceptable presentation standards of scholarly work in

the above mentioned discipline.

Marshall, Todd Steven (Ph.D., Electrical Engineering)

Design and Characterization of Low-Cost Ka-band Amplifier Antenna Arrays

Thesis directed by Professor Zoya Popović

Quasi-optical (QO) amplifiers combine the output powers of multiple low-power amplifiers in free-space to achieve higher output RF power levels. The benefit of QO amplifiers over corporate power combiners, which use guided waves, is that the power combining efficiency is theoretically independent of the number of devices. Therefore, a large number of devices can be combined efficiently.

In this thesis, several Ka-band (30 GHz) QO amplifier arrays for power combining applications are designed, fabricated, and characterized. The design of the QO amplifier includes: MMIC choice; thermal considerations; antenna choice and design; array layout; DC bias effects; mutual coupling effects; fabrication complexity; and total amplifier cost. Each array fabricated at the University of Colorado takes approximately eight weeks to complete and costs approximately three thousand dollars. Based on the variations in designs, a series of characterization measurements are completed which form the basis of fundamental studies related to: the repeatability of QO amplifier performance; effect of feed configuration; thermal properties of substrate; effect of device biasing; and sensitivity to fabrication tolerances. Three different feed configurations (far-field, near-field hard horn, and Gaussian beam) are studied. Of particular note, a near-field electro-optic (EO) probe station proved to be valuable in the diagnosis of design and fabrication flaws.

DEDICATION

I would like to thank my parents, Annie and Henry, my brother, Craig, and my Grandmother, Anna Petroff, who have never wavered in their support, in any and all, of my endeavors. Craig thanks for helping me with the milling and copper bias line shields.

ACKNOWLEDGMENTS

I would like to acknowledge and thank the individuals in the Active Antennas Group at the University of Colorado: advisor; Dr. Zoya Popović, and graduate students; Dr. Eric Bryerton, Slavko Djukic, Michael Forman, Joseph Hagerty, Dr. Stein Hollung, Jan Peeters Weem, Darko Popović, Joe Tustin, James Vian, and Manoja Weiss, who have provided illuminating conversations about electromagnetic theory and practice. Michael Forman earned and deserves special recognition; namely, he and I collaborated for many years in a team effort to advance the technology of quasi-optical power combining at Ka-band. As a result, we co-authored six publications and some of the results summarized in these publications are reiterated in this thesis (concentrated in Chapter 3). Thanks go to Dr. Richard Waters, Ivan Perez, and Dr. Bart Van Zeghbroeck for their help with photolithography required in the fabrication of the arrays. I also recognize the help of Dr. Amir Mortazawi, Sean Ortiz, Dr. Erich Schlecht, John Hubert, and Lee Mirth during my initial learning phase of this project when we had many conference calls discussing the design of QO amplifiers on diamond substrates with liquid coolant. Note that this work was partially supported by Lockheed Martin under the DARPA MAFET3 program.

Some measurement techniques required specialized custom equipment; in particular, the EO probe station located at the University of Michigan and the Gaussian beam system located at the California Institute of Technology were used to characterize the amplifier arrays. I thank Kyoung Yang, Dr. Gerhard David, Dr. John Whitaker, and Dr. Linda Katehi for access to and help with their EO probe station. Dr. Blythe Deckman and Dr. David Rutledge helped me to characterize my final amplifier array in their Gaussian lens system.

CONTENTS

TABLES

TABLE

FIGURES

FIGURE

CHAPTER 1

INTRODUCTION TO KA-BAND QUASI-OPTICAL POWER COMBINING

1.1 Motivation

The principle motivation for using Ka-band (26.5-40 GHz) frequencies for both military and commercial applications is due to the fact that the earth's atmosphere does not attenuate electromagnetic radiation (see Figure 1.1) significantly at Ka-band frequencies. Ka-band systems also have the advantage of small antenna size as compared to microwave

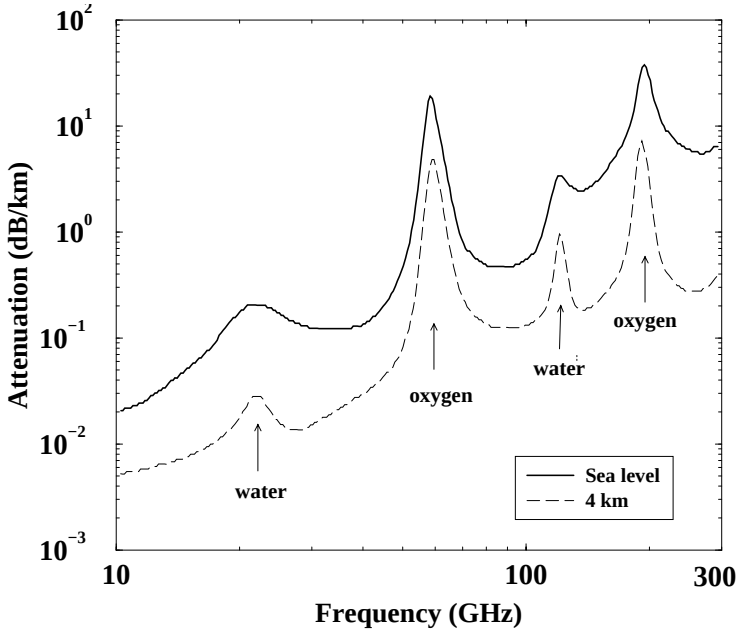

Figure 1.1. The attenuation of electromagnetic radiation is measured as a function of frequency [1]. At Ka-band (26.5-40 GHz), attenuation of electromagnetic radiation by the earth's atmosphere is relatively low.

systems. In most Ka-band transmitters, such as the ones used in missiles and satellites,

one to one-hundred watt power amplifiers are needed. In fact, the project presented in this dissertation began as a collaboration with Lockheed Martin to find a small light-weight watt-level Ka-band power source for missile guidance.

At microwave frequencies (below 30 GHz), individual solid-state devices have been demonstrated with output power levels on the order of 10 W (see Figure 1.2), but as frequency (f) increases, device loss increases which limits output power at Ka-band. The tube-based

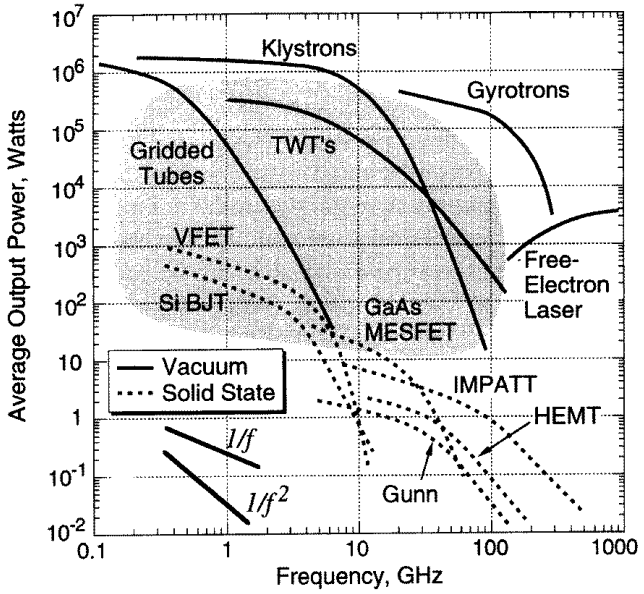

Figure 1.2. Average output power is plotted as a function of frequency for some millimeter-wave sources [1]. The high-power vacuum based devices are shown as solid lines. The lower-power solid state devices are shown as dashed lines.

devices (such as the Klystron and TWT) deliver high power, but are bulky, less tolerant to failures, and more expensive than solid-state devices. For example, two commercially available TWT amplifiers that achieve tens of watts at Ka-band, manufactured by *Litton* and *AR Research*, cost \$50,000 and \$110,000, respectively. At Ka-band, the output power of an individual solid-state device is proportional to $1/f^2$; consequently, to obtain Ka-band watt-level power, the power from multiple solid-state devices needs to be combined efficiently.

The corporate power combiner shown schematically in Figure 1.3(a) is typically used to combine the power of individual amplifiers using guided wave structures and Wilkinson

combiners. Each Wilkinson combines the power of two balanced input ports into a single output port, but not perfectly. Each element of the corporate combiner has insertion loss (L) which contributes to overall efficiency. Since there are $N = 2^k$ elements in k stages, the total output power from the corporate power combiner including loss is

$$P_{\text{output}} = P_{\text{i}} 2^k \text{L}^k \tag{1.1}$$

where P_{i} is the power output from each individual amplifier. Using the definition of power combining efficiency (PCE):

$$\text{PCE} = \eta = \frac{P_{\text{output}}}{\sum_{i=1}^{N} P_{\text{i}}} \tag{1.2}$$

the PCE of a corporate combiner with k stages is

$$\eta = \text{L}^k \tag{1.3}$$

Note that for guided wave structures L is proportional to $\sqrt{f}$ and increases as frequency increases. The theoretical PCE is plotted as a function of the number of stages in Figure 1.3(b). For a small insertion loss per element ($L = 0.5\,\text{dB}$), the PCE decreases rapidly to 70% with only three stages (eight amplifiers). Hence, a different power combining scheme is needed in which the PCE does not decrease as the number of amplifiers increases.

In 1968, an alternative method to the corporate combiner was introduced which combined the power of multiple solid-state devices in free space at 450 MHz [2]. In [2], an array consisting of 100 dipole antennas (see Figure 1.4), each connected to the output of a transistor capable of producing 1 W with 7 dB gain, radiated 100 W with a net gain of 4.75 dB; as a result, an alternative power combining scheme with high PCE was created. Since 1968, several researchers have demonstrated Ka-band quasi-optical amplifier arrays: in [3], the first successful watt-level millimeter-wave QO amplifier array was presented; in [4], monolithic microwave integrated circuit (MMIC) amplifiers were combined using patch antennas with 4 W of output power and 16 dB of large-signal gain; in [5] and [6], monolithic grid amplifiers, using HBTs and pHEMTs respectively, showed gain up to 60 GHz; and in

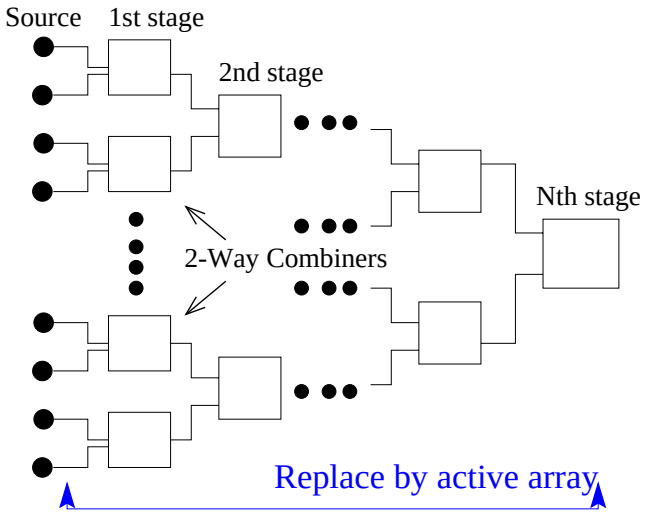

(a) Corporate power combiner

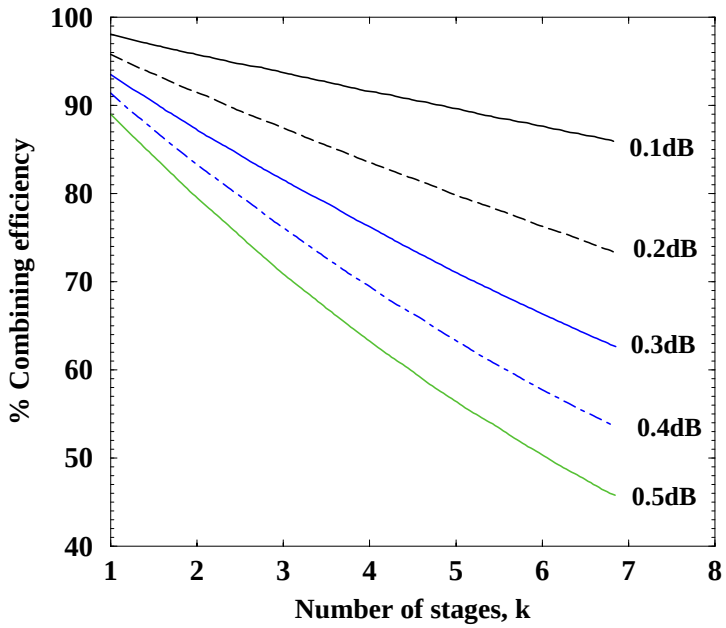

(b) Theoretical combining efficiency

Figure 1.3. The conventional corporate power combiner (a) utilizes guided wave structures. Each stage has insertion loss which contributes to the total power combining efficiency (b) of the corporate power combiner [1].

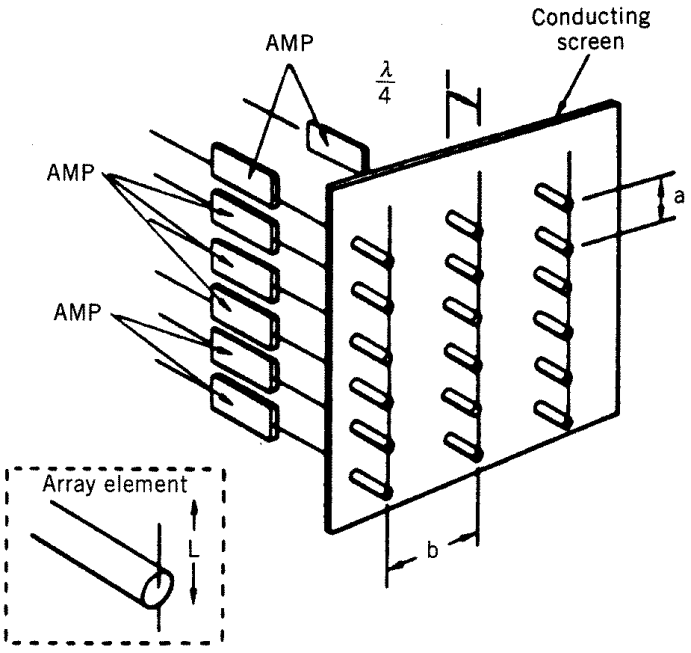

Figure 1.4: The first spatial power combiner [2].

[7], 1 W of power was obtained in an array mounted in a waveguide. In these recent research efforts, the common motivation for quasi-optical amplifier power combining is to obtain watt level power from solid-state amplifiers at millimeter-wave frequencies with high combining efficiency.

1.2 Amplifier array theory

In the previous section, it was stated that quasi-optical power combiners can achieve high power combining efficiencies, but the explanation as to why was not given. In this section, a theoretical explanation is presented to further understand and confirm the benefits of quasi-optical power combining.

1.2.1 Basic theory of transmit-receive antenna system Figure 1.5 shows the textbook equivalent circuit for the transmit-receive antenna system [8, 9]. The source generator which supplies power to the transmitting antenna is specified by its Thévenin equivalent circuit (V_g and Z_g). The source generator supplies the current (I_t) to the transmitting

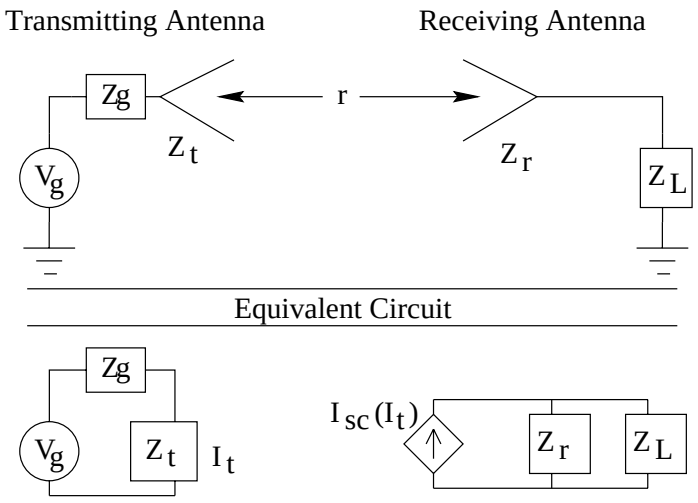

Figure 1.5: A picture of a simple transmit-receive antenna system.

antenna which radiates power. The total time average power radiated by the transmitting antenna is

$$P_t = \mathrm{Re}\left(\frac{Z_t |I_t|^2}{2}\right) \tag{1.4}$$

where Z_t is the radiation impedance of the transmitting antenna. A fraction of the radiated power is coupled to the receiving antenna. The receiving antenna then acts as the generator that delivers power to the load (Z_L). Finally, the amount of time-averaged real power delivered to the load Z_L connected to the receiving antenna is

$$P_L = \mathrm{Re}\left(\frac{Z_L |I_L|^2}{2}\right) \tag{1.5}$$

The problem of calculating the power in the load is reduced to determining the current (I_L) in the load.

The current in the load can be found by treating the receiving antenna as a generator for the load. The Norton equivalent circuit of the antenna in receive mode is defined by the short circuit current (I_{sc}) and its radiation impedance (Z_r). Therefore, the open circuit voltage of the receiving antenna is

$$V_{oc} = Z_r I_{sc} \tag{1.6}$$

and the current in the load is

$$I_L = \frac{V_{oc}}{Z_r + Z_L} \tag{1.7}$$

The open circuit voltage depends on the properties of both the transmitting and receiving antennas. If the two antennas are separated by a distance r, the open circuit voltage is given by

$$V_{oc} = j\eta k I_t \vec{l_t} \cdot \vec{l_r} \frac{e^{-jkr}}{4\pi r} \tag{1.8}$$

where the effective length for any antenna is given by

$$\vec{l}(\theta, \phi) = \frac{j2}{f\mu I_{in}} \vec{E}(\theta, \phi) \tag{1.9}$$

$\vec{E}(\theta, \phi)$ is the radiated electric field vector in the far-field. The far-field is determined by $r > 2D^2/\lambda$ where D is the characteristic size of the antenna. For any given antenna, $\vec{E}(\theta, \phi)$ in transmit mode is identical to $\vec{E}(\theta, \phi)$ in receive mode. The power P_L delivered to the load in a wireless line-of-sight link is determined by the current in the transmitting antenna (I_t), the frequency (f) of operation, the distance between antennas, and both the transmitting and receiving antenna far-field radiation patterns.

1.2.2 Generalization of the transmit-receive antenna system Since QO amplifier arrays have efficient power combining as their ultimate goal, it is important to account for the different power loss mechanisms. The aim of this section is to use Eqn.(1.8) and determine the induced currents at arbitrary elements in a quasi-optical array. Based on the currents, an accounting of power inside the quasi-optical system can be tabulated. In the case with multiple transmit-receive antenna pairs (as is the case in a quasi-optical amplifier), the dot product in Eqn.(1.8) differs based on the arbitrary positions and orientations of the antennas which make up the array. For completeness, the geometric problem of calculating the dot product in Eqn.(1.8) is presented and solved in general terms in this section.

Two arbitrarily located and arbitrarily oriented transmitting and receiving antennas are shown in Figure 1.6. The global coordinate system is in Cartesian coordinates and the

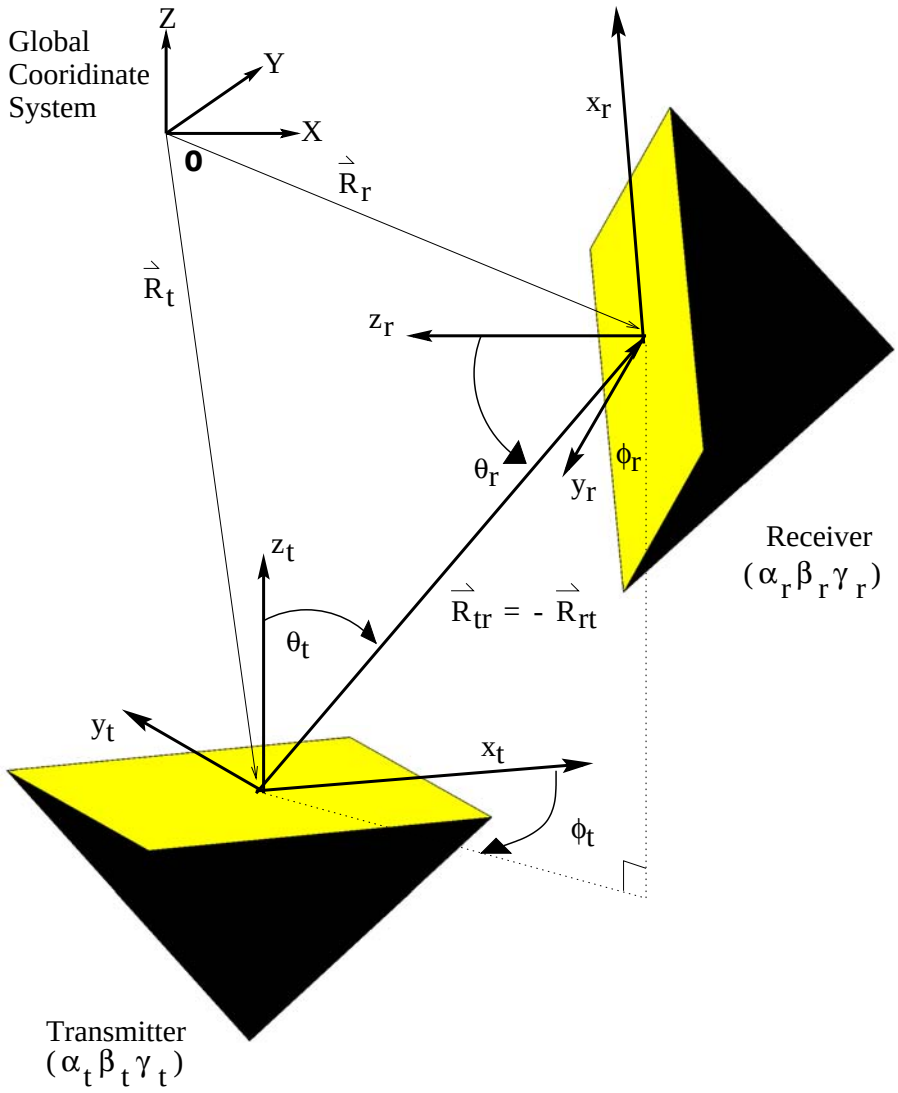

Figure 1.6. Definition of variables used in the generalized transmit-receive antenna system.

global origin is labeled $\mathbb{O}$. The location of the transmitting antenna is $\vec{R}_t$ and the location of the receiving antenna is $\vec{R}_r$. The orientation of the transmitting antenna is given by its Euler angles $(\alpha_t, \beta_t, \gamma_t)$ in radians (see Figure 1.7) [10]. Similarly, $(\alpha_r, \beta_r, \gamma_r)$ is given for the

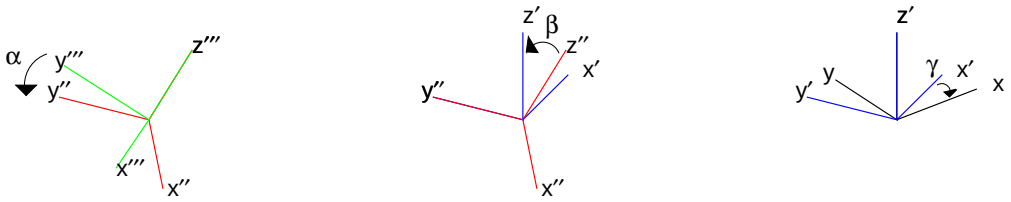

Figure 1.7. The definitions of the Euler angles. In this particular case, $(\alpha, \beta, \gamma) = (-\pi/6, -2\pi/5, -\pi/7)$.

receiving antenna orientation. Far-field antenna radiation patterns are naturally described by vectors in spherical coordinates which are functions of (θ, ϕ). The effective length vector is naturally written in spherical coordinates as:

$$\vec{l}(\theta,\phi) = l_r(\theta,\phi)\hat{\rho}(\theta,\phi) + l_\theta(\theta,\phi)\hat{\theta}(\theta,\phi) + l_\phi(\theta,\phi)\hat{\phi}(\theta,\phi) \tag{1.10}$$

Care must be taken to correctly apply the dot product whenever vectors are described by spherical coordinates since the orientation of the unit spherical vectors varies as a function of (θ, ϕ). One approach is to calculate the effective lengths of both transmitting and receiving antennas in global Cartesian coordinates and then calculate the dot product as

$$\vec{L_t} \cdot \vec{L_r} = [L_t]^T [L_r]^* \tag{1.11}$$

$$= \begin{bmatrix} L_{t,X} L_{t,Y} L_{t,Z} \end{bmatrix} \begin{bmatrix} L^*_{r,X} \\ L^*_{r,Y} \\ L^*_{r,Z} \end{bmatrix} \tag{1.12}$$

$$= L_{t,X}L^*_{r,X} + L_{t,Y}L^*_{r,Y} + L_{t,Z}L^*_{r,Z} \tag{1.13}$$

The subscript "t" refers to the transmitting antenna and "r" refers to the receiving antenna. The convention of capitalizing quantities which refer to vectors described in the global coordinate system $\mathbb{O}$ is adopted. Non-capitalized quantities refer to vectors in local coordinates.

What is the effective length in global Cartesian coordinates of the transmitting antenna located at (θ_r, ϕ_r) in the receiving antenna's local coordinate system? The vector between the transmitting antenna and the receiving antenna in global coordinates is given by

$$\vec{R}_{tr} = \vec{R}_r - \vec{R}_t \tag{1.14}$$

Since the local coordinate system of the transmitting antenna is defined by the Euler rotation angles, the position of the receiving antenna in the transmitting antenna's local coordinate system is found by an Euler coordinate rotation (U):

$$\vec{r}_{tr} = [U(\alpha_t, \beta_t, \gamma_t)]^{-1} \begin{bmatrix} X_{tr} \\ Y_{tr} \\ Z_{tr} \end{bmatrix} \tag{1.15}$$

where the Euler coordinate rotation matrix is

$$[U(\alpha, \beta, \gamma)] \equiv [U_z(\gamma)][U_y(\beta)][U_z(\alpha)] \tag{1.16}$$

and

$$U_z(\alpha) \equiv \begin{bmatrix} \cos(\alpha) & \sin(\alpha) & 0 \\ -\sin(\alpha) & \cos(\alpha) & 0 \\ 0 & 0 & 1 \end{bmatrix} \tag{1.17}$$

and

$$U_y(\beta) \equiv \begin{bmatrix} \cos(\beta) & 0 & -\sin(\beta) \\ 0 & 1 & 0 \\ \sin(\beta) & 0 & \cos(\beta) \end{bmatrix} \tag{1.18}$$

The location of the receiving antenna in the transmitting antenna's local spherical coordinate

system is given by $(r_{tr}, \theta_t, \phi_t)$ where [1]

$$r_{tr} = \sqrt{\vec{r}_{tr} \cdot \vec{r}_{tr}} \tag{1.19}$$

$$\cos\theta_t = \frac{z_{tr}}{r_{rt}} \tag{1.20}$$

$$\sin\theta_t = \frac{x_{tr}^2 + y_{tr}^2}{r_{rt}} \tag{1.21}$$

$$\cos\phi_t = \frac{x_{tr}}{x_{tr}^2 + y_{tr}^2} \tag{1.22}$$

$$\sin\phi_t = \frac{y_{tr}}{x_{tr}^2 + y_{tr}^2} \tag{1.23}$$

The effective length $(l_{t,r}, l_{t,\theta}, l_{t,\phi})$ of the transmitting antenna in its local spherical coordinate system is calculated from the local position $(r_{tr}, \theta_t, \phi_t)$. The effective length is then converted into local Cartesian coordinates by a matrix multiplication as follows

$$\begin{bmatrix} l_{t,x} \\ l_{t,y} \\ l_{t,z} \end{bmatrix} = [C(\theta_t, \phi_t)]^T \begin{bmatrix} l_{t,r}(\theta_t, \phi_t) \\ l_{t,\theta}(\theta_t, \phi_t) \\ l_{t,\phi}(\theta_t, \phi_t) \end{bmatrix} \tag{1.24}$$

where

$$[C(\theta, \phi)] \equiv \begin{bmatrix} \sin(\theta)\cos(\phi) & \sin(\theta)\sin(\phi) & \cos(\theta) \\ \cos(\theta)\cos(\phi) & \cos(\theta)\sin(\phi) & -\sin(\theta) \\ -\sin(\phi) & \cos(\phi) & 0 \end{bmatrix} \tag{1.25}$$

Finally, the effective length in the global Cartesian coordinates is found by an Euler coordinate rotation:

$$\begin{bmatrix} L_{t,X} \\ L_{t,Y} \\ L_{t,Z} \end{bmatrix} = [U(\alpha_t, \beta_t, \gamma_t)] \begin{bmatrix} l_{t,x} \\ l_{t,y} \\ l_{t,z} \end{bmatrix} \tag{1.26}$$

Hence,

$$\begin{bmatrix} L_{t,X} \\ L_{t,Y} \\ L_{t,Z} \end{bmatrix} = [U(\alpha_t, \beta_t, \gamma_t)][C(\theta_t, \phi_t)]^T \begin{bmatrix} l_{t,r}(\theta_t, \phi_t) \\ l_{t,\theta}(\theta_t, \phi_t) \\ l_{t,\phi}(\theta_t, \phi_t) \end{bmatrix} \tag{1.27}$$

[1] As a practical note, in most calculations of the radiation pattern θ_t and ϕ_t are rarely found outside of the cos and sin functions. Therefore, it is usually unnecessary to waste time by calculating the inverse trigonometric functions to determine numerical values for θ_t and ϕ_t.

The effective length in global Cartesian coordinates of the transmitting antenna at $\vec{R}_t$ seen by the receiving antenna at $\vec{R}_r$ is the product of the Euler rotation matrix evaluated at $(\alpha_t, \beta_t, \gamma_t)$, the $[C]^T$ matrix evaluated at (θ_t, ϕ_t), and the effective length $\vec{l}_t$ (in local spherical coordinates) evaluated at $(r_{tr}, \theta_t, \phi_t)$. Similarly, the effective length of the receiving antenna at $\vec{R}_r$ is

$$\begin{bmatrix} L_{r,X} \\ L_{r,Y} \\ L_{r,Z} \end{bmatrix} = [U(\alpha_r, \beta_r, \gamma_r)][C(\theta_r, \phi_r)]^T \begin{bmatrix} l_{r,r}(\theta_r, \phi_r) \\ l_{r,\theta}(\theta_r, \phi_r) \\ l_{r,\phi}(\theta_r, \phi_r) \end{bmatrix} \tag{1.28}$$

where $[U]$ is evaluated at $(\alpha_r, \beta_r, \gamma_r)$, $[C]^T$ is evaluated at (θ_r, ϕ_r), and $\vec{l}_r$ is evaluated at $(r_{rt}, \theta_r, \phi_r)$. Note that the index "$rt$" of r_{rt} reflects the fact that $\vec{R}_{rt} = -\vec{R}_{tr}$ is used to calculate $(r_{rt}, \theta_r, \phi_r)$ from Eqs.(1.19).

The generalized form of Eqn.(1.8) which is applicable to to both linear and circular polarized waves is

$$V_{oc} = j\eta k I_t \vec{L}_t \cdot \vec{L}_r \frac{e^{-jkR_{rt}}}{4\pi R_{rt}} \tag{1.29}$$

where the effective lengths in global Cartesian coordinates are derived from the given effective lengths in spherical coordinates. The pertinent dot product is written explicitly as

$$\begin{bmatrix} \\ [U(\alpha_t, \beta_t, \gamma_t)][C(\theta_t, \phi_t)]^T \end{bmatrix} \begin{bmatrix} lt_r(\theta_t, \phi_t) \\ lt_\theta(\theta_t, \phi_t) \\ lt_\phi(\theta_t, \phi_t) \end{bmatrix} \Bigg]^T \Bigg[\begin{bmatrix} \\ [U(\alpha_r, \beta_r, \gamma_r)][C(\theta_r, \phi_r)]^T \end{bmatrix} \begin{bmatrix} lr_r(\theta_r, \phi_r) \\ lr_\theta(\theta_r, \phi_r) \\ lr_\phi(\theta_r, \phi_r) \end{bmatrix} \Bigg]^* \tag{1.30}$$

1.2.3 Superposition - Power combining Figure 1.8 shows a typical QO amplifier array including far-field feed and collecting horn employed in this thesis. The equivalent circuit diagram for the quasi-optical amplifier system is given in Figure 1.9. The far-field feed horn Z_{ti} is connected to a Thévenin equivalent generator (V_g and Z_g). The amplifier receiving antennas $[Z_r]$ act as generators which drive their respective loads. The loads seen by the input antennas are represented by the $[ABCD]$ matrices terminated by

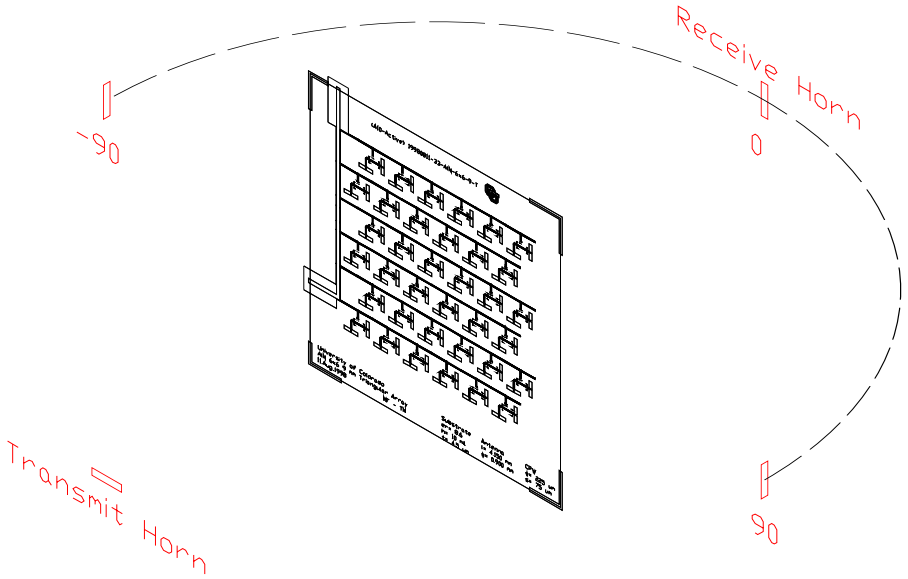

Figure 1.8. A schematic of a typical quasi-optical amplifier array system with far-field feed and collect horns.

$[Z_{to}]$ (the output antenna impedances). The use of $[ABCD]$ matrices allows any combination of transmission lines, internal reactive discontinuities, and MMIC amplifiers to be inserted between input and output antennas; as a result, their effects can be modeled. The time averaged power in each of the output antennas $[Z_{to}]$ is radiated power which is received by the collect horn Z_{ro}. Finally, the power delivered to the load from the generator V_g is $P_L = \mathrm{Re}(\frac{1}{2} Z_L |I_L|^2)$.

In mathematical terms, this problem can be explicitly solved. The location of the feed horn is $\vec{R}_{ti}$ and its orientation is $(\alpha_{ti}, \beta_{ti}, \gamma_{ti})$. The locations and orientations of each amplifier's receiving antennas are given by $\{\vec{R}_{ri}\}$ and $\{(\alpha_{ri}, \beta_{ri}, \gamma_{ri})\}$. By convention, the $\{\vec{R}_{rt}\}$ is the set of the positions describing all of the individual amplifier receiving antenna locations in global Cartesian coordinates. Individual elements in the set are described by adding a subscript to the $\{\}$; for example, the orientation of the n^{th} receiving antenna is given by $\{(\alpha_{ri}, \beta_{ri}, \gamma_{ri})\}_n \equiv (\alpha_{ri_n}, \beta_{ri_n}, \gamma_{ri_n})$. All mathematical operations on the sets $\{\}$ are assumed to be point-wise operations. For example, the dot product over two sets is defined

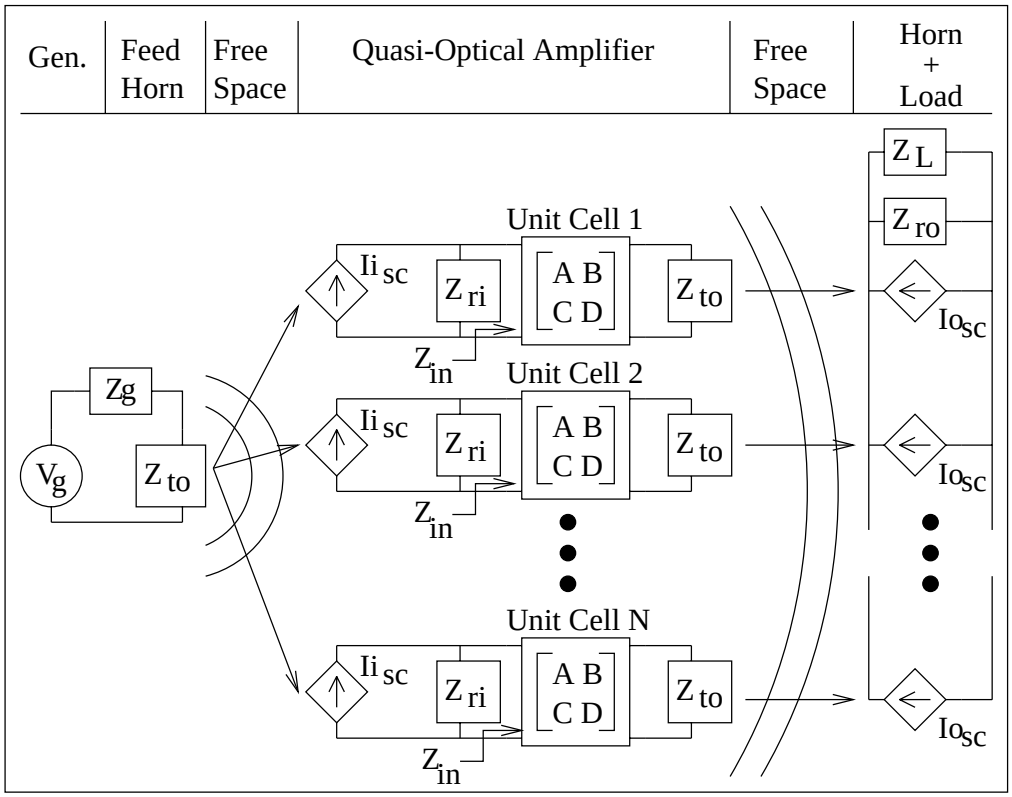

Figure 1.9. The equivalent circuit of the QO amplifier with far-field feed and collect horns shown in Figure 1.8. The propagation of electromagnetic radiation is shown schematically only; the circuit elements include field propagation when evaluated.

by convention to be $\{\{\vec{A}\}\cdot\{\vec{B}\}\} \equiv \{\vec{A}_1\cdot\vec{B}_1, \vec{A}_2\cdot\vec{B}_2 \ldots \vec{A}_N\cdot\vec{B}_N\}$. Using this convention and assuming the effective lengths for both the feed horn and the amplifier receiving antennas are known in local spherical coordinates, $\{\vec{L}_{ti}\}$ and $\{\vec{L}_{ri}\}$ are known in global Cartesian coordinates from Eqn.(1.30). Hence, the set of open circuit voltages at each of the amplifier receiving antennas is

$$\{V_{i,oc}\} = j\eta k I_{ti}\{\{\vec{L}_{ri}\}\cdot\{\vec{L}_{ti}\}\}\frac{e^{-jk\{R_{tr}\}}}{4\pi\{R_{tr}\}} \tag{1.31}$$

The set of currents $\{I_{in}\}$ is related to the open circuit voltages by

$$\{I_{in}\} = \frac{\{V_{i,oc}\}}{\{Z_{ri}\}+\{Z_{in}\}} \tag{1.32}$$

and from the $[ABCD]$ matrix, the set of impedances seen by the receiving antennas is

$$\{Z_{in}\} = \frac{\{A\}Z_{to} + \{B\}}{\{C\}Z_{to} + \{D\}} \tag{1.33}$$

Hence, the complex power received by each receiving antenna in the array is

$$\{S_{in}\} = \frac{1}{2}\{Z_{in}\}\{|I_{in}|^2\} \tag{1.34}$$

So the total time-average power received by the array is

$$P_{in} = \mathrm{Re}\left(\sum_n \{S_{in}\}_n\right) \tag{1.35}$$

The calculation is repeated on the output side of the amplifier array using the currents in the output amplifier antennas as the sources of re-radiated output power. The set of currents in the output amplifier antennas is

$$\{I_{to}\} = -\{C\}\{Z_{in}\}\{I_{in}\} + \{D\}\{I_{in}\} \tag{1.36}$$

The locations and orientations of each amplifier's transmitting antennas are given by $\{\vec{R}_{to}\}$ and $\{(\alpha_{to}, \beta_{to}, \gamma_{to})\}$. The location of the collect horn is $\vec{R}_{ro}$ and its orientation is $(\alpha_{ro}, \beta_{ro}, \gamma_{ro})$. Note that when calculating the effective length it is important to use the real part of the antenna terminal impedance, $\mathrm{Re}(Z_{to})$. The total open circuit voltage of the collect feed horn is

$$V_{o,oc} = \sum_n \left\{ j\eta k\{I_{to}\}\{\{\vec{L}_{to}\} \cdot \{\vec{L}_{ro}\}\}\frac{e^{-ik\{R_{rt}\}}}{4\pi\{R_{rt}\}} \right\}_n \tag{1.37}$$

The total current in the load Z_L is

$$I_L = \frac{V_{o,oc}}{Z_{ro} + Z_L} \tag{1.38}$$

Finally, the total time average power delivered to the load is

$$P_L = \mathrm{Re}\left(\frac{1}{2}Z_L|I_L|^2\right) \tag{1.39}$$

A typical quasi-optical amplifier system (see Figure 1.8) based on its equivalent circuit model (see Figure 1.9) has been characterized. Insight into the characteristics of a quasi-optical amplifier can be better understood from application of the equivalent circuit model. Two examples which help solidify understanding are presented in the following subsections.

1.2.4 Calculation of gain for a typical QO amplifier Assume a feed horn with a gain of 24.7 dB operating at a frequency of 30.8 GHz is located 1 m from an amplifier array – these represent typical values at Ka-band. An identical collect horn is located symmetrically on the other side of the array from the feed horn but orthogonally polarized (recall Figure 1.8). The amplifier array is placed at the origin of the global Cartesian coordinate system. The amplifier array utilizes a 6-by-5 triangular array lattice with a unit cell spacing of 7.5 mm (0.77λ). In each unit cell there is a receiving antenna connected by an $[ABCD]$ matrix to an orthogonally polarized transmitting antenna. As an approximation, the receiving and transmitting antennas are both modeled as linear-tapered horns with a representative gain of 8.7 dB. The generator supplies 1 W to the feed horn.

Three cases (similar to a real array characterization experiment) are calculated and compared for the quasi-optical array system: with feed and collect horns co-polarized and no array present; with a passive array; and with an ideal active amplifier array. The first calculation without the array, but with co-polarized feed and collect horns, serves as a "through" calibration. The second calculation determines P_L when the passive array is present; similarly, the third calculation determines P_L for the active array. The only difference between the passive and active amplifier arrays is whether or not MMIC amplifiers are present. The passive array uses the $[ABCD]$ matrix for a passive transmission line, but the active array uses the $[ABCD]$ matrix for a 19 dB gain MMIC.

Table 1.1 summarizes the results of the three calculations. The co-polarized horn calculation is used as a calibration to define $S_{21} = P_L - 11.2\,\text{dB}$. Due to the far-field feed

and the calibration, the passive array has a loss of $S_{21} = -8.4\,\text{dB}$. As a consequence, the

Table 1.1. Comparison of theoretical output powers from an array of 30 elements (N=6 and M=5) with and without MMIC amplifiers. The Co-pol calculation is used as a calibration.

Case	$[ABCD]$	P_t[dBm]	P_{in}[dBm]	P_{out}[dBm]	P_L[dBm]	S_{21}[dB]
Co-pol	NA	30	NA	NA	11.2	0
Passive	CPW through	30	16.5	16.5	2.8	-8.4
Active	MMIC	30	16.5	35.5	21.8	10.6

active array achieves $19 - 8.4 = 10.6\,\text{dB}$ gain. Overall, the actual power transferred to the load P_L is 21.8 dB which is 8.2 dB less than the power supplied by the feed generator. This problem is due to the far-field feed but can be solved using a different feed configuration (see Section 1.3). An intuitive solution might be to move the feed and collect horns closer to the array, but based on calculations using this theory, polarization mismatch loss and non-uniform array excitation make such a solution inefficient.

1.2.5 Calculation of currents on a typical QO amplifier The results in the previous section could have been found with a much simpler calculation using the Array factor. The value of going through the detailed calculation to find the currents on the array is that it lends insight into possible types of unit cell variations. Variations in input current among unit cells would not be a problem for an ideal linear MMIC amplifier. However, a real MMIC amplifier is non-linear when it is driven into saturation. Usually, one tries to get the maximum output power from an array by increasing the input RF power until the output RF power is saturated. It is difficult to determine the $[ABCD]$ matrix for an individual MMIC in saturation. However, some insight can still be gained by looking at the individual currents (or equivalently, individual input MMIC RF powers) at the input of the array (output from each individual receiving array antenna).

The currents are calculated for the same configuration used in the previous subsection. Figure 1.10 shows a plot of the magnitude of current as a function of the n^{th} element. The first element is located in the upper left corner of the array. Successive elements are

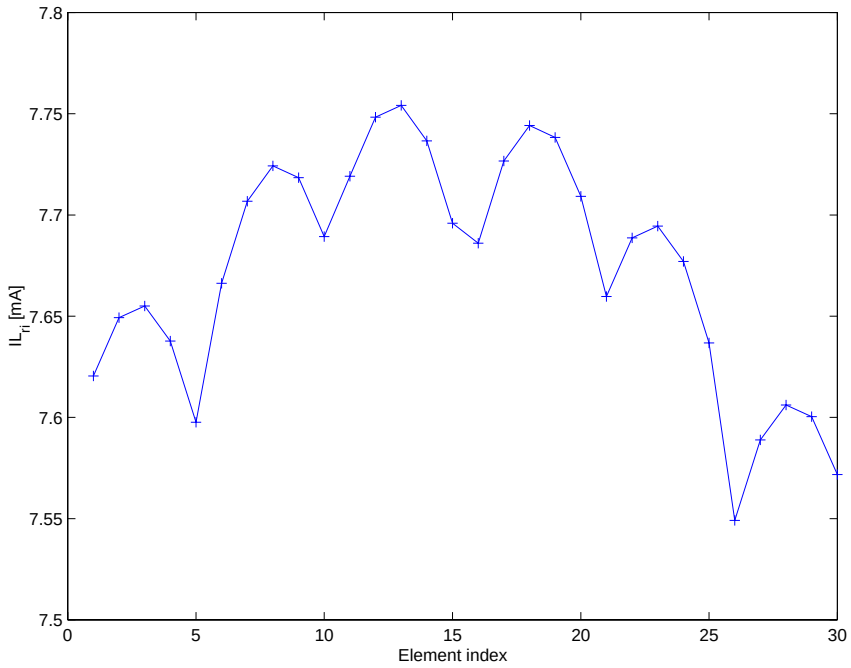

(a) Amplitude

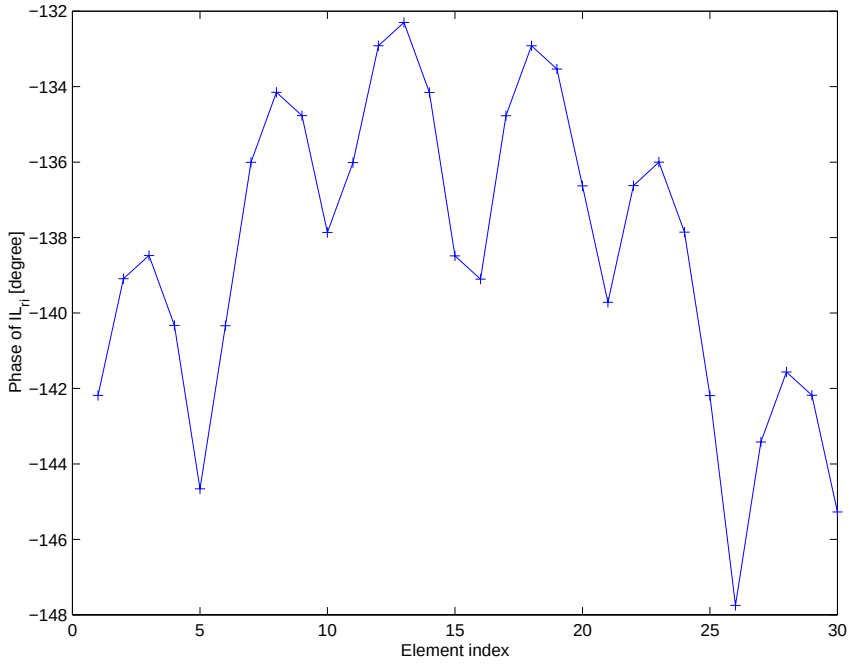

(b) Phase

Figure 1.10. Theoretical variation in amplifier input current is plotted as a function of array element number. The 1 W feed horn is located 1 m away from the array.

incrementally labeled as reading a page of text. It is clear that not all MMICs receive the same RF input power. The center elements receive more power than the outer elements; however, the variation is less than 3% due to the location of the transmit feed location in the far-field of the entire array. In principle, unit cells nearest the center of the array will reach saturation before elements on the periphery of the array. As the power from the feed horn is increased, an increasing number of elements will be saturated, until all elements are saturated. The effect will be an unpredictable variation in the phase of the unit cells.

1.2.6 Further simplification due to far-field feed The power into an amplifier array [Eqn.(1.35)] and the power delivered to the load attached to the collect horn [Eqn.(1.39)] are general equations which account for variations among unit cells within an amplifier array. Variations within the array occur in practice and can significantly alter the amplifier array performance. However, insight into the operation of ideal amplifier arrays can be learned from simplification of Eqs.(1.35) and (1.39).

Ideally, under normal far-field conditions all unit cells behave identically: the gain of the individual amplifiers are equal, the $[ABCD]$ matrices do not vary across the array, and the frequency response of each antenna is not affected by its nearest neighbors. The vector distance from any source antenna $\vec{r'}$ and the observation point $\vec{r}$ is

$$\vec{R} = \vec{r} - \vec{r'} \tag{1.40}$$

By computing $\vec{R} \cdot \vec{R}$ and using the binomial expansion, the distance R is approximated by

$$R \approx r - \hat{r} \cdot \vec{r'} \tag{1.41}$$

Eqs.(1.35) and (1.39) have a radial dependence which is approximated by

$$\frac{e^{-ikR}}{4\pi R} \approx \frac{e^{-ikr}}{4\pi r} e^{ik\hat{r}\cdot\vec{r'}} \tag{1.42}$$

and the angular dependence is found from the Taylor series expansion

$$f(\theta', \phi') \approx f(\theta, \phi) + (\theta' - \theta)\frac{\delta f}{\delta \theta} + (\phi' - \phi)\frac{\delta f}{\delta \phi} \tag{1.43}$$

Since the size of the array is small

$$f(\theta', \phi') \approx f(\theta, \phi) \tag{1.44}$$

Combining Eqs.(1.42) and (1.44) with Eqn.(1.35), the input power to the array is

$$P_{in,\text{total}}(\theta, \phi) \approx N P_{in,\text{single}}(\theta, \phi) \tag{1.45}$$

$P_{in,\text{total}}$ is maximized when $(\theta, \phi) = (0, 0)$ since the array antennas are aligned such that their peak directivity is at $(\theta, \phi) = (0, 0)$. From Eqn.(1.45) and the superposition principle, the maximum total power radiated by the output antennas is

$$P_{rad,\text{total}} = N P_{in,\text{single}}(0,0) IL (1 - |S_{11}|^2) \eta_{\text{rad}} \tag{1.46}$$

The IL includes the MMIC gain and the mismatch loss between the input antenna and MMIC. The losses on the output side of the MMIC are due to output antenna mismatch $(1 - |S_{11}|^2)$ and the output antenna radiation efficiency (η_{rad}).

The power combining efficiency of the array is calculated from Eqs.(1.2) and (1.46) to be

$$\eta = \frac{N P_{in,\text{single}} IL (1 - |S_{11}|^2) \eta_{\text{rad}}}{N P_{in,\text{single}} IL} \tag{1.47}$$

$$= (1 - |S_{11}|^2) \eta_{\text{rad}} \tag{1.48}$$

The power combining efficiency does not depend on the number of elements in the array, provided all output elements are in phase with equal amplitude. In practice, the mismatch loss between the MMIC and the output antenna can be reduced to zero. The radiation efficiency of the output antenna sets the limit on the PCE of the array.

Assuming that the feed horn is placed at $(\theta, \phi) = (0, 0)$ to maximize $P_{in,\text{total}}$, the total power absorbed by the load [Eqn.(1.39)] is approximated with Eqs.(1.42) and (1.44).

$$P_{L,\text{total}}(\theta, \phi) \approx |AF|^2 \, P_{L,\text{single}}(\theta, \phi) \tag{1.49}$$

where AF is the standard Array Factor found in textbooks

$$AF(\hat{r}) = \sum_{n} e^{ik\hat{r}\cdot\vec{r'}} \tag{1.50}$$

Note that the Array factor should not be normalized to its peak value when calculating the total power [Eqn.(1.49)]. The array factor only depends on the positions of the array elements $\vec{r'}$ and the location of the receiving antenna $\hat{r}$. The array factor varies from zero to the total number of unit cells NM in the array. Therefore, the power transferred to the load is bounded by

$$0 < P_{L,\mathrm{total}}(\theta,\phi) < (NM)^2 P_{L,\mathrm{single}}(\theta,\phi) \tag{1.51}$$

Note that $P_{L,\mathrm{single}}(\theta,\phi)$ describes loss mechanisms such as: dielectric loss tangent, antenna mismatch, polarization mismatch, substrate modes, and free-space feed loss. The losses, except for the free-space loss, can be reduced by careful array design. The free-space loss is due to the locations of the transmitting and receiving antennas in relation to the array and cannot be improved by simple means. Even though the PCE of the spatial power combiner is independent of the number of array elements, the free-space feed loss is dominant and necessitates the need for alternative feed configurations.

1.3 Alternative feed-collect configurations

Figure 1.11 schematically represents the problem associated with the previously described far-field feed configuration. Because the transmit and collect horns are placed in the far-field of the array ($2D^2/\lambda$) to achieve uniform plane-wave excitation, free-space and spill-over losses exist which overwhelm the benefit of quasi-optical power combining (power combining efficiency). Consequently, different feed-collect configurations are required.

Currently, there are four main QO amplifier feed-collect configurations designed to reduce the problematic loss associated with the far-field feed. Figure 1.12 summarizes the essential differences between the four configurations. Since free-space loss is dependent on the

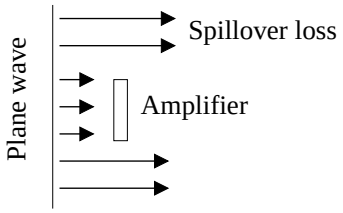

Figure 1.11: A schematic representation of spillover loss.

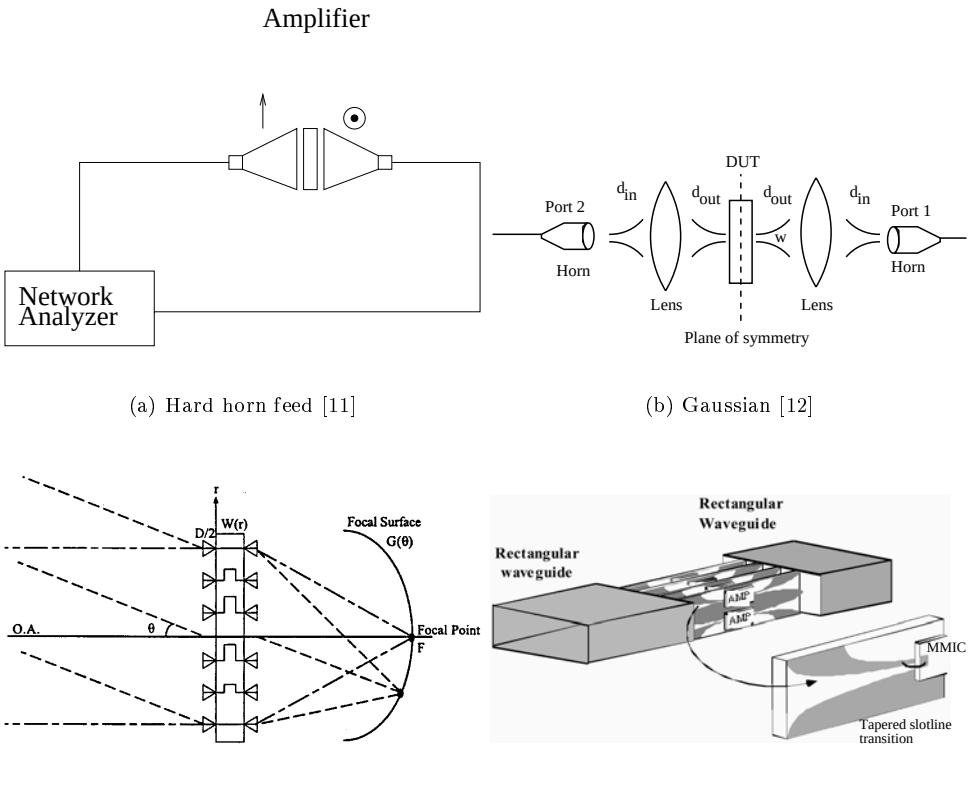

(a) Hard horn feed [11]

(b) Gaussian [12]

(c) Lens array [13]

(d) Waveguide [14]

Figure 1.12: Alternatives to the far-field feed.

distance from the feed horn to the array, the hard-horn configuration (a) places two custom designed horns as close to the array as possible ($\approx 0.5\lambda$). Each hard horn is designed to have uniform electric field amplitude and phase [15, 11] across its aperture to uniformly excite the QO array. A second method of array excitation (b) uses large (300 mm diameter at Ka-band) dielectric lenses to produce a Gaussian beam waist with a diameter on the order the size of the array [12]. By placing the array at the beam waist, the Gaussian lens system achieves the desired uniform phase across the array, but the amplitude is a non-uniform Gaussian profile. The hard-horn, Gaussian lens, and far-field feed configurations can be used to feed the identical QO active array, unaltered. The last two feed configurations require completely different QO amplifier array designs which are not compatible with the far-field, hard-horn, nor Gaussian lens feeds. Figure 1.12(c) shows a lens array which is designed to have a focal surface located 5-10λ from the array [13]. The feed loss for a lens array is theoretically as low as 2 dB.

1.4 Thesis organization

The goal of this thesis is to design, fabricate, and characterize an inexpensive Ka-band amplifier array with Watt level performance. The descriptive term "inexpensive" refers to both material costs and manufacturing costs. Up to this point, a simplified background of free-space power combining has been presented to motivate the benefits of QO amplifiers in contrast to corporate power combining techniques. Inevitably, second-order factors arise which are not accounted for in the simplified models which degrade the actual performance of QO arrays. These factors hamper the possibility of finding a simple, comprehensive, and accurate analytical description of the QO system.

The necessity of having an accurate analytical QO design leads to dependence on Computer Aided Design (CAD) tools (software packages). Commercially available CAD software packages based on Method of Moment (MOM) or Finite-Difference Time-Domain

(FDTD) approximations to Maxwell's equations which have sufficient accuracy are readily available. Even though these tools are accurate and available, they do not necessarily simplify the process of design. In general, CAD tools find a particular solution $F(p_1, p_2, \cdots p_N)$ given a fixed set of N design parameters $(p_1, p_2, \cdots p_N)$. For instance, a particular desired solution F of interest which would affect total array output power might be radiation efficiency of the array $F = \eta$. Radiation efficiency depends on dielectric losses of the substrate, the thickness of the substrate, ohmic losses due to metalization, the fundamental antenna type, and even the spacing between unit cells in the array. In this particular case there are five parameters which affect the radiation efficiency. Without an analytical solution, it is not necessarily obvious which of the five parameters is dominant and most important to the design. The most common method of dealing with this dilemma is to calculate F multiple times while the parameters $(p_1, p_2, \cdots p_N)$ are varied. The designer then tries to understand the meaning of the results. Most likely, the designer repeats the process of calculating F over a different set of parameter variations until the design meets specifications. This iterative process is referred to as the Design Loop.

The organization of this thesis is summarized by the flow chart shown in Figure 1.13 adopted from [16]. Chapter 2 summarizes the QO array amplifier design and theoretical array performance (Design Loop). The design parameters involve: MMIC choice, substrate choice, antenna modeling, array factor considerations, mutual coupling analysis, thermal analysis, and DC bias effects. As will be demonstrated in Chapter 2, the Design Loop can yield multiple satisfactory designs. A few of the more promising designs are selected for fabrication and their power performance is characterized based on a series of experiments. The characterization of the arrays is separated into two chapters. Array performance is characterized in Chapter 3 using far-field feed horns (as in Section 1.2.3, page 12) and hard-horns (as in Section 1.3). Chapter 4 summarizes near-field measurements performed in collaboration with the University of Michigan. The near-field measurements proved to be valuable in

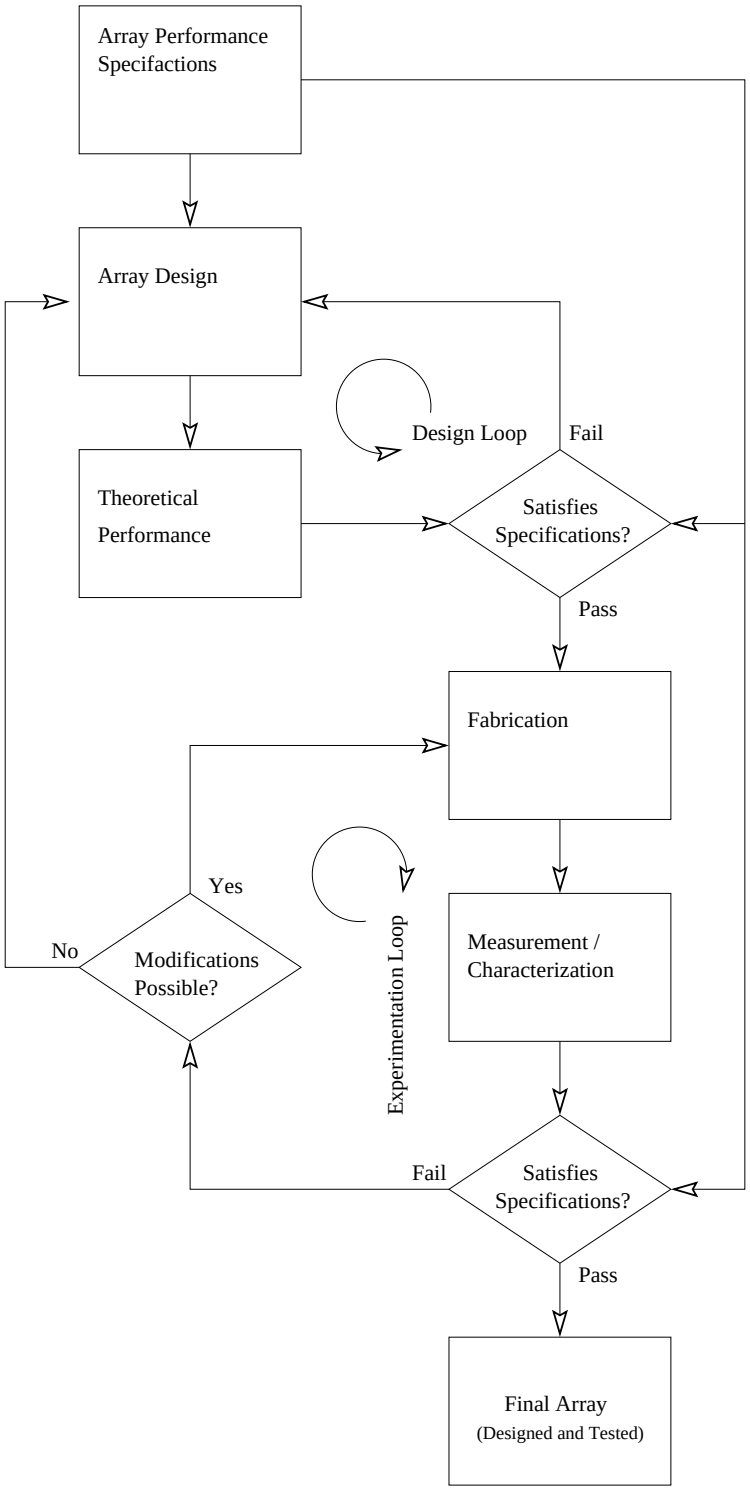

Figure 1.13: Flow chart shows thesis outline.

observing effects of mutual coupling and diagnosing design flaws. The demonstrated array performance (Chapter 3) and the insight gained from near-field measurements (Chapter 4) provided guidelines for a redesign of the QO amplifier array. Chapter 5 presents another complete Design Loop and Experimentation Loop with the goal of designing and characterizing an improved amplifier array. Concluding remarks and possibilities for future research are presented in Chapter 6.

CHAPTER 2

DESIGN AND ANALYSIS OF QO AMPLIFIER ARRAYS

In the previous introduction chapter, Figure 1.13 showed a conspicuously simple block labeled "Array Design" as part of the "Design Loop". The representation of "Array Design" as a single block removed from the "Theoretical Performance" block significantly under-represents the difficulties involved in a successful QO amplifier design. Figure 2.1 shows the inner details of the "Design Loop". Figure 2.1 makes the inter-dependence between

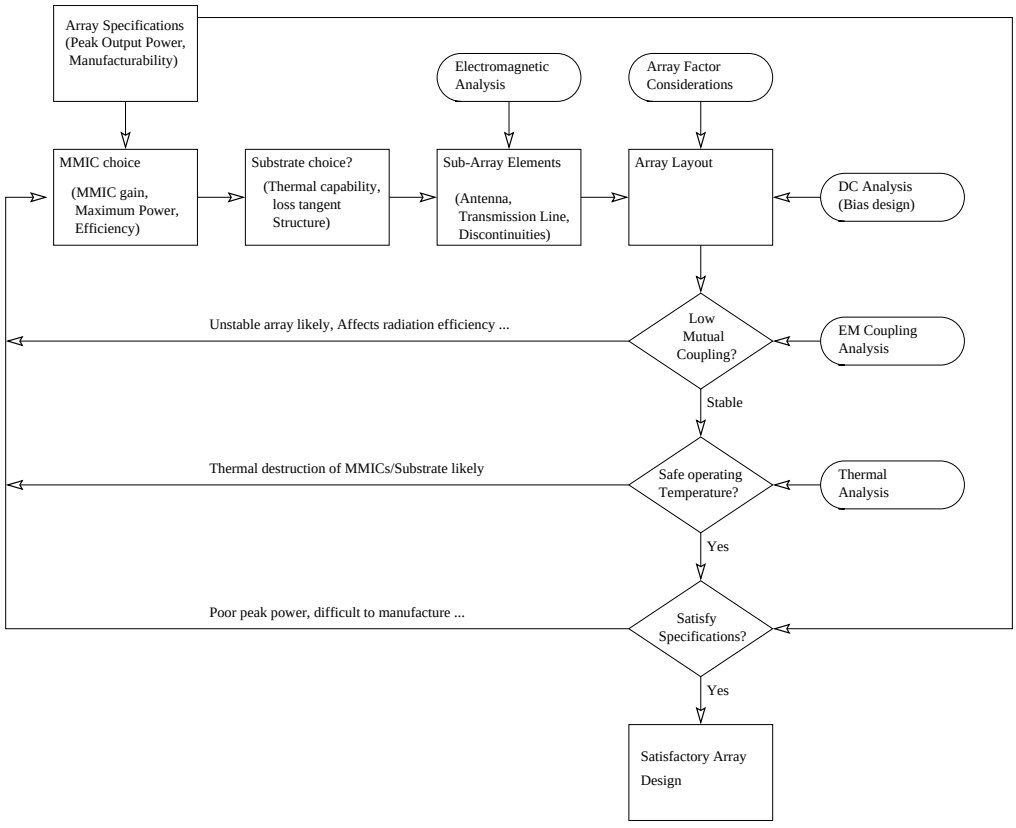

Figure 2.1: Design flow chart.

the "Array Design" and "Theoretical Performance" clear by not showing them as separate blocks. The "Array Design" is a result of the "Theoretical Performance". In other words, as expected from common sense, the real performance of the array can only be expected to be as good as the theoretical performance of the array design. Hence, as much detail as is possible must be included in the "Design Loop". The "Design Loop" includes: MMIC and substrate choices, transmission line type and discontinuities, antenna design, array layout considerations, DC bias effects, electromagnetic coupling effects in an active array, and thermal issues.

The goal of this Chapter is to understand the details involved in the design of a QO amplifier array and to produce a satisfactory design suitable for fabrication and characterization. Any satisfactory design must meet four specifications: the array must be capable of producing watt-level RF output power at Ka-band; the array must be inexpensive to build; the array must be relatively easy to manufacture; and the array must be stable both thermally and electrically. The low cost, ease of manufacture, and thermal stability requirements are the main issues that separate this research from other research efforts in the QO field. These requirements are achieved by using off-the-shelf medium power (tens of mW) MMICs, and single-sided processing of an aluminum nitride (AlN) substrate.

2.1 Overview of QO amplifier array design

Figure 2.2 shows the schematic representation of the type of QO configuration utilized in this thesis.[1] From all the different types of QO amplifier configurations possible (as described in Chapter 1) the configuration shown in Figure 2.2 is chosen based mainly on the ease of manufacturing and flexibility. The flexibility allows either far- or near-field feed configurations to be used with minimal alterations to the experimental setup. The difference

[1] This is not meant to be confused with a general QO power amplifier configuration. Other research efforts utilize different configurations as outlined in Chapter 1. For instance, some may or may not use polarizers which depends on whether or not their antennas are unidirectional or bidirectional.

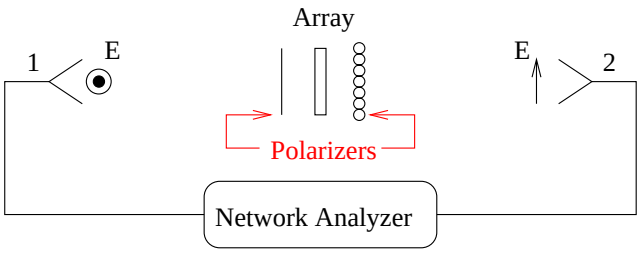

Figure 2.2. Schematic diagram of the QO configuration used in this thesis. The feed and collect antennas (ports 1 and 2) are placed in either the far-field or near-field of the active array depending on the specific type of feed horn.

between the far- and near-field configuration is the type of horn and its location relative to the array.

The final QO array design is the result of multiple design loop iterations. Rather than trying to explain each of the design loop iterations, the method chosen to present the overview of QO amplifier array design is to show the final QO design first, and subsequently explain the reasons as to why. The quasi-optical amplifier array shown in Figure 2.3 is the final array design. This final array is a design evolution of the first successful watt-level millimeter-wave QO amplifier array [3]. Port 1 (Figure 2.2) of the Network Analyzer is connected to a standard commercial Ka-band liner-tapered horn which produces a vertically-polarized plane wave at the array surface. The input slot antennas in the array receive power from the incident vertically-polarized plane wave. In each unit cell, the received power is coupled to a 50-Ω Coplanar Waveguide (CPW) transmission line, and is then amplified by a commercial MMIC amplifier. The amplified power is re-radiated in the horizontal polarization by the output slot antennas and is the coherent combination of all element outputs. Isolation and stability is partially provided by orthogonal polarization of input and output antennas. The amplified power is transferred to the load by the receiving horn (horizontally polarized) at Port 2 of the vector network analyzer.

The MMIC is the basis of the Ka-band amplifier array design. If the MMIC is highly efficient then low operating temperatures can be expected. Low operating temperatures allow

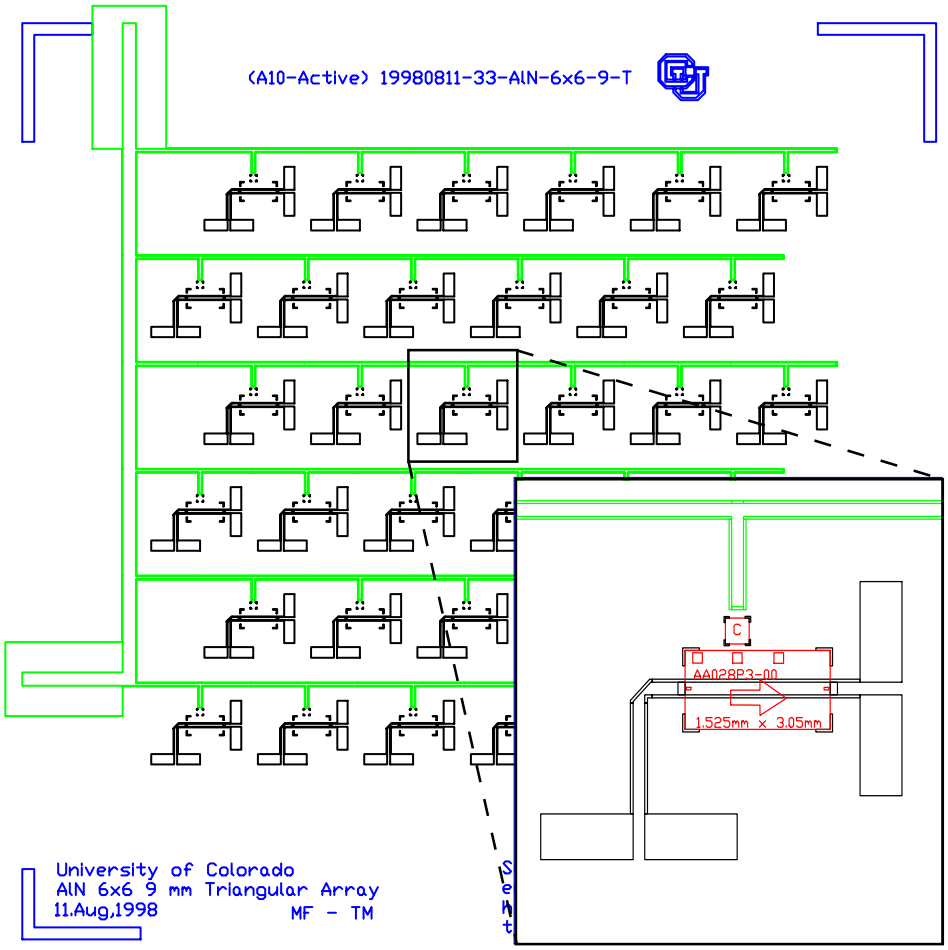

Figure 2.3. Schematic of a unit cell within the amplifier array. The slot antennas are orthogonally polarized and are connected to the MMIC by CPW transmission lines. The DC-bias line for the single-supply MMIC and blocking capacitor are also visible.

for standard substrates which can handle small temperature gradients. However, at Ka-band the efficiency of transistors is limited so exotic substrates which can handle the high heat production of multiple MMICs are required. Simultaneously, the designs of antennas and transmission lines are highly dependent on the RF properties of the substrate. Assuming that a substrate exists that is both thermally stable and has satisfactory RF characteristics, the sub-array elements are designed using accurate full-wave electromagnetic models. Once the sub-array elements are determined, the array layout can be determined. The design of the active array layout is not trivial. Specifically, the arrangement and placement of unit cells affects both the peak operating temperature and the RF stability of the array. The array layout depends on the array factor (alluded to in Chapter 1), on DC bias line design (high DC current density is likely) and, most importantly, on mutual coupling within the array. The array factor determines the radiation pattern of the array. The high DC current density and parallel bias configuration limits the total number of MMICs possible in an amplifier array. The RF interactions between DC bias lines and antennas, and between input and output antennas affect the RF array stability. These mutual coupling interactions are the most difficult parts of the design to account for and have a large effect on RF stability and peak power performance. The combination of all these inter-related design issues yields the final design given in Figure 2.3. The detailed explanations of the added design complexity as compared to the simplistic model from Chapter 1 are presented in the remaining sections.

2.2 Commercial MMIC amplifiers

The choice of MMIC amplifier is the starting point for the Ka-band amplifier array design. Table 2.1 summarizes common Ka-band MMICs which are currently available from various commercial vendors. Commercial Ka-band MMIC amplifiers typically have 10 to 20 dB of small-signal gain, and 16 to 31 dBm of output power at the 1-dB compression point. Their power added efficiency (PAE= $\frac{P_{\mathrm{RF,out}} - P_{\mathrm{RF,in}}}{P_{\mathrm{DC}}}$) is typically 10% to 20%. Cost per MMIC

Table 2.1: Comparison of commercially available Ka-band MMICs

Company	Model	Cost [$]	T_{op} [°C]	PAE [%]	Peak gain [dB]	S_{11} [dB]	$P_{1\,dB}$ [dBm]	Size [mm^2]	Bias
Alpha	AA032P1	32	90	15	14	-17	24	5.5	Dual
Alpha	AA028P4	35	90	NA	17	-18	26	6.2	Single
Alpha	AA028P1	33	90	10	15	-17	23	5.8	Single
Alpha	AA028P3	75	90	NA	19	-19	16	4.7	Single
UMS	CHA5091a	114	85	10	11	-56	26	10.2	Dual
Alpha	AA035p2	173	90	15	13	-20	26	11.3	Dual
Marconi	P355121	NA	NA	NA	17	-12	21	3.3	Dual
Filtronic	LMA443	NA	150	NA	20	-12	22	1.7	Dual
Raytheon	RMPA29000	NA	65	25	20	-8	29	15.3	Dual
Raytheon	RMPA29100	NA	65	15	20	-8	31	15.3	Dual
Raytheon	PKAFD01A3	NA	75	NA	15	-14	30	16.1	Dual

varies from $30 to $200.

Since there is a large variation among MMIC performance and cost, there is a wide set of options for choosing the MMIC. Ideally, the MMIC of choice is inexpensive, has a low reflection coefficient (S_{11}), high gain, high PAE, and high saturated output power. The cost of MMICs (without considering labor and assembly costs) represents the largest fraction of the total expense of Ka-band arrays. Typically, the total MMIC cost is 90% of all array material expenses. The simplest way to reduce cost is therefore to choose the least expensive MMIC. High return loss causes much of the power received by the input antennas to be wasted as scattered power, and simultaneously more input power is required to saturate the array (i.e., an external Ka-band amplifier might be required to saturate the array). The choice of MMIC gain is constrained by mutual coupling and array stability. The problem of mutual coupling, array stability, and MMIC gain are intimately linked and require a detailed discussion (see Section 2.7). A high PAE translates into lower array operating temperatures since less waste heat is generated by the MMICs with high PAE. As for the saturated MMIC output power levels, it is debatable [17] as to which is better: many low power MMICs or a few high power MMICs. Intuitively, a large saturated output power per MMIC should allow for cost reduction since fewer MMICs would be required to achieve a specified output power.

In practice, as shown in [17], the lower power devices have higher efficiencies and are less expensive. Since the power combining efficiency of QO arrays is independent of the number of devices, it is more advantageous to use high-efficiency lower-power devices.

A design compromise is made and the final MMIC is chosen to be the *Alpha* AA028P3-00 MMIC. The decision is to use a relatively low power MMIC with high gain. If the coupling problems associated with high gain (19 dB) can be overcome then it is a simple matter to improve power performance by later replacing the *Alpha* AA028P3-00 MMIC with a lower-gain higher-power MMIC. The converse is not true and would require a complete redesign to improve power performance.

2.3 Thermal analysis

The substrate is chosen based on three factors; structural rigidity, RF characteristics, and thermal properties. Structural rigidity is required to inhibit deformations of the substrate, which are harmful during both the fabrication and characterization stages. The RF characteristics of interest are the dielectric loss tangent and the relative permittivity of the substrates. The relative permittivity is a minor concern which mainly affects the size of antennas. The size of antennas varies slightly over the range of possible relative permittivity and does not affect the performance of the QO amplifier significantly. The dielectric loss tangent is a more critical design parameter, since a large loss tangent means power is wasted in the substrate. In addition to dielectric losses, heating of the array due to MMICs with typically low efficiencies can cause catastrophic array failures [18]. In fact, preventing thermal destruction of the arrays is a paramount concern. The substrate that is chosen must be a good thermal conductor and have a low dielectric loss tangent at Ka-band.

2.3.1 Thermal conduction model

The Ka-band MMIC amplifiers (see Table 2.1) typically have 10% to 25% efficiency. These efficiencies are quoted from the manufacturer's data sheets and represent peak performance. In Ka-band applications where

maximum output RF power is desired, 90% of the DC power is wasted due to unwanted heat generation. Typically, the MMICs (heat sources) are placed in close proximity to one another and this can lead to high operating temperatures. High temperatures can destroy the substrate or even destroy the MMICs themselves. Note that MMICs are based on GaAs substrates which have low (poor) thermal conductivity. In addition to possible thermal destruction, MMIC gain is affected adversely by operation temperature; in [19], Batty showed that a change in temperature from 60°C to 70°C can cause as much as a 4 dB decrease in MMIC gain. Therefore, good thermal management is an integral part of QO amplifier design and needs to be understood.

Figure 2.4 graphically represents the general thermal problem for planar QO amplifier arrays which can be modeled. The substrate is modeled as a rectangular block with

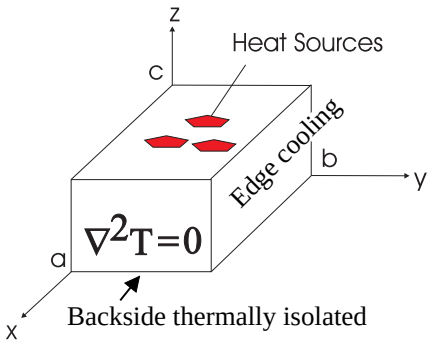

Figure 2.4: Schematic of thermal problem in Cartesian coordinates.

the following dimensions: the width is a; the length is b; and the thickness is c. On the top surface of the array there are MMICs which are represented by the red patches. From the thermal point of view, the MMICs are the "Heat Sources" which determine the temperature of the substrate. A simple approximation to the real array in air is to assume that both the top and bottom surfaces are thermally isolated so no heat is removed from these surfaces. The vertical sides of the substrate are assumed to be in contact with an ideal heat sink which keeps the sides at a constant temperature. The ideal heat sink only removes heat through the vertical sides.

We start the thermal analysis, in order to solve for temperature profile $T(x, y, z)$, with the fundamental equation describing the substrate in thermal steady state with no internal heat sources [20] given by

$$\nabla^2 T(x, y, z) = 0 \tag{2.1}$$

As is commonly done when solving partial differential equations, a substitution of variables (see Figure 2.5) is applied as follows

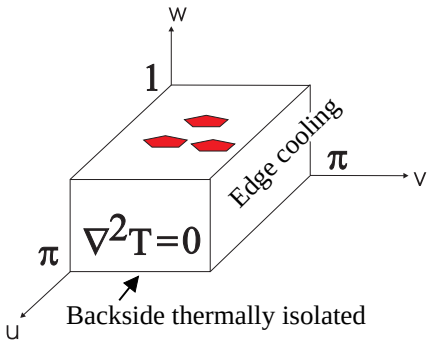

Figure 2.5: Schematic of thermal problem in normalized coordinates.

$$u = (x - x_0)\pi/a \tag{2.2}$$

$$v = (y - y_0)\pi/b \tag{2.3}$$

$$w = (z - z_0)/c \tag{2.4}$$

The concise description of the thermal problem in normalized coordinates with all the boundary conditions is therefore

$$\nabla^2 T = 0 \quad \text{with} \tag{2.5}$$

$$T_w(u, v, 1) = -\frac{c}{kA_H}\frac{dQ(u, v)}{dt} \tag{2.6}$$

$$T_w(u, v, 0) = 0 \tag{2.7}$$

$$T(0, v, w) = T(\pi, v, w) = 0 \tag{2.8}$$

$$T(u, 0, w) = T(u, \pi, w) = 0 \tag{2.9}$$

where: c is the thickness of the substrate; k is the thermal conductivity of the substrate; A_H is the area of contact between each MMIC and the substrate; and $\frac{dQ}{dt}$ is the heat-flow rate in watts. The notation T_w represents the partial derivative of temperature with respect to w. The boundary condition $T_w(u,v,1)$ is the mathematical statement that the MMICs are the sources of heat. The boundary condition $T_w(u,v,0) = 0$ describes the fact that the bottom surface is thermally isolated and no heat flows out of the bottom surface. Finally, the remaining boundary conditions on the sides describe the ideal heat sink which keeps the sides at a constant temperature.

Eqn.(2.9) can be solved analytically to determine the temperature profile of the array. Separation of variables is applied to Eqn.(2.9) and the temperature profile is determined to be

$$T(u,v,w) = \frac{P_H}{kA_H}\tilde{T}(u,v,w) \tag{2.10}$$

$$\tilde{T}(u,v,w) = \sum_{m=1}^{\infty}\sum_{n=1}^{\infty}\tilde{A}_{mn}\sin(mu)\sin(nv)\cosh(\gamma_{mn}w) \tag{2.11}$$

$$\tilde{A}_{mn} = -\frac{16}{\pi^2}\frac{\sin(\frac{m\pi}{2})\sin(\frac{m\pi}{2}f_1)\sin(\frac{n\pi}{2})\sin(\frac{n\pi}{2}f_2)}{mn\frac{\gamma_{mn}}{c}\sinh(\gamma_{mn})} \tag{2.12}$$

$$\gamma_{mn} = c\pi\sqrt{\left(\frac{m}{a}\right)^2 + \left(\frac{n}{b}\right)^2} \tag{2.13}$$

where P_H is the power wasted as heat by an individual MMIC; $f_1 \equiv \frac{w_{\text{MMIC}}}{a}$ is defined by the ratio of MMIC width to the substrate width; and $f_2 \equiv \frac{l_{\text{MMIC}}}{b}$ is defined by the ratio of MMIC length to substrate length. Due to RF array considerations that will be explained later, a triangular layout of MMICs is utilized which defines the particular geometrical factors: $\tilde{T}$, $\tilde{A}_{mn}$, and γ_{mn}.

Insight into the parameters that control the temperature of the QO amplifier is gained by studying Eqn.(2.10). The $\tilde{T}$ factor depends solely on positions of the MMICs. Careful inspection of $\tilde{T}$ reveals that the temperature of the array can be decreased by placing the MMICs as far away from each other as possible. In other words, from thermal

considerations, it is best to have a large array spacing. As will be shown later, this is contrary to the desired array spacing based on RF considerations. The temperature is also proportional to the heat P_H generated by each of the MMICs in the array. Therefore, it is best to choose highly efficient MMICs with lower P_H. The temperature is inversely proportional to the area of a single MMIC (A_H). The temperature of the array can be lowered by using MMICs with a large area of contact (A_H). However, this increases the unit cell size and as will be shown later, adversely affects the array radiation pattern. The temperature is also inversely proportional to the thermal conductivity of the substrate.

What if the edge temperature is not zero but rather a constant T_{edge}? In that case, the solution is given by superposition of T_{edge} and the temperature profile given by Eqn.(2.10) Recall that Eqn.(2.10) was derived with the edge temperature equal to zero. The solution $T(u, v, w) + T_{edge}$ is easily verified by substituting it back into Eqn.(2.9) and confirming that the boundary conditions are still satisfied.

2.3.2 Which substrate? Eqn.(2.10) makes it possible to compare the thermal performance of some available and promising substrates. The choice of substrate is constrained by the approximate 100°C maximum operating temperature of the MMIC. Thermal gradients on substrates during operation are approximated with the simple analytical model of heat conduction [Eqn.(2.10)]. Let the model assume a uniform heat flux due to each MMIC, and a uniform temperature of 25°C is maintained along the edge of the substrate. Let the substrate dimensions be 7.62 cm-by-7.62 cm-by-h (a convenient commonly available size), where the substrate thickness h for commercially available substrates varies between 254 μm and 406 μm. Assume an array has 36 unit cells spaced 9 mm ($0.9\lambda_0$ at 31 GHz) apart. 36 *Alpha* AA028P3-00 MMICs are required to produce watt level output power. The 36 *Alpha* AA028P3-00 MMICs will produce at most 33 W of total heat ($P_{H,t} = 33$ W).

The maximum expected temperatures based on the conduction model for diamond, aluminum nitride (AlN), and *Rogers* TMM6 substrates are given in Table 2.2. The diamond

Table 2.2: The theoretical maximum temperature based on conduction only.

Substrate	h (μm)	k (W/(m K))	$P_{H,t}$ (W)	Cost \$	T_{max} (°C)
Diamond	406.4	2000	33	10000	30.3
AlN	254	170	33	400	124
TMM6	381	0.7	33	30	15000

substrate has the lowest thermal gradient but is also at least 25 times more expensive than AlN. The unrealistic maximum temperature calculated for the TMM6 substrate demonstrates the limitation of any model based solely on heat conduction. However, at higher temperatures, cooling is dominated by convection and radiation which will decrease the maximum temperature given in Table 2.2, making these tabulated values absolute maxima. For substrates with high thermal conductivity, the surface temperature of the substrate is relatively low which tends to reduce the effects of thermal radiation and convection; consequently, the thermal conduction model is best suited for high thermal conductivity substrates.

As was stated earlier, at high temperatures not only the MMIC can be destroyed by high temperatures but the substrate itself may also be affected. In fact, early in this project, Lockheed-Martin (LM) fabricated one of our first designs on a proprietary LM diamond substrate with custom high-power (1 W) MMICs. The diamond substrate failed. A layer of "carbonized" material was visible after the array operated for a short amount of time. This failure and the fact that diamond is expensive discouraged its future use for the arrays in this thesis.

The AlN substrate was chosen over diamond because its 100°C thermal gradient (see Figure 2.6) meets the MMIC temperature requirements and the substrate is comparatively inexpensive. The AlN substrate is 254 μm thick with a relative permittivity of 8.6. One problem with AlN is the fact that the dielectric loss tangent of AlN is unknown at Ka-band. At X-band, AlN is well characterized with a low dielectric loss tangent. For design purposes, the dielectric loss tangent is assumed to be zero. This assumption turns out to be acceptable

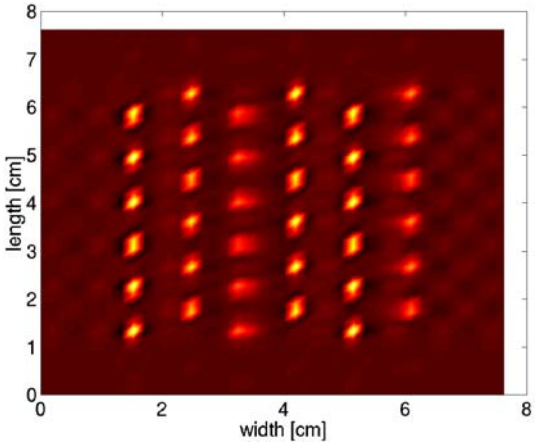

(a) Heat Sources

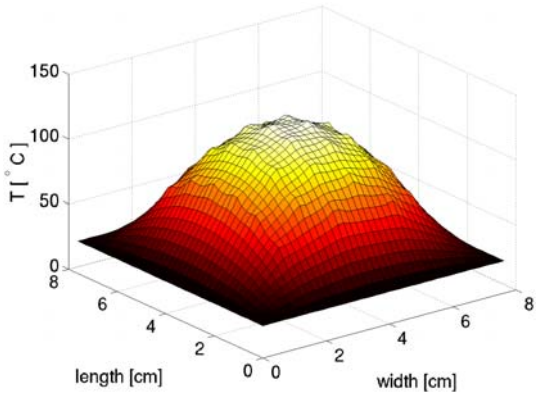

(b) Temperature Profile

Figure 2.6. Theoretical temperature on the surface of the AlN substrate is plotted as a function of position. The "spikes" in the temperature distribution are due to the finite area of individual MMICs. The maximum temperature shown is 124°C.

based on measured results (Chapter 3).

2.3.3 Drawbacks of liquid coolant The AlN is a very good thermal conductor but it is still very poor compared to diamond. Based on the thermal conduction model presented in the previous section, the AlN substrate just meets the thermal requirements, barely. In the early stages of this thesis, the possibility of cooling the array more with liquid coolant was pursued. Based on thermal calculations, a liquid coolant flowing over the back of a thin substrate could dramatically reduce the maximum operating temperature, independent of the substrate used.

The solution that was envisioned is shown in Figure 2.7. A low-loss quartz layer

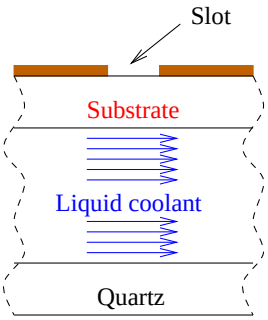

Figure 2.7: Liquid coolant diagram.

would be used to contain a low-loss liquid coolant. The liquid coolant would flow over the back of the array surface and remove excess heat.

The problem with this approach turned out to be the reduction of efficiency of the antenna when the coolant was added. Figure 2.8 shows the theoretical radiation patterns for two slot antennas; one without coolant and the other with liquid coolant. Both antennas were individually designed to have a $50\,\Omega$ input impedance at resonance. The radiation pattern was affected adversely by the coolant and became unacceptable for incorporation into an array due to the bore sight null and high side lobes (right hand side in Figure 2.8). Furthermore, the radiation efficiency dropped from a reasonable 80% to only 40% when the coolant was added. Such a low radiation efficiency is not acceptable for any power-combiner

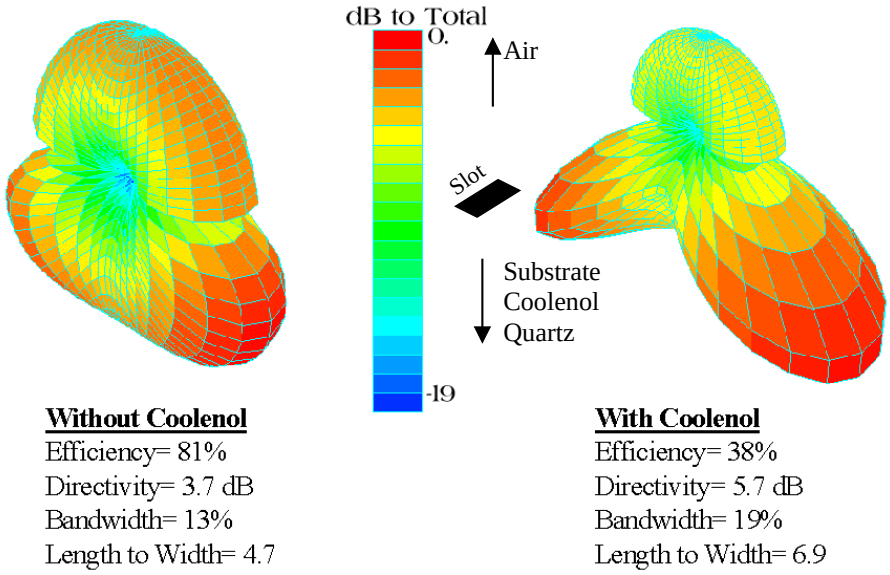

Figure 2.8. Effect of liquid coolant (*Coolenol*) on antenna performance. The normalized far-field power is plotted for two cases; with and without coolant.

design. Note that any thick substrate would have similar problems and is therefore not a practical alternative to a thin substrate with high thermal conductivity.

2.4 RF analysis - Sub array design

The particular design of RF array elements depends highly on the particular substrate chosen. AlN was chosen to be the substrate because of its high thermal conductivity. The relative permittivity, $\epsilon_r = 8.5$ for AlN, determines the precise dimensions of each passive array component in the QO amplifier. The dielectric losses, $\tan\delta$=0.0039 at 10 GHz for AlN [18], should not affect the QO amplifier efficiency and the peak output power of the QO amplifier.

Only after the substrate is chosen and its RF properties are known is it possible to design the particular array components (antennas and transmission lines). The first goal of this section is to explain why certain RF elements were chosen over others. For instance, why is the CPW transmission line more desirable than the microstrip transmission line. The

second goal of this section is to give the final design of the antennas, transmission lines, and transmission-line bends used in the final QO amplifier.

2.4.1 Antenna design Closed-form analytical solutions to Maxwell's equations for general antenna designs are rare and exist in only the simplest cases. For example, the Hertzian dipole is a well known antenna with an analytical solution. However, the kinds of antennas that are likely to be fabricated on a thin planar substrate such as AlN cannot be described by simple analytical models. The design of antennas and other RF array components on planar substrates relies heavily on numerical models. The consequence of relying on numerical models is that the design of antennas is based on iterative CAD.

Due to the fabrication techniques available at the University of Colorado (described later in Chapter 3.1) and the inability to tune individual unit cells after fabrication, it is decided that a large antenna bandwidth is desired to avoid dependence on high-precision fabrication. Patch antennas are commonly used because they are well understood and characterized with a simple accurate cavity model [8]. The problem with using patch antennas is their low bandwidths. Slot antennas typically have higher bandwidths than patch antennas. Figure 2.9 gives the real and imaginary parts of input antenna impedance as a function of frequency for a slot antenna. The impedance is calculated with *WireZeus*, a MOM code that uses entire-domain basis functions to numerically calculate the antenna currents. *WireZeus* simplifies the problem and treats the slot antenna as a dielectrically coated dipole (Booker's Duality Principle [21]). Figure 2.9 shows that second-resonance slot antennas have large bandwidths due to a less-steep zero crossing of the imaginary impedance. Another antenna with an even larger bandwidth that was considered was the folded-slot antenna [22, 23]. However, the area of the folded-slot antenna was determined to be too large for this application.

Once the slot antenna is chosen, the specific type of feed still needs to be determined. *WireZeus* models the feed as a small point generator, which is not a realistic practical

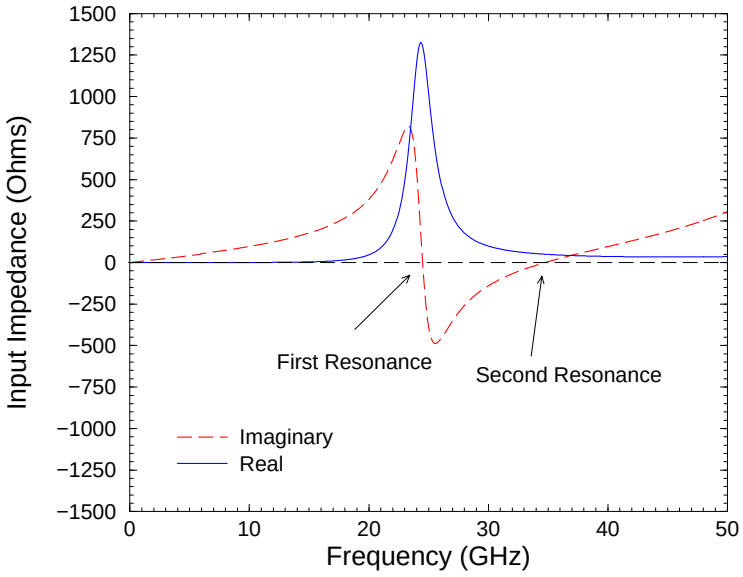

Figure 2.9. *WireZeus* simulation for the real and imaginary components of input impedance versus frequency shows the benefit of using a slot at its second resonance.

feed. Three commercially available CAD programs are employed to more accurately model the CPW feed: *Momentum* by Agilent, formerly Hewlett Packard; *Ensemble* by Ansoft Corporation; and *IE3D* by Zealand Corporation. All three models are based on Method of Moments (MOM) solutions for planar structures with sub-domain basis functions which can model the slot antenna and the feed numerically without resorting to Booker's Duality Principle. The feed can either be a microstrip (MS) or CPW transmission line.

Figure 2.10 summarizes most of the different slot antenna feed configurations that were considered for the QO amplifier. All the antennas are designed to have an input impedance of 50 Ω at 33 GHz. The first three antennas (a),(b),(c) are simulated with *Ensemble*. Antennas (a)–(c) are fed with a microstrip line (shown as a thin vertical line). The slot antenna (shown as a wide horizontal rectangle) is cut in the ground plane of the microstrip line. This requires metalization on both sides of the substrate and precise alignment of the two sides. Antenna (a) has its feed in the center and has a bandwidth of 11%. Antenna

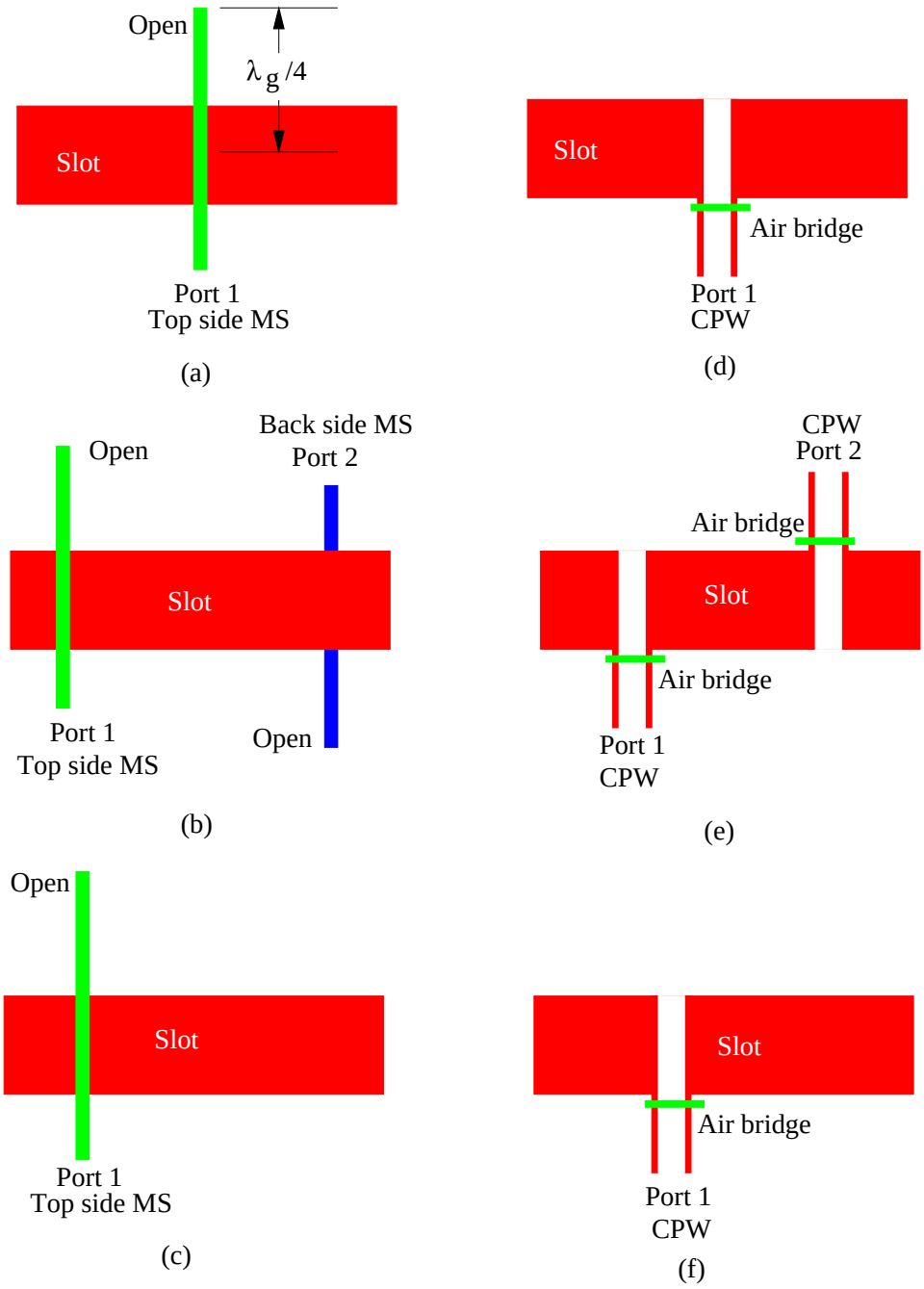

Figure 2.10. Sketches of different slot antenna feeds considered for the QO amplifier. Two types of feeds are compared: microstrip (a-c) and CPW (d-f). Unlike the CPW feeds, the microstrip feeds require an open at $\lambda_g/4$. For each feed type, three different port locations are used: center, dual off-center, and off-center. Depending on the port location, the slot width and length are determined such that terminal impedance is $50\,\Omega$. The 2:1 VSWR bandwidth for each case is calculated: (a) 11%; (b) 21%; (c) 7%; (d) 17%; (e) 9%; (f) 7%.

(b) has dual off-center feeds with a large bandwidth of 21%. The idea behind the dual feed is to use the same antenna for input and output power and reduce unit cell size [7]. This turns out to be unusable because the coupling between the two ports is too large which enhances the possibility of oscillations. Antenna (c) has an offset feed which lowers the bandwidth.

The last three antennas (d),(e),(f) are modeled using both *Momentum* and *IE3D*. Antennas (d)–(f) simply replace the microstrip feed with a CPW feed. This configuration requires that only one side of the substrate is metalized which greatly simplifies fabrication. The CPW feed and the slot are on the same side of the substrate which removes the problem of alignment of feed line to antenna during fabrication. Again the bandwidth of the center fed slot (17%) is better than that of the off-center fed slot (7%). The center-fed CPW slot antenna has a higher bandwidth than the center-fed microstrip slot antenna. In conclusion, the CPW-center-fed slot antenna shown in Figure 2.10(d) is chosen for its high bandwidth, small size, and ease of fabrication.

The final antenna is designed using *HP Momentum* to have a 50-Ω terminal impedance. The model requires a 0.2 mm ($\lambda_0/50$ at 30 GHz) edge mesh to accurately sample the magnetic current near the edges of the slot where the fields vary rapidly. A typical theoretical near-field distribution demonstrates this rapid variation (see Figure 2.11). Everywhere else a mesh with 30 cells per wavelength (mesh frequency of 40 GHz) is sufficient for the input impedance to converge. The model requires 8 Megabytes (matrix size of 710 unknowns) and 4 minutes per frequency point on an HP workstation. In summary, the second-resonance slot antenna is 4.15 mm long and 0.9 mm wide, and has a modeled return loss of 50 dB at 33 GHz (see Figure 2.12) with a 13% 2:1 VSWR bandwidth (without polarizers that are actually used in the array to enforce unidirectional radiation). The theoretical radiation efficiency of a single slot antenna is 70% (-1.52 dB) based on *IE3D*. *IE3D* is the only numerical tool we have available that has the capability of calculating radiation efficiency. 30% of the power loss is due to ohmic losses in the metal and substrate modes.

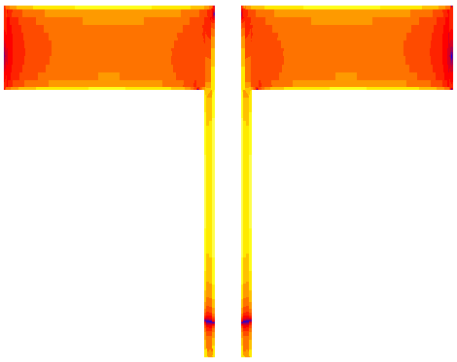

(a) Total magnetic current density

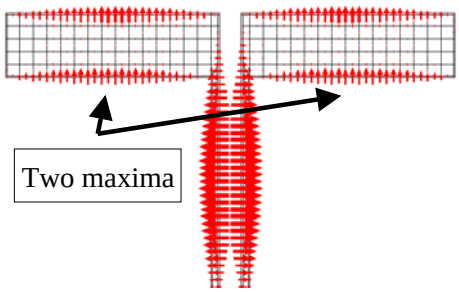

(b) Total electric field intensity

Figure 2.11. Theoretical current of second-resonance slot antenna shows two maxima located symmetrically about the CPW feed. The total magnetic current density (a) and the electric field intensity (b) are calculated over a variable mesh; consequently, the intensity maxima are on the slot edges where the smallest mesh is located.

2.4.2 Transmission lines and discontinuities Recall, the CPW transmission line was chosen over the microstrip line to alleviate the problem of aligning the feed to the slot antenna during fabrication. Both the CPW and microstrip lines are well characterized, have analytical models, and are easily designed. Based on a textbook analytical model of CPW lines [24], the dimensions of a CPW line are found by solving a transcendental equation. To achieve a CPW line with a $50\,\Omega$ characteristic impedance on AlN, the width of the center CPW conductor (W_{CPW}) is found to be $225\,\mu$m and the gap spacing (S_{CPW}) is $75\,\mu$m. This solution to the transcendental equation agrees exactly with the *LineCalc* solution that is packaged with *Momentum*.

Recall from Figure 2.3 that the input antenna is attached to a CPW line that has

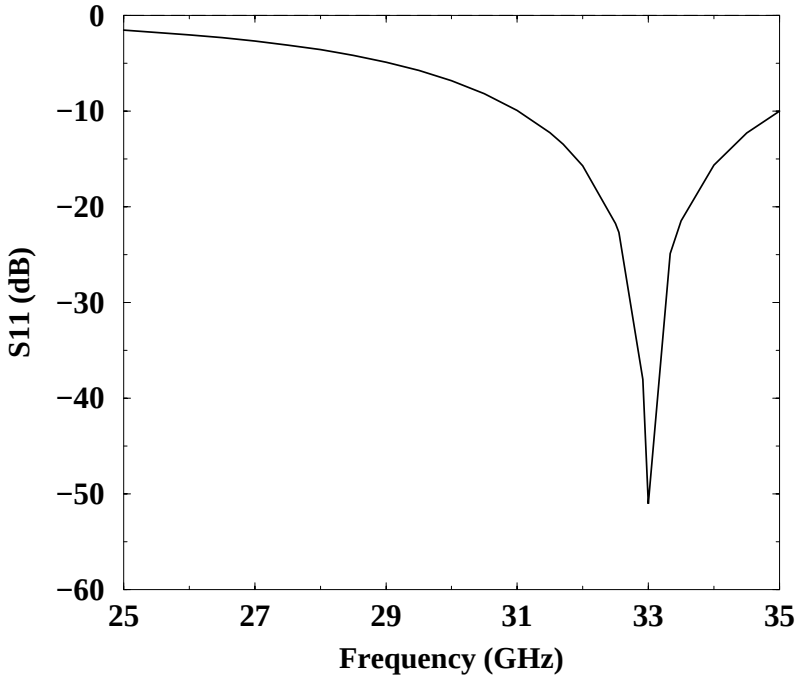

Figure 2.12: *Momentum* characterization of ideal slot antenna design on AlN.

a 90° bend. The effect of the 90° bend has no simple analytical description. However, the 90° compensated bend is easily modeled by *Momentum*. The precise model is shown in Figure 2.13(a). Discontinuities such as the 90° bend are known to excite the unwanted slot line mode of the CPW line which radiates. The air bridges are required to suppress radiation from the CPW line.

Figure 2.13(b) summarizes the theoretical performance of the 50 Ω CPW line based on the *Momentum* model. The return loss is better than 17 dB and the insertion loss is less than 0.2 dB over the 25-35 GHz frequency range. Even with the 90° bend and the air bridges, the RF performance of the CPW design is acceptable.

2.5 Array factor considerations

With the MMIC chosen and the sub-array elements designed, the unit cell size can be determined based on two considerations: mutual coupling effects and the radiation pattern

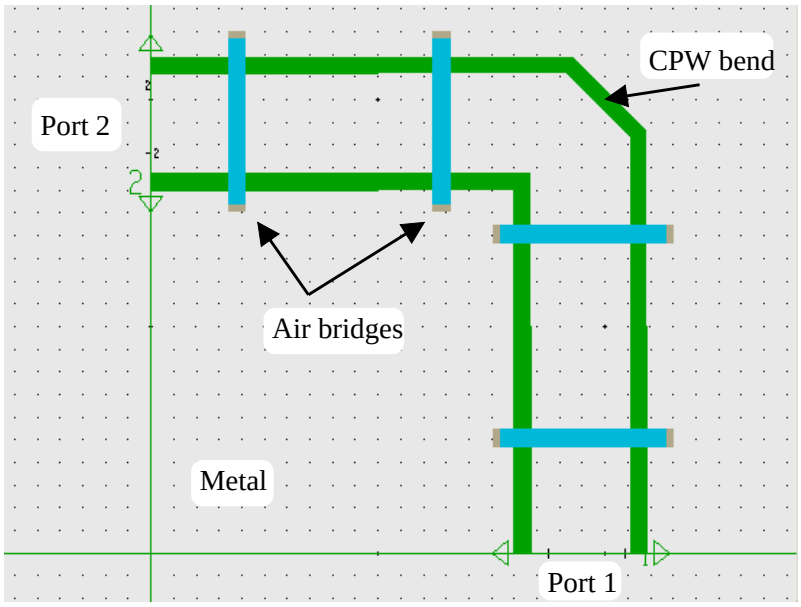

(a) Geometry

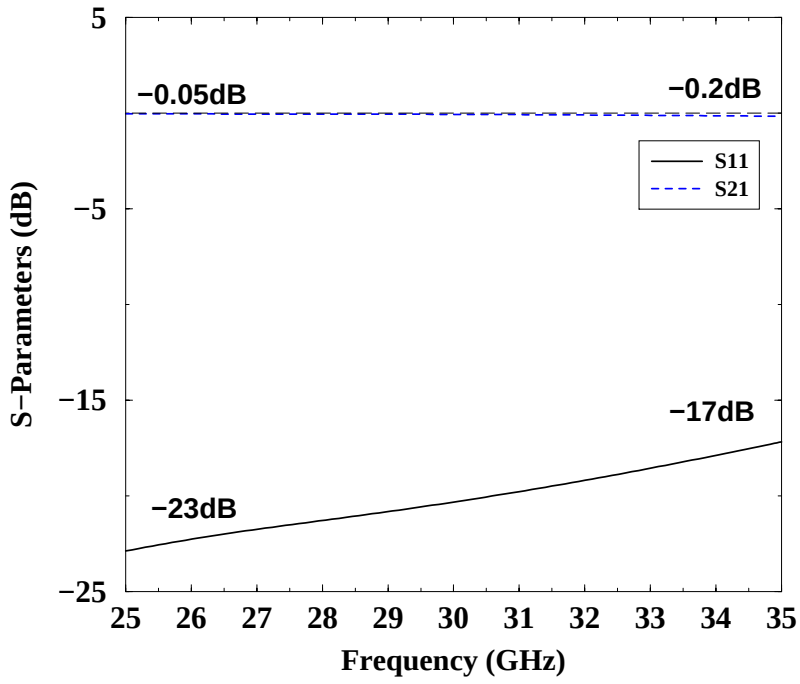

(b) Theoretical

Figure 2.13. The layout of the CPW line with a 90° bend and air bridges is shown in (a). The theoretical S-parameters (b) are calculated using *Momentum*.

of the array. The effects of mutual coupling are difficult to study without first knowing the unit cell design. However, as will be explained in a later section (see Section 2.7), mutual coupling tends to dictate a large unit cell on the order of λ_0, depending on the gain of the MMIC. A large unit cell affects the radiation pattern of the array since the array factor (recall Eqn.(1.50)) is determined by the unit cell size and the particular array lattice. In this section, the array factor is used to determine the bounds on the unit cell size and to compare the rectangular and and triangular array lattices.

Recall from Eqn.(1.49) that the total radiation pattern of the array is the product of the array factor and the individual antenna pattern. The individual slot antenna used in the QO amplifier has the theoretical *IE3D* radiation pattern shown in Figure 2.14. The slot is oriented with its polarization in the y-direction with the back side (non-metalized side) of the substrate facing up ($\theta = 0°$). Notice that the radiation pattern is 1 dB higher at $\theta = 0°$ than at $\theta = 180°$. For this reason, the output side of the array (driven by the high gain MMICs) is in the $\theta = 0°$ direction, opposite the side with MMICs. For clarity, the E- and H-plane radiation patterns are plotted in Figures 2.14(b) and (c).

The final array design uses a triangular array lattice with a $0.92\lambda_0$ array spacing (recall Figure 2.3). The reason for the triangular lattice, as opposed to the rectangular lattice, is demonstrated graphically in Figure 2.15. The E-plane array factor is calculated for both the rectangular (a) and the triangular (b) lattices. The rectangular lattice (a) has large side lobes at $\theta = \pm 90°$ but the triangular lattice does not. Hence, the triangular lattice is chosen to suppress E-plane side lobe radiation.

The effect of array spacing on the array factor is shown in Figure 2.16. As the unit cell size increases from (a) $0.50\lambda_0$ to (c) $0.92\lambda_0$, unwanted H-plane side lobes at $\theta = \pm 90°$ increase. Note that the total H-plane pattern of the array (d) has reduced side lobe levels due to the toroidal H-plane pattern of the slot antenna. Ideally, the unit cell size should be as small as practically possible to reduce side lobe radiation which can not be collected by

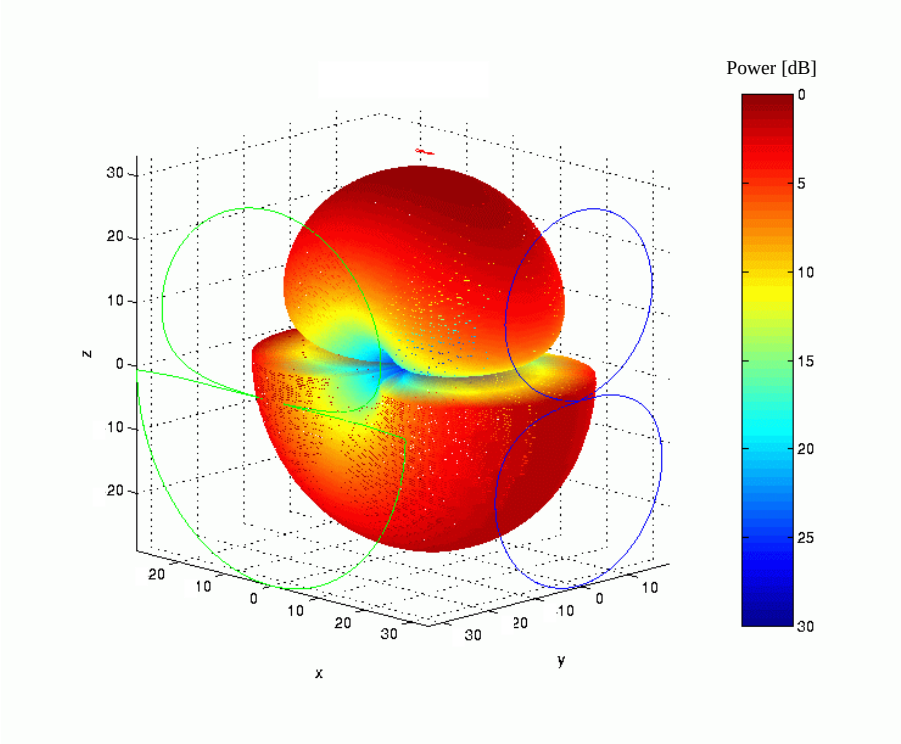

(a) Single slot antenna

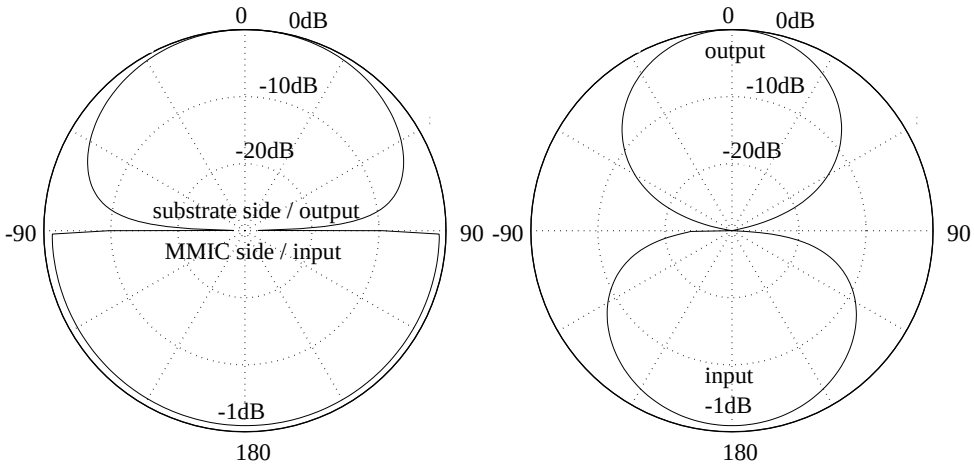

(b) E-plane

(c) H-plane

Figure 2.14. Theoretical *IE3D* far-field normalized-power pattern of a single y-polarized slot antenna. The Cartesian axes in (a) are for referencing the orientation of antenna and the scale in [dB] refers to the polar radius only. The E- and H-planes are plotted in (b) and (c), respectively.

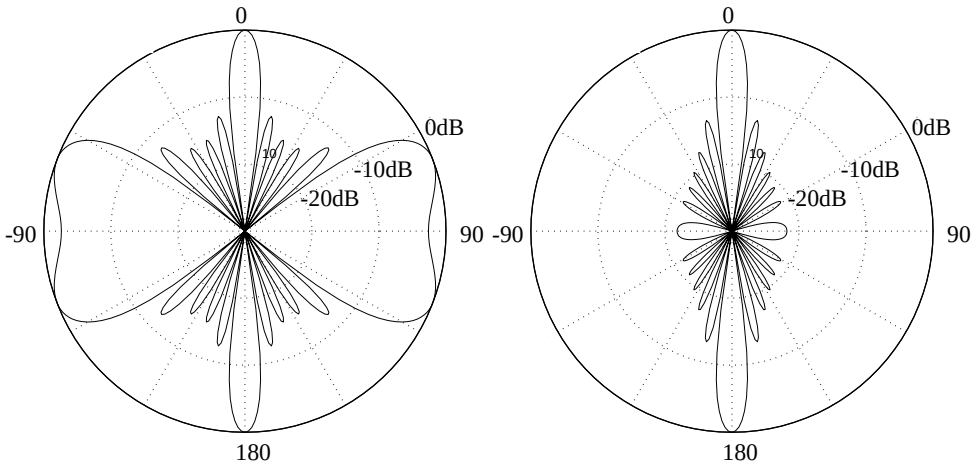

(a) Rectangular AF

(b) Triangular AF

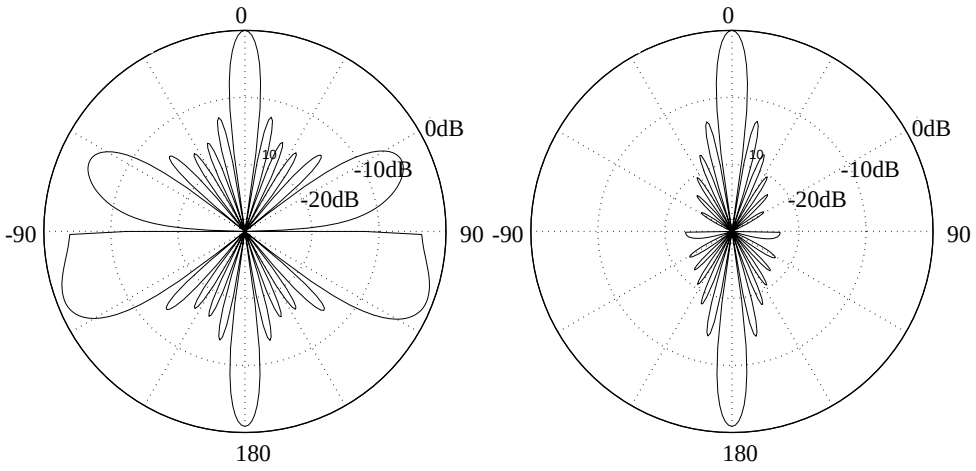

(c) Rectangular AF × Slot

(d) Triangular AF × Slot

Figure 2.15. Comparison between the rectangular and triangular lattices for a 6×6 array. The unit cell size is 9 mm ($0.92\lambda_0$). The normalized E-plane radiation patterns are shown for: (a) rectangular and (b) triangular lattices of isotropic antennas; and (c) rectangular and (d) triangular lattices of slot antennas. The triangular lattice (b) suppresses the side lobes at $\theta = \pm 90°$. The total E-plane radiation pattern (AF × Slot pattern) is shown for the (c) rectangular and (d) triangular lattices.

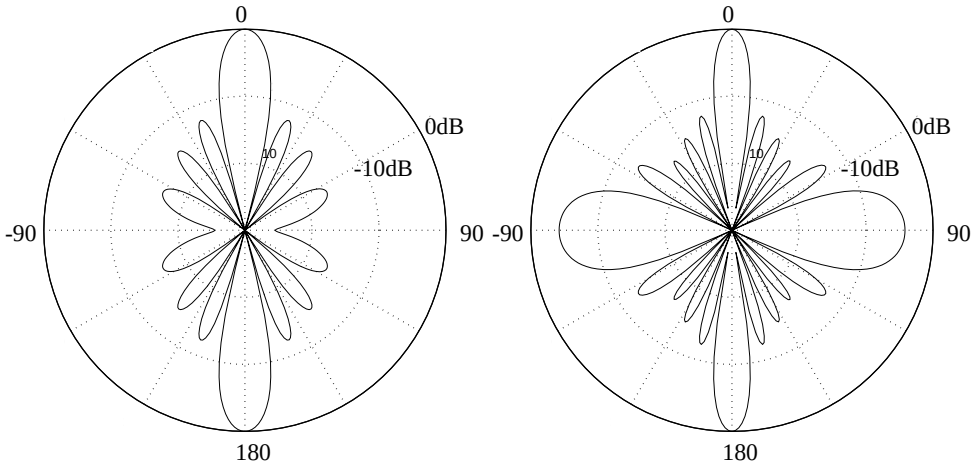

(a) $0.50\lambda_0$, AF

(b) $0.77\lambda_0$, AF

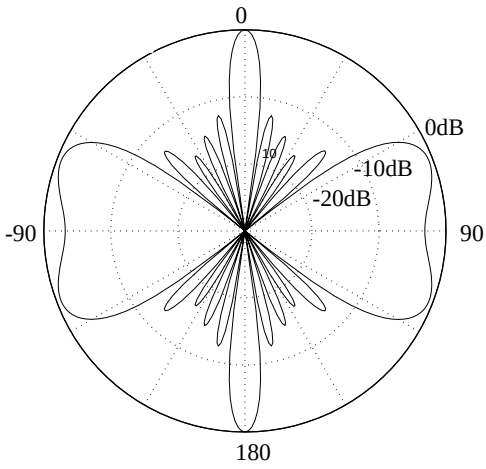

(c) $0.92\lambda_0$, AF

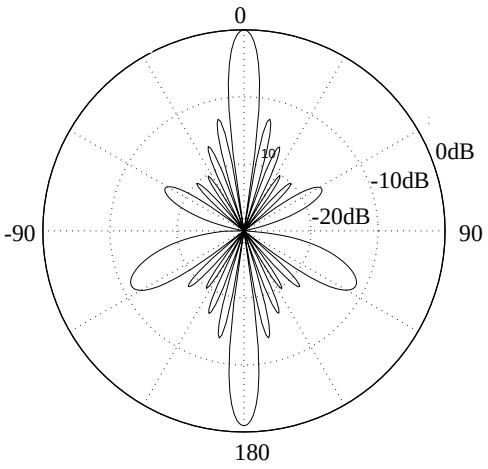

(d) $0.92\lambda_0$, AF $\times$ Slot

Figure 2.16. The effect of unit cell size on the normalized H-plane pattern of a 6×6 triangular lattice array. The array factor is plotted for increasing unit cell size: (a) $0.50\lambda_0$; (b) $0.77\lambda_0$; (c) $0.92\lambda_0$. When the actual toroidal pattern of the slot antenna is taken into account (d), the large side lobe from the $0.92\lambda_0$ AF (c) is decreased by 10 dB.

the receive horn in a QO amplifier system.

As shown in the previous figures, the slot antenna radiates in both the $\theta = 0°$ and $180°$ directions; consequently, half the power is lost in the $\theta = 180°$ direction. To overcome the bi-directional radiation pattern of the slot antenna, a polarizer is placed a distance (h) in front of the array on the input side to enforce unidirectional radiation of the array. In [1], the polarizer is modeled as an infinite ground plane placed $\lambda/4$ away from an array of ideal Hertzian dipoles and the array aperture efficiency is used to quantify the effect of the polarizer. The calculation of aperture efficiency is now repeated except that the ideal Hertzian dipoles are replaced by slot antennas on AlN.

The aperture efficiency is defined as the ratio of the effective area of the array to the physical area of the array aperture:

$$\eta_a = \frac{A_{\text{eff}}}{A_{\text{phys}}} \tag{2.14}$$

The effective area of the array is related to the directivity (D) of the array by

$$A_{\text{eff}} = \frac{\lambda^2}{4\pi}\eta_r D \tag{2.15}$$

where η_r is the antenna efficiency. The directivity is calculated from the total radiation pattern

$$D = \frac{4\pi}{\oint |AF(\theta,\phi)|^2 |P(\theta)|^2 |F(\theta,\phi)|^2 d\Omega} \tag{2.16}$$

where AF is the array factor and F is the single slot radiation pattern. The polarizer is taken into account by applying the method of images and defining P to be

$$P(\theta) = \begin{cases} \sin(2\pi/\lambda h \cos\theta) & \text{with polarizer,} \\ 1 & \text{without polarizer.} \end{cases} \tag{2.17}$$

Figure 2.17 compares the theoretical aperture efficiency with and without the polarizer for a 6×6 array of slot antennas as a function of unit cell size assuming $\eta_r = 1$. Note that aperture efficiencies greater than one are not physically realizable due to the physical size of

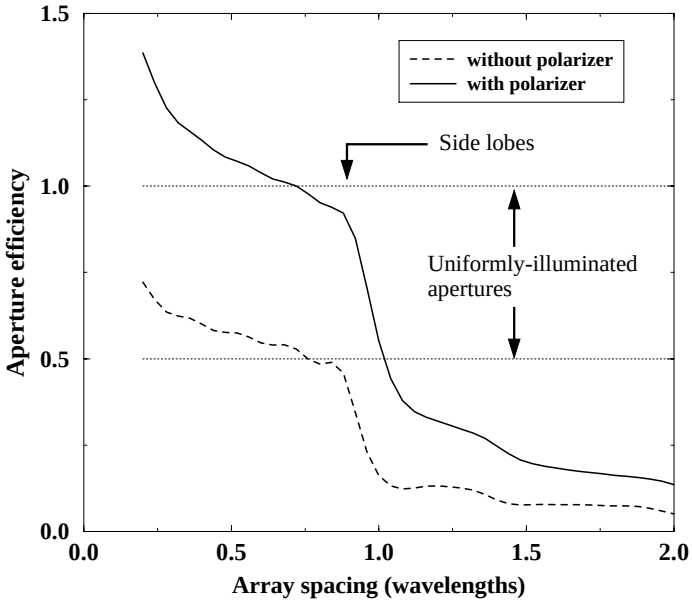

Figure 2.17. Theoretical aperture efficiency ($\eta_a = A_{\text{eff}}/A_{\text{phys}}$) is plotted as a function of normalized unit cell size (or array spacing) for a 6×6 array of slot antennas. The individual slot radiation pattern is calculated using *IE3D*.

antennas and mutual coupling which are ignored in this calculation. As the array spacing increases, side lobes appear and the aperture efficiency rapidly decreases which confirms the prior observations shown graphically in Figure 2.16. As expected, the aperture efficiency approximately doubles when the polarizer is added. Hence, the polarizer accomplishes the goal of enforcing unidirectional radiation of the QO amplifier array.

In conclusion, the triangular array lattice is chosen to suppress E-plane side lobe radiation. In the H-plane, side lobes are eliminated due to the toroidal pattern of the slot antenna. Ideally, the array spacing should be as small as possible to maintain unity aperture efficiency and should not exceed $0.92\,\lambda_0$ to maintain $A_{\text{eff}}/A_{\text{phys}} > 0.85$. The small array spacing is difficult to achieve due to mutual coupling effects (see Section 2.7); consequently, a compromise between aperture efficiency and mutual coupling determines the final array spacing of 9 mm ($0.92\lambda_0$).

2.6 DC analysis and bias design

There is inevitably a DC-voltage variation across the array due to ohmic losses in the bias lines and large current densities in QO power amplifiers. The gravity of this problem was first realized from a near-field measurement (details in Chapter 4) of the x-directed electric fields of our first working array (named Array 0). The near-field measurement (see Figure 2.18) shows that only 20% of the elements in the active array are functional. A

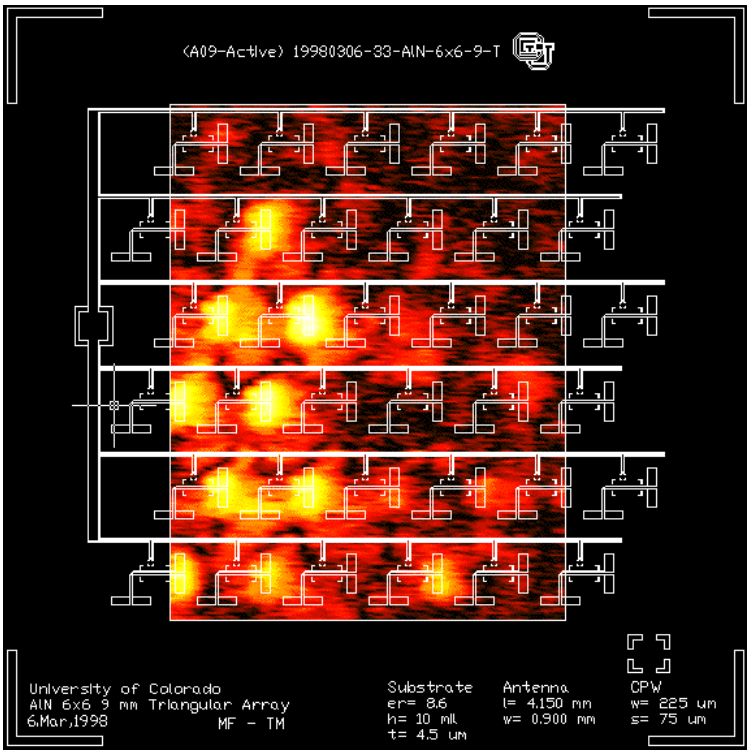

Figure 2.18. The measured near-field of an array with poor bias design. In this case, the bias line is thin (high resistance) which causes a rapid decrease in voltage from the bus bar (left side) to the farthest unit cell MMIC (right side). This array is effectively a 2-by-5 active array; the majority of MMICs simply do not have enough DC bias to turn on.

DC-voltage variation affects the gain of each of the MMICs in the array. As a result, the gain of the MMICs tends to drop the farther they are from the DC voltage source (bus bar). The lower gain MMICs contribute less power and the total output RF power of the array is reduced below the ideal. The goal of this section is to derive an equation describing the

voltage variation which will help improve DC bias design and improve array performance.

The biasing network for a row is modeled as a resistive ladder network consisting of series, $R_{\rm bias}$, and shunt, $R_{\rm MMIC}$, resistors (Figure 2.19). The variables $R_{\rm bias}$ and $R_{\rm MMIC}$

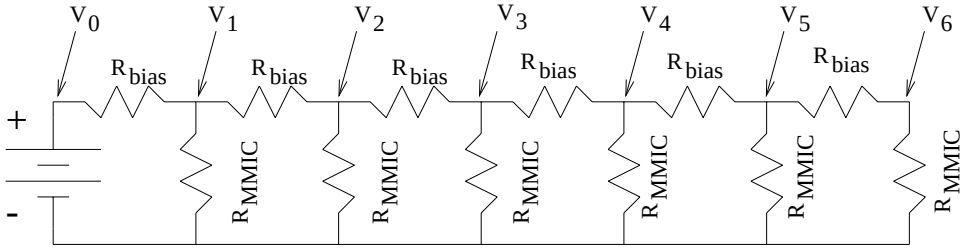

Figure 2.19. Resistive ladder network diagram used to calculate MMIC bias levels within the array.

represent the resistance of the unit-cell bias line and the resistance of the internal MMIC biasing circuitry, respectively. In particular, the unit-cell bias line resistance is given by

$$R_{\rm bias} = \left[\frac{w_{\rm bias}}{l_{\rm UC}}(t_{\rm Cu}\sigma_{\rm Cu} + t_{\rm Au}\sigma_{\rm Au})\right]^{-1} \tag{2.18}$$

where $w_{\rm bias}$ is the width of the bias line, $l_{\rm UC}$ is the distance between adjacent MMICs (the unit cell dimension), t is the thickness of the substrate metalization, and σ is the conductivity of the metal. The subscripts "Cu" and "Au" refer to the copper and gold layers, respectively. Eqn.(2.18) is written to allow the possibility of two metal layers for the improvement of R_{bias} during fabrication. The bias voltage along a row at the $(k+1)$ unit cell is given by:

$$V_{k+1} = \alpha_{N-k-1}^{-1} V_k \qquad \text{, where} \tag{2.19}$$

$$\alpha_k = \frac{R_{\rm bias} + R_k}{R_k} \qquad \text{, and} \tag{2.20}$$

$$R_j = \left[\frac{1}{R_{\rm MMIC}} + \frac{1}{R_{\rm bias} + R_{j-1}}\right]^{-1} \tag{2.21}$$

The number of unit cells in a row is N, j=1 to N-1, and k=0 to N-1. k=0 corresponds to the supply voltage V_0 and $R_0 \equiv R_{\rm MMIC}$.

Eqs.(2.19) and (2.21) expressed as a function of the ratio $R_{\rm MMIC}/R_{\rm bias}$, confirm that the bias voltage variation over a row may be substantial (Figure 2.20). The conclusion

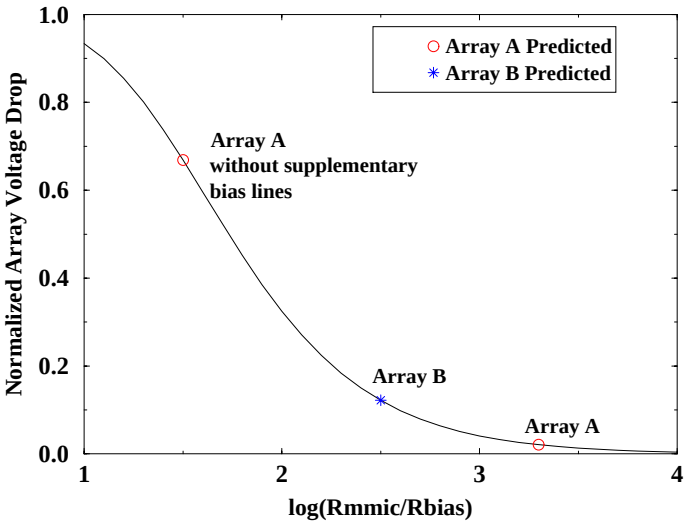

Figure 2.20: Normalized array voltage drop plotted as a function of $R_{\mathrm{MMIC}}/R_{\mathrm{bias}}$.

from Figure 2.20 is that the ratio $R_{\mathrm{MMIC}}/R_{\mathrm{bias}}$ needs to be as large as possible to achieve a small voltage variation.

An even larger voltage drop can be expected since each row is in turn connected to the DC bus bar. The bus bar is the long vertical rectangle shown on the left side in Figure 2.3. The DC power supply is connected to the bus bar at a single location (either at the lower left pad or at the upper right pad). Similar to the voltage drop along a row, there is a voltage variation along the bus bar described by

$$V'_{k+1} = \beta^{-1}_{N-k-1} V'_k \quad \text{, where} \tag{2.22}$$

$$\beta_k = \frac{R_{\mathrm{bus}} + R'_k}{R'_k} \quad \text{, and} \tag{2.23}$$

$$R'_j = \left[\frac{1}{R_{N-1}} + \frac{1}{R_{\mathrm{bus}} + R'_{j-1}} \right]^{-1} \tag{2.24}$$

where the impedance of the bus bar is

$$R_{\mathrm{bus}} = \left[\frac{w_{\mathrm{bus}}}{l_{\mathrm{UC}}} (t_{\mathrm{Cu}} \sigma_{\mathrm{Cu}} + t_{\mathrm{Au}} \sigma_{\mathrm{Au}}) \right]^{-1} \tag{2.25}$$

and R'_0 is determined by the impedance of an entire row ($R'_0 = R_{\mathrm{row}} = R_{N-1}$). In a sense, R_{row} is analogous to R_{MMIC}. The consequence is that the ratio of $R_{\mathrm{row}}/R_{\mathrm{bus}}$ must be large

to decrease the total array voltage drop. In effect, the ratio of $R_{\text{row}}/R_{\text{bus}}$ places a limit on the maximum number of unit cells possible in any active array.

From the previous Eqs.(2.19) and (2.22), the MMIC voltage at the (i, j) unit cell is finally summarized by

$$V_{0,0} = V_0 \tag{2.26}$$

$$V_{0,j} = \prod_{m=0}^{j-1} \alpha_{N-m-1}^{-1} \tag{2.27}$$

$$V_{i,0} = \prod_{n=0}^{i-1} \beta_{N-n-1}^{-1} \tag{2.28}$$

$$V_{i,j} = V_{i,0} V_{0,j} \tag{2.29}$$

where i=1 to $N-1$ and j=1 to N. Note that V_0 is the supply voltage at the array pad and does not include any cable losses from the actual supply to the array.

An important figure of merit when describing the DC bias design is the maximum normalized voltage variation (dV_{max}). The maximum normalized voltage variation describes the amount of DC voltage variation that can be expected from a given bias design. The maximum normalized voltage drop for an array is

$$dV_{max} = \frac{V_{0,0} - V_{N-1,N}}{V_{0,0}} \tag{2.30}$$

Ideally, dV_{max} is zero when all of the MMICs have identical DC bias. In practice, the designer has to determine how much variation is acceptable. In the case of the failed array (Figure 2.18), $dV_{max} = 0.45$ is unacceptably large. A reasonably acceptable DC bias design should have $dV_{max} < 0.10$ to ensure a correspondingly reasonable MMIC gain (S_{21}) variation across the entire array.

2.7 Electromagnetic coupling analysis

At this point in the QO amplifier design, everything but the unit cell size is determined. The fact that only the unit-cell size is undetermined is no coincidence. It is impossible

to complete an electromagnetic (EM) coupling analysis of an array without first knowing the specific array details. For instance, type of substrate, type of antenna, type of array lattice, MMIC gain, etc., must all be known prior to attempting the coupling analysis. This section is dedicated to explaining the choice of unit cell size for the particular QO amplifier design of this chapter with CPW-fed slot antennas on AlN with *Alpha* AA028P3-00 MMICs.

The most difficult design consideration is the effect of mutual coupling between sub-array elements (input antennas, output antennas, and bias lines). The main difficulty is the lack of accurate and simple models (analytical or numerical) of EM coupling between elements within an array. Even something as simple as designing a single second resonance slot antenna requires the tedious CAD design process based on a numerical MOM model (recall Section 2.4.1). It is not difficult then to imagine that the mutual coupling problem is more complicated because of the tens, or even hundreds, of RF elements that exist in an array. In addition to the model size, the distance between RF elements and the type of antennas greatly affect the EM coupling within any array. Therefore, any model of EM coupling is highly dependent on the specific geometry of the particular array of interest.

In general, mutual coupling causes an antenna in an array to have different RF properties (e.g. insertion loss, radiation pattern, efficiency) from the same antenna in isolation. An antenna in the array is affected by all of its surroundings. In principle the EM coupling within the array could be studied with a MOM model of the entire array. The problem is that such a model necessarily requires large computer resources (run time and memory). Michael Steer's group at North Carolina State University has had limited success in modeling entire QO arrays of patch antennas with a custom computer model [25]. Note that the measurements to confirm the custom model are off by as much as 10 dB from simulations. Similar models for CPW-fed slot arrays do not currently exist and the commercial packages, *Momentum* and *IE3D*, can only model a few elements at a time. Another approach besides modeling the entire array is therefore necessary.

In this thesis, the approach of modeling mutual coupling effects follows closely the work presented by Humphrey [26]. Humphrey [26] characterized the coupling between patch antenna pairs by measuring S_{21} as a function of separation distance. The implicit assumption is that EM coupling in an array is dominated by the interaction of a single array element and its nearest neighbors. This assumption is based on three facts for patch antennas: first, S_{21} varies as $\frac{1}{d}$ for E-plane coupling [27]; second, S_{21} varies as $\frac{1}{d^2}$ for H-plane coupling [28]; and finally, less than 1 dB of coupling is due to surface waves [29]. In other words, the effects of nearby elements are dominant since mutual coupling effects, quantified by S_{21}, decrease rapidly as separation distance increases. The assumption reduces the complexity of the mutual coupling problem. Rather than attempting to model an entire array of antennas to determine sub-array coupling, only S_{21} between pairs of elements needs to be characterized. Based on this nearest neighbor approximation, the problem of characterizing the EM coupling effects in the array is reduced to determining S_{21} as a function of separation distance between pairs of sub-array elements in close proximity with each other.

IE3D and *HP Momentum* simulations, rather than measurements, are performed to characterize mutual coupling effects within the QO amplifier array. Measurements are hampered by the bi-directional radiation pattern of the slot antenna and its interaction with the *Cascade* probe station. Figure 2.21 summarizes the results of the coupling analysis. In each case, only the two elements connected by the arrow are included in the model and all other elements are removed to reduce the model size. For instance, in case A, a model with a slot antenna connected to port 1 and a bias line terminated with matched ports (2 and 3) is created and S_{21} is numerically calculated to be -41 dB. Similar models are created and analyzed for the remaining cases. As expected, the coupling between input and output antennas (cases B and C) is dominant due to close proximity of antennas. Another important coupling mechanism occurs between the slot and parallel bias line (case D). Based on a comparison between cases A and D, the DC bias lines are oriented perpendicular to the

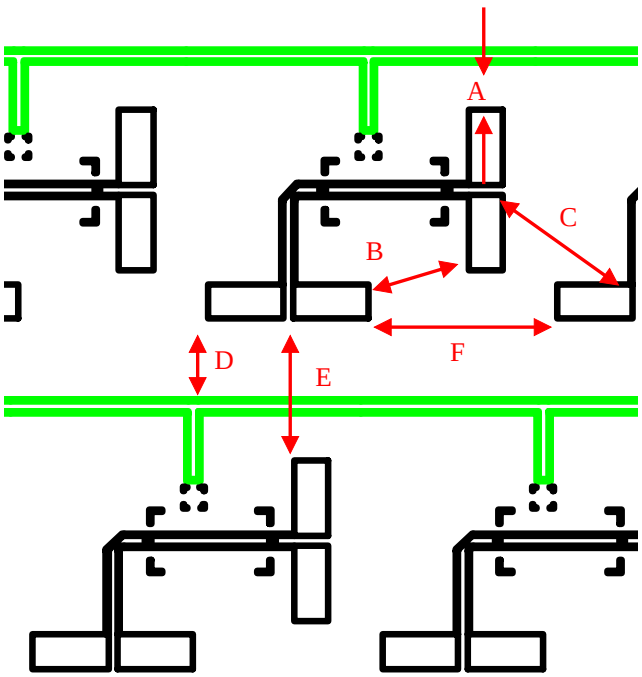

Figure 2.21. Nearest-neighbor coupling (S_{21}) is calculated for 6 important cases: (A) −41 dB; (B) −21 dB; (C) −19 dB; (D) −28 dB; (E) −38 dB; (F) −29 dB. For each case, only the two elements connected by red arrows are modeled and all other elements are not present.

output antennas to minimize coupling from the MMIC to the bias lines.

The choice of unit cell size is determined based on the gain of the MMIC. Coupling (S_{21}) must be low enough as to inhibit possible oscillations. To decrease the chance of MMIC oscillations, a closed loop gain for every RF path must be less than 0 dB. Since the gain of the *Alpha* AA028P3-00 MMIC is 19 dB, it is reasonable to take the cutoff value of $S_{21} = -19$ dB to guarantee that any closed loop gain is at most 0 dB. The design criterion of $S_{21} < -19$ dB is used to determine the actual positions of the elements shown in Figure 2.21. In particular, the final 9 mm ($0.92\lambda_0$) unit-cell design is chosen to keep coupling between the orthogonally-polarized input and output antennas below the maximum MMIC gain (−19 dB) for stability.

2.8 Satisfactory designs

In this chapter, the design of the final Ka-band QO amplifier using slot antennas on AlN with *Alpha* AA028P3-00 MMICs (shown in Figure 2.3) is explained in detail. The final QO amplifier uses a 9 mm ($0.92\lambda_0$) triangular lattice to suppress E-plane side lobe radiation and control internal mutual coupling. The second resonance slot antennas are designed using *Momentum* to have a 50 Ω input impedance with a width of $w_{\text{slot}} = 0.9$ mm and a length of $l_{\text{slot}} = 4.15$ mm. In order to simplify the fabrication, the CPW feed is used to excite the slot antenna. The CPW gap is $S_{\text{CPW}} = 75\,\mu$m and the CPW center conductor width is $w_{\text{CPW}} = 225\,\mu$m.

The next logical step is to fabricate and test this QO amplifier design; three active arrays (0, A, and B) and one passive array suitable for characterization are summarized in Table 2.3. Note that the passive array is required for calibration purposes and is identical to Array B except each MMIC is replaced by a through CPW line. The main variation among the designs is the ratio $R_{\text{MMIC}}/R_{\text{bias}}$ which controls the DC bias variation across the array. By characterizing three active arrays with slight design and fabrication variations, repeatability of performance and biasing effects on the QO amplifier can be studied experimentally in the remainder of this thesis.

Table 2.3. Summary of QO amplifier designs on AlN using *Alpha* AA028P3-00 MMIC amplifiers.

Array Label	**Description**
0	$R_{\text{MMIC}}/R_{\text{bias}} = 1.5$
A	$R_{\text{MMIC}}/R_{\text{bias}} = 3.3$
B	$R_{\text{MMIC}}/R_{\text{bias}} = 2.5$
Passive	Identical to Array B except through CPW lines replace MMICs

CHAPTER 3

FABRICATION AND PERFORMANCE CHARACTERIZATION

Based on the procedure outlined in Chapter 2, some promising Ka-band amplifier array designs were determined and are summarized in Table 2.3. The two main goals of this chapter are to explain the details involved in the fabrication of these Ka-band arrays and to compare their designs in terms of measured performance [30].

3.1 Fabrication

The details involved in the fabrication of the amplifier arrays are summarized in this section. The arrays are built from three basic parts: commercial *Alpha* AA028P3-00 MMIC amplifiers; a completely metalized 254 μm (10 mil) thick AlN substrate; and pre-manufactured capacitors (47 pF and 100 pF). The fabrication of each amplifier array involves: etching of the array features onto the substrate metalization layer; implementation of a jig to provide mechanical support for the fragile AlN substrate and an external DC bias connection; attachment of MMICs and capacitors to the AlN substrate with silver epoxy; and electrical connection of RF components using a wire bonding machine.

3.1.1 Photolithography The first objective in the fabrication process is to reproduce the array layout design (recall Figure 2.3) on the metal layer of the AlN substrate (see Figure 3.1). The minimum array feature size is 75 μm from the CPW line gap. This minimum feature size is too small for milling, but is well within the limit of current photolithography technology [31]. Therefore, photolithography is required for the fabrication.

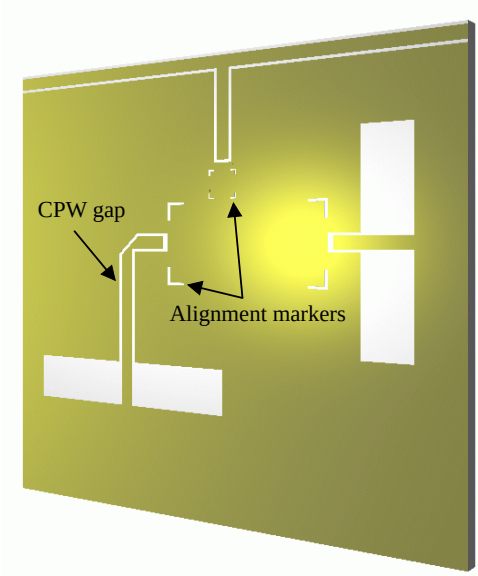

Figure 3.1. The goal of photolithography is to etch the thin metal layer (yellow) of the AlN substrate (grey) to form the input and output slot antennas, CPW lines, and bias lines.

The photolithography process begins by spinning positive *AZ4210* photoresist (PR) onto the completely metalized AlN substrate at 5000 RPM for 30 seconds which is subsequently baked for 20 minutes at 90° C. A dark-field mask (see Figure 3.2) is required to transfer the desired image onto the substrate. The mask is printed on a transparent Mylar sheet by *Image Technology, Inc.* The substrate is placed in an alignment jig where the mask is aligned on top and held in place with a UV-transparent glass plate. The substrate-mask-glass assembly is bolted together for mechanical support. The complete stack is exposed to UV light for 110 seconds. Note that since there is only one mask step by design, this step is well suited for mass production. The substrate is removed, developed in 2:1 *Hoechst AZ400K* for 65 seconds, and then baked for 20 minutes at 120° C. The resulting substrate has a layer of PR everywhere except where UV light passed through the mask. The substrate is placed in a solution of *Transene* gold etchant Type TFA for 2 to 5 minutes (depending on Au thickness) until the design features are completely etched into the metal layer. Finally, the positive PR is removed with an acetone rinse and the desired (Figure 3.1) result is achieved.

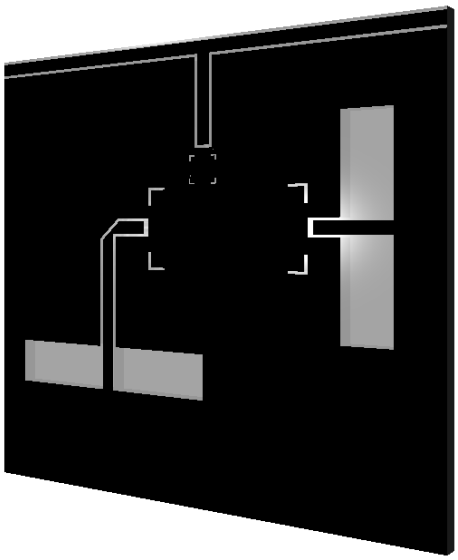

Figure 3.2. Drawing of the dark-field mylar mask (corresponding with Figure 3.1) printed on a thin transparent Mylar sheet.

The final dimensions of the critical array elements are measured: CPW gap distance is 87 μm (expected 75 μm); CPW center conductor width is 220 μm (expected 225 μm); slot antenna length is 4.17 mm (expected 4.15 mm); and slot antenna width is 0.92 mm (expected 0.9 mm). The consequences of this overetch will be discussed later in Section 3.2.2.

3.1.2 Mechanical jig The AlN substrate is fragile. For example, Array 0 was completely fabricated (MMICs and all) and was being characterized when it was accidentally tapped with a screwdriver and cracked. Obviously, some means of mechanical support is necessary to help secure the amplifier array. One such means of support is shown in Figure 3.3. The support is provided by sandwiching the AlN substrate between two sturdy-rigid materials. Figure 3.3, shows the jig resting on a 6.6 mm (260 mil) thick brass plate; the thick brass plate is not part of the jig, but rather a part of the hot stage which is used in subsequent fabrication steps to heat the array. Notice that an external bias connection is also provided by means of snap connectors in the lower left corner on the jig.

The jig has two different configurations determined by the support back plate. During the fabrication stages, the fabrication support plate [see Figure 3.4(a)] is used to regulate

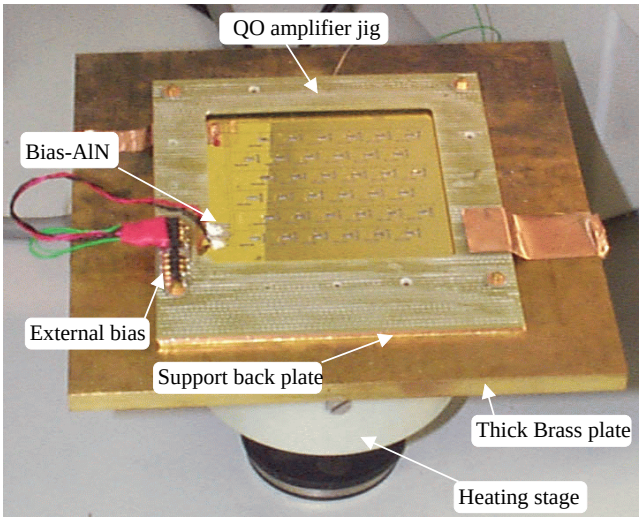

Figure 3.3. QO amplifier jig which helps to protect the AlN substrate during fabrication and characterization. In the picture, the AlN substrate is placed inside the protective jig which is resting on a thick Brass plate.

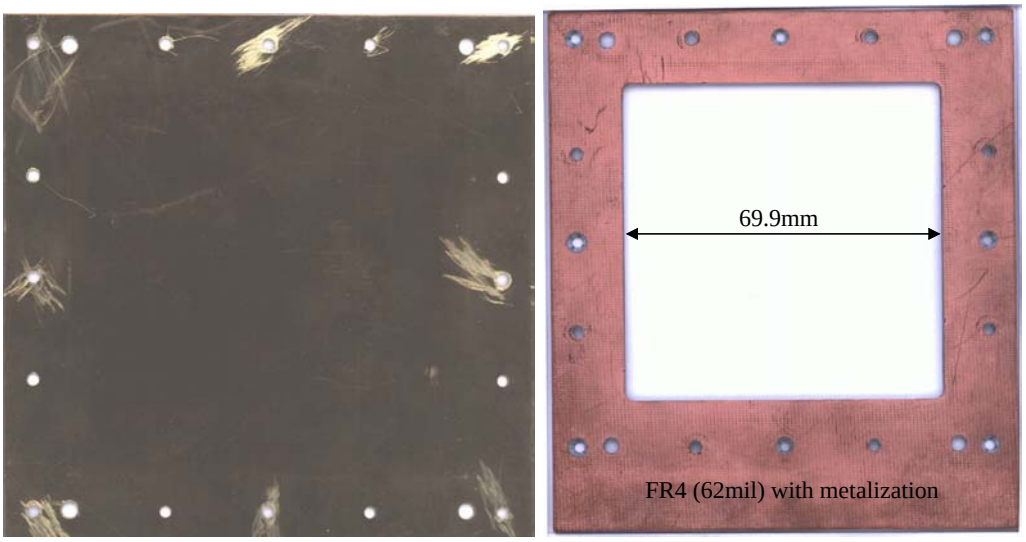

(a) Fabrication support plate (b) Characterization support plate

Figure 3.4. The two different support plates used in the QO amplifier jig are pictured: the fabrication support plate (a) is made from 635 μm (25 mil) brass; and the characterization support plate (b) is made from 1.57 mm (62 mil) FR4.

the AlN temperature (see Section 3.1.3) and provide mechanical support (see Section 3.1.4). After fabrication is complete, the fabrication support plate is replaced with the characterization support plate [see Figure 3.4(b)] which has a 69.9 mm window to allow RF propagation into and out of the QO amplifier.

3.1.3 Mounting of MMICs and capacitors With the AlN substrate supported by the amplifier jig utilizing the fabrication support plate [Figure 3.4(a)], the MMICs and capacitors are attached to the array (see Figure 3.5) with silver epoxy. While looking

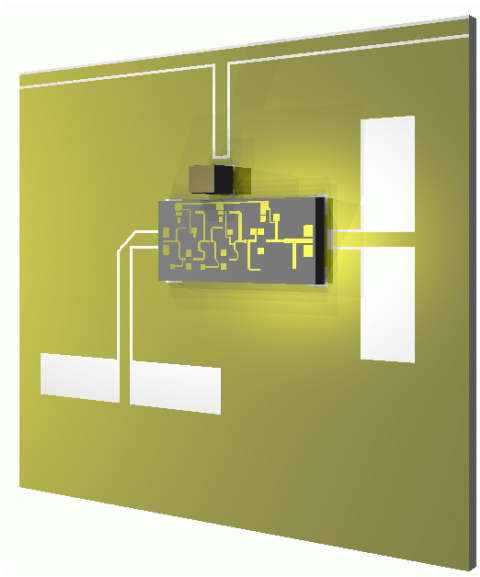

Figure 3.5. Schematic view of a unit cell of an active array after the MMICs and capacitors are mounted using silver epoxy.

into a microscope, silver epoxy is painted onto the substrate, inside each MMIC and capacitor alignment marker, with a needle point by hand. Each individual MMIC and capacitor is positioned onto the painted silver epoxy with tweezers, again using the alignment markers as guides. To cure the silver epoxy, the heating stage (shown in Figure 3.3) is then used to heat the AlN substrate resting on the thick brass plate at 100° C for 2 hours.

3.1.4 Wire bonding The final stage of fabrication is accomplished with a wire bonding machine. The array remains on the heating stage and is positioned in the

wire bonder as shown in Figure 3.6. The wire bonder is used to make all RF electrical

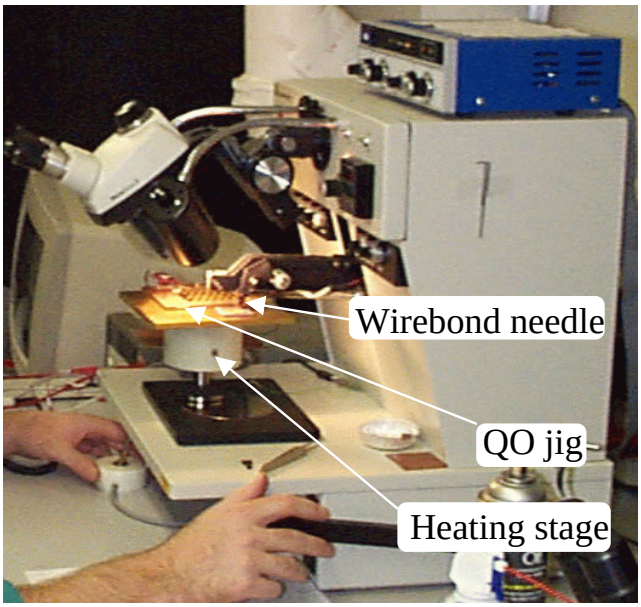

Figure 3.6: The wire bonder is pictured with the QO amplifier in place.

connections as shown in Figure 3.7. The bond wires provide connections between the MMIC pads, capacitor pads, and array metalization, as well as airbridges along the CPW lines to prevent slot modes. Note the the diameter of each wire bond is 25.4 μm (1 mil).

In total, four arrays (passive, 0, A, and B) are fabricated as described in the previous sections with some slight design variations (recall Table 2.3 design summary). Two of the fabricated arrays (A and B) are pictured in Figure 3.8. The supplementary bias line network consisting of insulating adhesive mylar and copper tape used by Array A is visible in the expanded view of Figure 3.8(a). The bias design of Array B differs; additional gold is electroplated onto the DC bias line over which additional airbridges and capacitors are added [see expanded view in Figure 3.8(b)]. For calibration purposes (recall Section 1.2.4), a passive array is fabricated to be identical to Array B, except that CPW through lines replace the MMICs. The arrays A and B differ only in the implementation of the biasing network and substrate metalization such that studies can be performed to experimentally determine the repeatability and sensitivity of the QO amplifier designs.

Figure 3.7. Schematic view which is the result of the final wire bonding stage of fabrication.

3.2 Experimental results

Results from experiments designed to characterize the performance of the QO amplifiers are summarized in this section. In particular, the following measurements are summarized here: thermal distribution across the array; return loss of slot antenna; small signal gain of the MMIC; small signal gain of the array; saturated output power of the array; far-field radiation patterns; and measurement of bias variations.

3.2.1 Thermal measurements The maximum operation temperature of QO amplifiers is critical to overall array reliability and performance. If the operation temperature is too high, the MMICs or the substrate may be destroyed. In addition, the gain and output power of a GaAs MMIC in saturation decrease as its temperature increases. A measurement of array temperature under normal operating conditions is necessary to determine if a QO amplifier is likely to fail or have degraded performance due to a high operating temperature.

With the array mounted vertically and under normal DC bias conditions, a small ($0.65\,\mathrm{mm}^2$) thermal sensor is carefully placed in physical contact with the surface of the array and the temperature is measured. The temperature is determined mainly by the

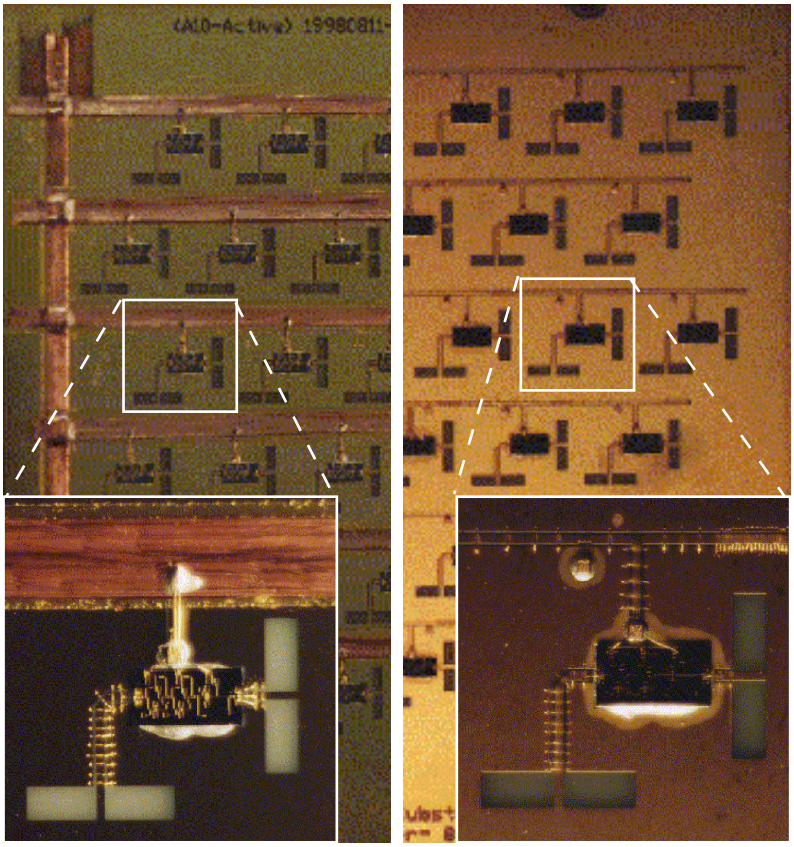

Array A Array B

Figure 3.8. Photographs of Arrays A and B with corresponding unit cells enlarged. The size of the unit cell is 9 mm by 9 mm (0.9λ by 0.9λ at 30 GHz).

DC bias and not the type of RF excitation. Small-signal excitation is most convenient and therefore, is used for this measurement. The point of contact is not on an actual MMIC since such contact would destroy that MMIC. The thermistor is connected near the center of the substrate as close as possible to the center MMIC where the array temperature is expected to be maximum (see Section 2.3). The maximum steady-state temperatures are measured to be 69° C and 62° C for Arrays A and B, respectively. The measured temperatures are lower than expected due to natural heat convection which is not included in the simple theoretical model.

The temperature is further improved by employing forced-convective cooling. Two fans with a flow of 1 m^3/minute are added to the previous setup and the operation temperature measurements are repeated. The maximum steady-state temperatures for Arrays A and B decrease to 39° C and 38° C, respectively. The manufacturer recommends an operation temperature of 25° C but allows a range from −50° C to 90° C. Based on the measurements with the cooling fans, the QO amplifiers are capable of handling the heat generated by 36 MMICs without significantly affecting array reliability and performance.

3.2.2 Elements of the arrays To estimate the accuracy of the numerical design simulations, various individual array components are fabricated on a separate AlN substrate for characterization. A *Cascade* probe station and (GSG) CPW probes are used to measure individual circuits, using a TRL calibration set also fabricated on the AlN substrate. The components of particular interest are: the CPW line and 90° compensated bend; the *Alpha* MMIC; and the slot antenna.

To test the quality of the CPW transmission line, an isolated CPW line is fabricated on the characterization substrate. Port 1 of the *Cascade* probe station is connected to one open end of the CPW line with a CPW probe; port 2 is connected to the other open end. An HP8510C vector network analyzer is used to measure S_{11} and S_{21} of the CPW line. The measurements of S_{11} and S_{21} confirm that the CPW line (with and without the 90°

compensated bend) performs as expected with loss no greater than 0.4 dB (within calibration error). The lack of loss confirms that the AlN substrate has a low dielectric loss tangent at Ka-band and validates the design assumptions used in Sections 2.4.1 and 2.4.2.

The measurement of MMIC gain is similar to the CPW measurement except a MMIC is placed on the CPW line in between ports 1 and 2 of the probe station and the MMIC is biased through an external bias line connection. The measured gain of one of the *Alpha* AA028P3-00 MMICs is summarized in Figure 3.9. It is important to note the

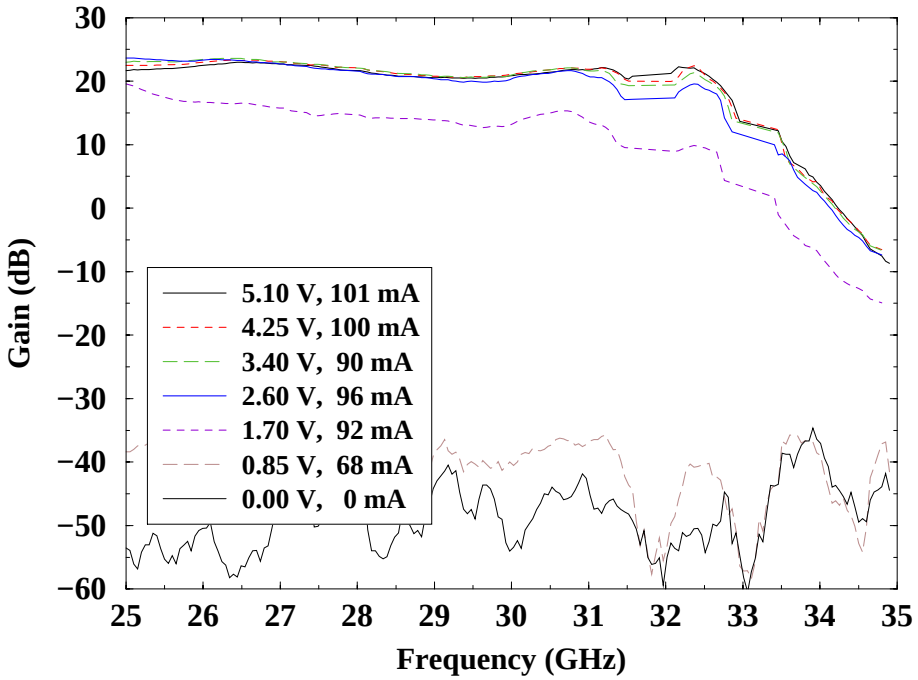

Figure 3.9: Measured gain (S_{21}) of the *Alpha* AA028P3-00 MMIC at various bias points.

MMIC under test is connected to the DC bias line, input CPW line, and output CPW line with bond wires which are configured identically to the connections made in Arrays A and B. The measured gain of the MMIC therefore includes effects due to the microstrip to CPW transition (MMIC to substrate transition) as well as the gain of the MMIC. Based on the measured gain, the MMIC performs as expected with the microstrip-to-CPW transition made during fabrication.

The slot antenna is also characterized using the probe station. The measured resonance of the slot antenna is 32.6 GHz and is shifted 150 MHz (0.5%) from the simulated [1] value of 32.75 GHz (Figure 3.10). The expected return loss at resonance is 35 dB. The slot

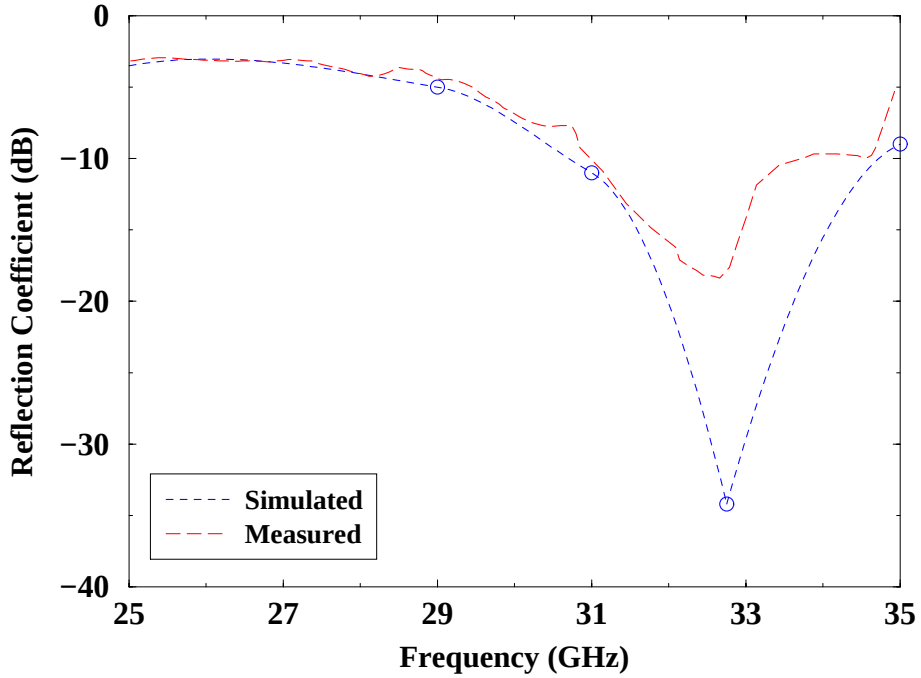

Figure 3.10. Simulated and measured reflection coefficient $|S_{11}|$ of the slot antenna. *HP Momentum* is used for the simulation.

antenna has a measured and simulated 2:1 VSWR bandwidth of 3.7 GHz (11%) and 4.3 GHz (13%), respectively.

3.2.3 Small signal array measurements The RF performance characterization of the arrays is achieved with three measurements: a small-signal far-field gain measurement with standard horns; a small-signal near-field gain measurement with hard horns; and a large-signal far-field power measurement with standard horns. In all three cases, the experimental setup is essentially the same as described in Chapter 2 (see 2.2). One practical difference exists; an external amplifier is required to saturate the array in large-signal

[1] This antenna simulation includes an increase in antenna and CPW dimensions resulting from over etching in the fabrication process. This is more representative than the original antenna design which (see Figure 2.12) does not include over etching effects on the physical dimensions of the slot antenna and CPW line.

far-field excitation as shown in Figure 3.11.

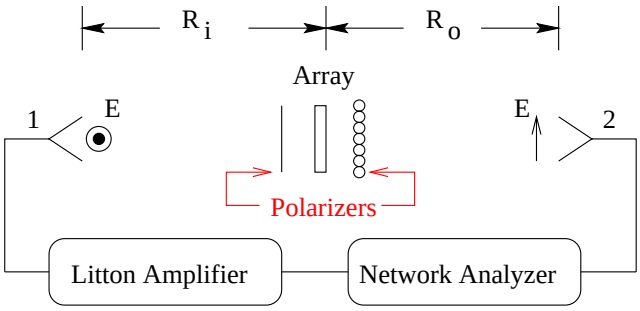

Figure 3.11: Schematic diagram of the QO configuration used in experiments.

Table 3.1. Measured small-signal response with standard horns **(a)** and hard horns **(b)**. BW indicates the range over which the arrays have gain. G_a is defined with respect to a passive array.

(a) Standard-horn small-signal gain measurements.

Array	freq (GHz)	Gain (dB)	BW (GHz)	On/Off Ratio (dB)	G_a (dB)
A	31.02	2.1	0.34	34	10
B	31.40	6.5	0.50	38	14

(b) Hard-horn small-signal gain measurements.

Array	freq (GHz)	Gain (dB)	BW (GHz)	On/Off Ratio (dB)	G_a (dB)
A	30.32	2.0	0.22	25	10
B	31.30	4.7	0.70	35	12

For the small-signal far-field measurement, two 21.5-dB cross-polarized standard horn antennas are placed $60\lambda_0$ from either side of the array ($R_i = R_o = 60\lambda_0$). Measurements are performed with an HP8510C vector network analyzer calibrated to a free-space through. In theory, tuned polarizers should increase the gain of the array by 6 dB by enforcing unidirectional radiation of the slot antennas. Measurements place the actual increase in gain by the polarizers at 3 dB; each polarizer contributes approximately 1.5 dB of loss. Note that each polarizer is manufactured from inexpensive computer ribbon cable. Figure 3.12(a) shows the measured gain of the passive and active arrays with respect to a through calibration. Measurements are summarized in Table 3.1(a). The average gain G_a contributed by

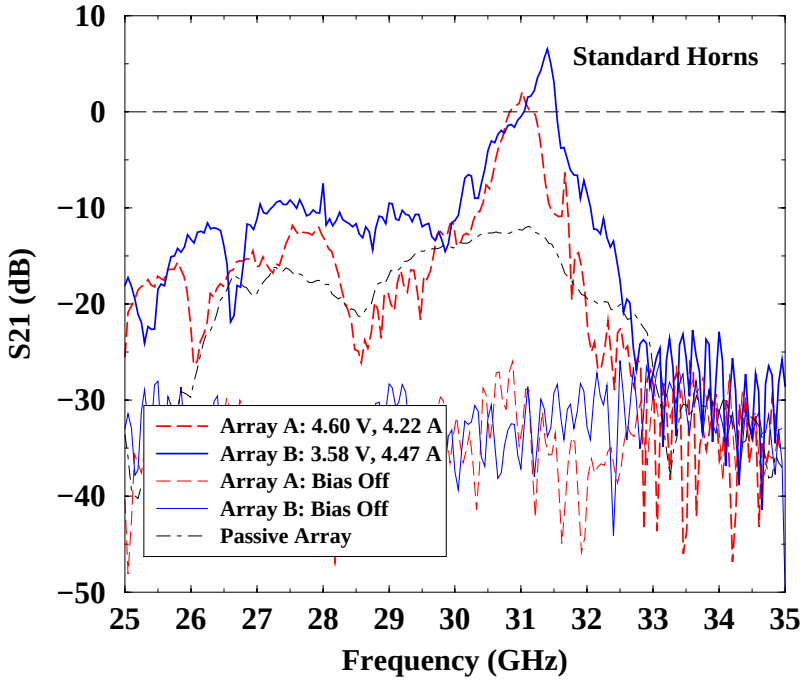

(a)

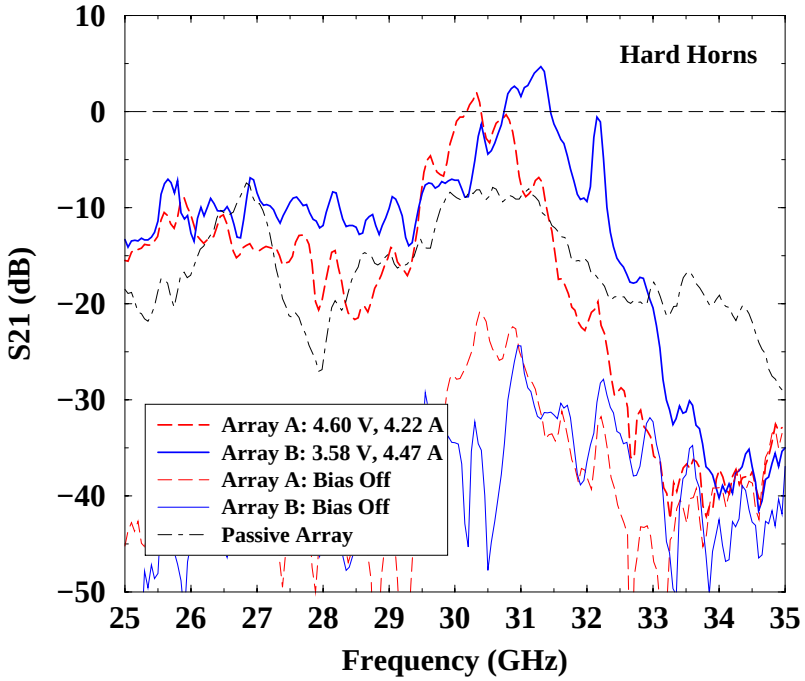

(b)

Figure 3.12. Small-signal gain measurements with standard horns **(a)** and hard horns **(b)**. Measurements are with respect to a through calibration.

the MMIC amplifiers is 10 dB.

Near-field small-signal gain measurements are performed in a similar fashion using two cross-polarized hard-horn antennas $6\lambda_0$ from the array ($R_i = R_o = 6\lambda_0$). The hard-horn antennas provide a uniform field distribution with amplitude and phase variations of only ± 1 dB and 80° over 98% of the horn aperture[15]. The small-signal hard-horn gain measurements are shown in Figure 3.12(b) and summarized in Table 3.1(b). The average gain G_a contributed by the MMIC amplifiers is again 10 dB.

3.2.4 Large signal array measurement Far-field large-signal power measurements are performed with standard horns placed $25\lambda_0$ from the array. In place of the network analyzer, an HP83640A synthesized sweeper driving a *Litton* M-762-00 MMPM are used to provide the power required to saturate the arrays. The estimated power incident on the array is 27.7 dBm. An HP437B power meter with a high frequency power sensor (HP8487A) is used to measure the output power. The losses of the cables and connectors as well as the gains of the horns and feed amplifier are calibrated by measurement. The effective isotropic radiated powers (EIRP) and output powers estimated from measured radiation patterns are summarized in Table 3.2. Measurement accuracies are ± 1 dB. The gain

Table 3.2: Measured saturated response with standard horns.

Array	freq (GHz)	EIRP (dBm)	EIRP (W)	P_t (dBm)	P_t (mW)
A	30.40	49.5	89	25	316
B	31.15	51.6	145	27.1	513

saturation of Arrays A and B is 7.9 dB and 7.5 dB respectively.

The maximum saturated output power of the arrays is calculated by dividing the measured EIRP by the estimated directivity of the array [32]. A value of 24.5 dB for the array directivity is obtained by both the Krauss approximation and the physical area of the array. The value obtained by Krauss approximation is based upon the large-signal far-field patterns shown in Figure 3.14. The radiated power includes the loss of the polarizers which

are an integral part of the QO arrays. By improving polarizer loss, the power could increase by as much as 1.5 dB (or 0.5 W and 0.7 W, respectively).

3.2.5 Far-field patterns Pattern measurements are performed using far-field standard-gain horn antennas $60\lambda_0$ from the array. Measurements are performed with polarizers under large-signal excitation. The theoretical and measured E- and H-plane patterns for the passive and active arrays are shown in Figure 3.13 and Figure 3.14 respectively. Theoretical array patterns are generated by multiplying the array factor of a uniform array by the pattern of the slot antenna (Section 2.5). The main beam is predicted well for both arrays in the E-plane. It is believed that the difference in side lobes between theoretical and measured active array patterns is due to a variation of magnitude and phase at the output of the MMICs, attributed to different MMIC bias points.

3.2.6 Bias variations across the array Voltage variations are measured across the bias network without RF input. Figure 3.15 shows the normalized measured voltage deviation along the bias network at each MMIC due to the bias ladder network. Voltage variations for Array B match the expected values within 5% relative error based on Eqs.(2.19) and (2.21) with a maximum normalized voltage variation of 88%. Array A's vertical voltage uniformity differs from theory due to resistive bus-bar connections. The resistive bus-bar connections occur at the intersection between vertical and horizontal bias lines where silver epoxy is required for electrical connection (see Figure 3.8(a)). The silver epoxy thickness is difficult to control which leads to variations in the resistivity of the bus-bar connections.

3.3 Summary

This chapter presents a Ka-band quasi-optical power-combining array with 145 W EIRP or 0.5 W of output power at 31 GHz. The active array consists of 36 unit cells with

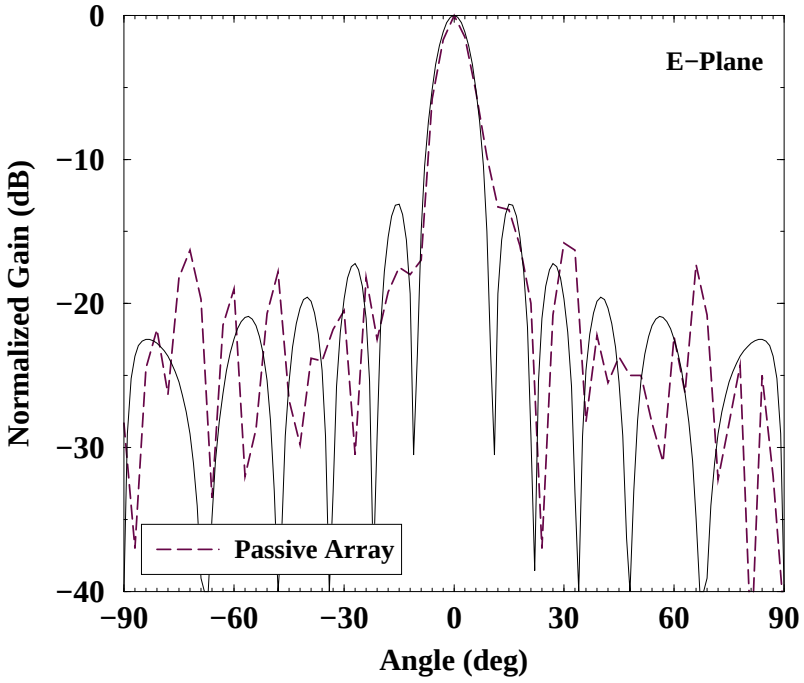

(a)

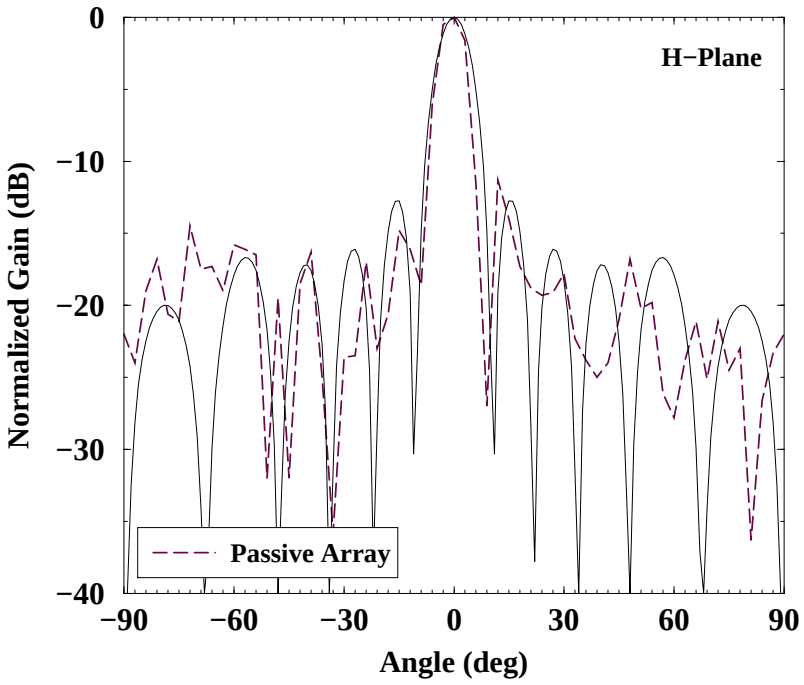

(b)

Figure 3.13. Passive array E-plane pattern measurement **(a)** and passive array H-plane pattern measurement **(b)** are shown as dashed lines. The measurement frequency is 31.4 GHz. The theoretical plot (shown as solid line) assumes a uniform array.

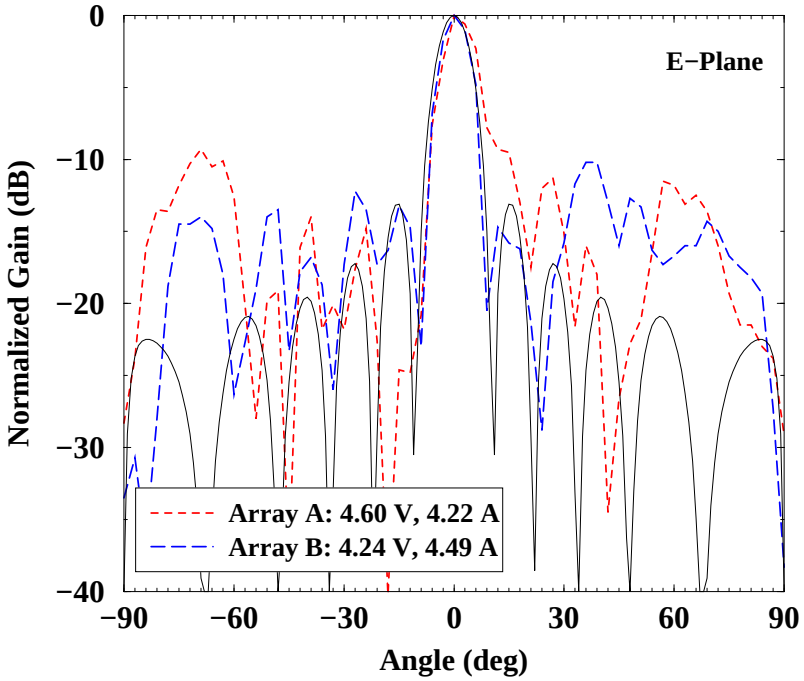

(a)

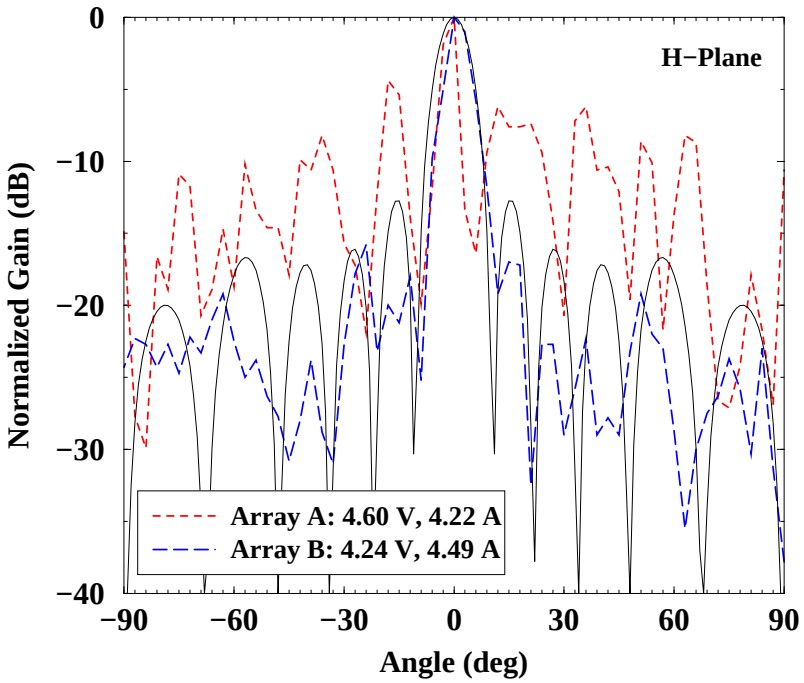

(b)

Figure 3.14. Active array E-plane pattern measurement **(a)** and active array H-plane pattern measurement **(b)** are shown as dashed lines. The measurement frequency is 31.4 GHz. The theoretical plot (solid line) assumes a uniform array.

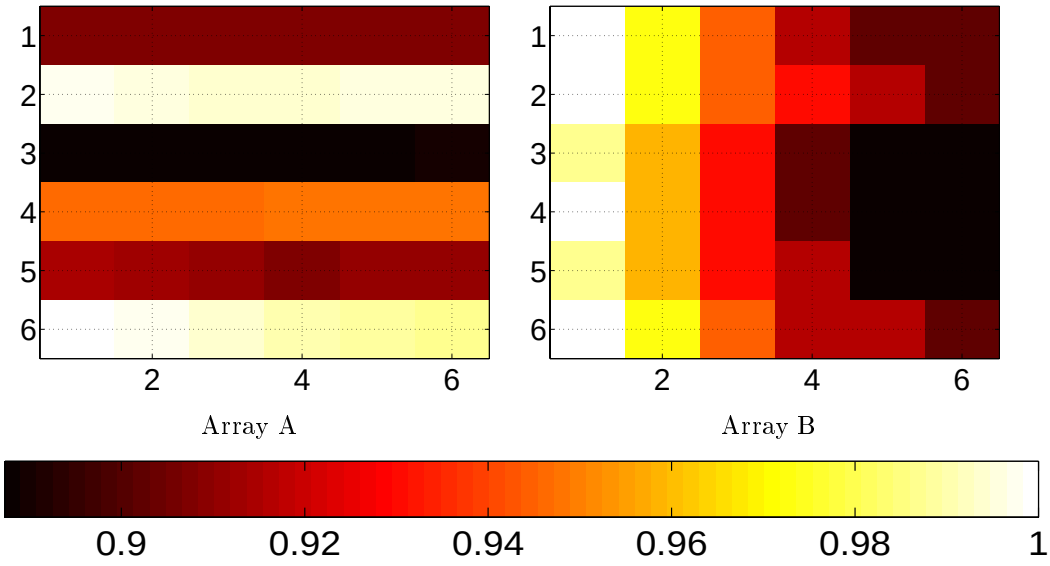

Figure 3.15. Measured normalized voltage levels for Arrays A and B. The lowest normalized voltage level (black) corresponds to 89% of the applied voltage.

commercial low-power MMIC driver amplifiers. Repeatability of array performance was examined with respect to bias-network variations on two arrays with identical RF architectures but different biasing networks. The variation of bias across the arrays causes magnitude and phase variations at the output antennas. It is believed that these variations contribute to creating different peak powers (316 mW and 513 mW), gains (2.1 dB and 6.5 dB), and far-field patterns of the two amplifier arrays which have identical RF designs.

Overall, the performance of both QO amplifiers is worse than expected: the average gain contributed by the MMICs in the stable array is 10 dB less than the gain of an individual MMIC; and the maximum output power is 0.5 W which is lower than the expected 2 W, and oscillations (indicative of mutual coupling) occurred at low bias levels. The array gain is lower due to instabilities that prevented full DC bias levels from being reached. The measurements in this chapter confirm that the individual antennas, CPW lines, and MMICs behaved as designed. The measured DC bias variations agree with theory within 5% relative error. Despite the fact that individual array components and the DC bias network perform well,

the paramount question – why the QO amplifiers performance is less than expected – is not answered in this chapter, and will be addressed in Chapters 4 and 5.

The experiments presented in this chapter are capable of characterizing how well the QO amplifiers perform, but are incapable of determining the design faults or fabrication issues which directly cause degraded array performance. Perhaps, performance is influenced by variations in slot antenna and CPW dimensions between the arrays due to variations in metalization and processing. Or perhaps, the nearest-neighbor approximation of mutual coupling used in the design is a poor model of internal array coupling. In essence, based on far-field measurements, only educated guesses can be made about the internal array problems that cause poor performance. More information (see Chapter 4) is needed to determine what went wrong and to improve future QO amplifier designs.

CHAPTER 4

NEAR-FIELD ELECTRO-OPTICAL DIAGNOSIS

In Chapter 3, far-field measurements used to characterize the performance of QO amplifiers are described. When the QO amplifiers did not perform as expected, the limitations of far-field measurements became obvious – the far-field of an array is the result of superposition of all array elements which tends to mask the effects of sub-array variations (up to complete device failure) on overall array performance. This "graceful degradation", as it is commonly referred to in the QO community, is usually beneficial since it makes arrays tolerant to sub-array failures [33]. However, the benefit of graceful degradation causes the problems and difficulties associated with diagnosing array failures based on far-field measurements.

Figure 4.1 illustrates the type of near-field measurement made possible by an electro-optic (EO) probe station.[1] The 2D color map graphically represents the measured electric field magnitude of a unit cell within a Ka-band QO amplifier as a function of position. Two maxima, symmetrically located about the CPW feed, are clearly visible. The theoretical calculation of field intensity shown in Figure 2.11 shows two similarly located maxima. Note that Figure 2.11 plots field intensity on a variable size mesh (smallest mesh near slot edges); consequently, the field intensity magnitude is largest near the slot edges. The expected second resonance of the slot antenna is confirmed by this EO measurement.

The EO probe station is not limited to measuring the magnitude of the electric

[1] The EO probe station is the result of work done by Dr. John Whitaker, Kyoung Yang, and Dr. Gerhard David. The EO probe station is located in their lab at the Center for Ultrafast Optical Science, University of Michigan, Ann Arbor.

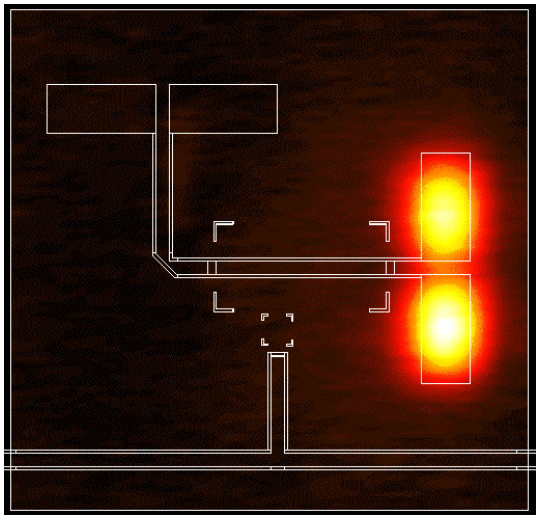

Figure 4.1. Measured near-field demonstrates the value of electro-optic (EO) probe station. The x-component of the electric field is normalized and ranges from -20 dB (black) to 0 dB (white). An outline of the unit cell is superimposed on the color map. The size of the slot antenna is 4.15 mm by 0.9 mm. The spatial resolution of this particular measurement is 93 μm.

fields alone. In fact, both the amplitude and phase information are measured simultaneously. Figure 4.2(a) plots the phase information which corresponds to the previous Figure 4.1. The top and bottom sides (green region on right side) of the slot antenna are in phase. Hence, the desired radiating mode of the slot antenna is confirmed. In contrast, Figure 4.2(b) shows the phase information for a unit cell of a different array. In case (b), the slot antenna is positioned on the far left side. The bottom half of the slot (green patch) is 180° out of phase with the top half of the slot (blue-purple patch). The non-radiating mode of the slot antenna has this characteristic 180° phase variation. The most likely cause of the non-radiating slot mode is the airbridge nearest the slot antenna. In some instances, the wire bond fails and one end of the airbridge slightly lifts from the substrate such that under the microscope it appears to be in contact.

Figures 4.1 and 4.2 clearly demonstrate the capability of the EO probes station to observe, by measurement with high spatial resolution at Ka-band, the near-field of an array, and thereby diagnose sub-array problems that far-field measurements cannot find.

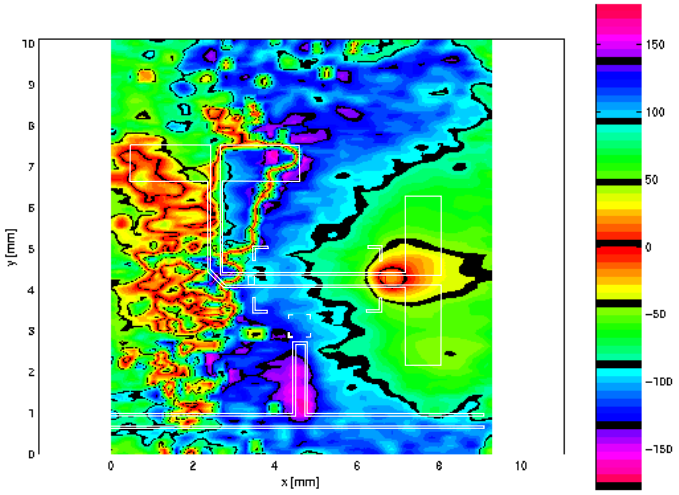

(a) Radiation mode of slot

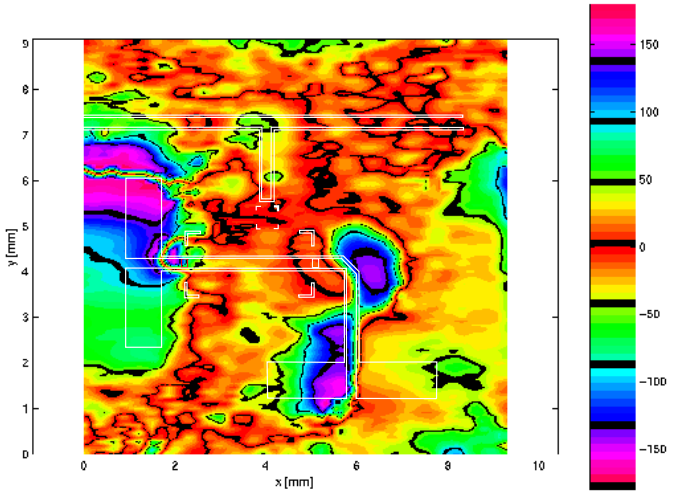

(b) Non-radiating mode of slot

Figure 4.2. Examples of phase plots [°] that demonstrate the diagnostic capabilities of EO probe station. The regions that are completely surrounded by a black band are approximately in phase.

For instance, a near-field measurement could in principle show which unit cell has a non-functioning MMIC by observing the near-field of all output antennas and noting which one does not behave like the functioning unit cell shown in Figure 4.1(a). Unlike the far-field measurements, the near-field measurements have enough spatial resolution (8 μm or $\lambda_0/1250$ at 30 GHz) to correlate the electric fields to their source. Near-field measurements are not susceptible to graceful array degradation effects and therefore, are ideally suited to diagnosing sub-array problems that cause poor array performance.

The goal of this chapter is to understand, based on near-field EO measurements, why the QO arrays designed in Chapter 2 and characterized in Chapter 3 gave less power than expected. The chapter begins with a description of the EO probe station. Subsequently, the results of seven diagnostic near-field experiments, described in Table 4.1, are presented.[2] The first experiment in Section 4.2.1 shows how well the hard horn (HH) feed achieves the desired uniform aperture excitation when the QO array is not present. Once the hard horn is characterized, the near-field of an entire passive array is mapped (Section 4.2.2) to gain insight into the importance of proper feed design. The isolation between input and output antennas which is critical to array stability is characterized in Section 4.2.3. The effects of bias design on the uniformity of the active array are observed in Section 4.2.4. Sections 4.2.5 and 4.2.6 summarize the interactions between the feed horn and the array. The final measurement of mutual coupling effects is summarized in Section 4.2.7. Also, the link between the near- and far-field is discussed in Section 4.2.8. Based on all the diagnostic results, possible design modifications which could improve future QO amplifier designs are summarized in Section 4.3.

[2]The arrays labeled A and B are the arrays characterized in Chapter 3. Abbreviations are listed: "WG" is a small waveguide aperture used to excite a single unit cell, "small HH" is the hard horn utilized in Chapter 3, and "large HH" is a larger-tapered hard horn.

Table 4.1: A summary of EO measurements used to diagnose array faults. The first two columns indicate the experiment number and the section in which they are discussed.

Exp.	Sec.	Array	Probe Orien.	Feed Type	Feed Orien.	Scan Area	Comments
1	4.2.1	none	y	standard horn	y	Aperture	-
		none	y	small HH	y	Aperture	-
		none	y	large HH	y	Aperture	-
2	4.2.2	Passive	x	standard horn	y	Unit cell 33	low RF input
3	4.2.3	A	y	large HH	y	Full array	4.23 V 4.19 A
		B	y	large HH	y	Full array	3.57 V 4.50 A
		B	y	large HH	y	Unit cell 34	3.68 V 4.50 A
4	4.2.4	B	x	large HH	y	Full array	3.42 V 4.46 A
		B	x	large HH	y	Full array	3.60 V 4.50 A
5	4.2.5	A	x	large HH	y	Full array	4.17 V 4.19 A
		B	x	large HH	y	Full array	3.79 V 4.52 A
6	4.2.6	A	x	small HH	y	Full array	4.27 V 4.20 A
		B	x	small HH	y	Full array	3.56 V 4.51 A
		B	x	small HH	y	Unit cell 34	3.56 V 4.51 A
7	4.2.7	A	x	WG	y	Full array	4,23 V 4.20 A
		A	x	WG	y	Full array	4.42 V 4.20 A
		B	x	WG	y	Full array	3.56 V 4.51 A
		B	x	WG	y	Full array	3.57 V 4.51 A

4.1 Overview of electro-optic (EO) probe station

The experimental measurement system used for the near-field characterization of quasi-optical amplifier arrays is sketched in Figure 4.3. This type of electro-optic sampling system has been introduced previously [34, 35, 36], but is summarized here for completeness. The optical beam from a phase-stabilized Ti:Sapphire laser, which has 100-fs duration pulse output at an 80-MHz pulse repetition rate, is focused inside of the electro-optic probe crystal [37, 38]. The faces of the probe crystal are polished in order to achieve total internal reflection of the incident beam, which is detected by a photodiode. The reflected beam is analyzed to determine the change of its polarization state, which is sensitive to the magnitude and phase of the RF electric field that extends into the probe crystal (Pockels effect).

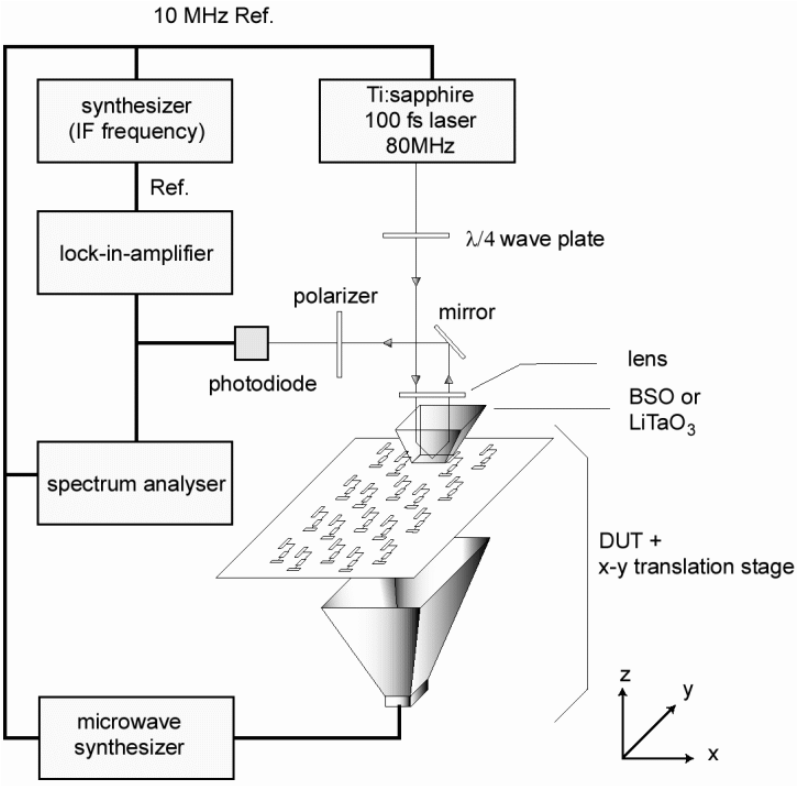

Figure 4.3: Schematic diagram of EO probe station.

In practice, the laser pulse train passes through a polarizer so that the electrical signal from the photodiode is proportional to the modulated optical intensity. Harmonic mixing of the input microwave signal frequency and an integer harmonic of the 80 MHz repetition rate of the laser (the LO) takes place in the electro-optic crystal and is used to obtain an IF that is fed into an RF lock-in amplifier [39, 40]. Using phase-locked-loop electronics in the stabilized laser system, one is able to synchronize the CW signal from a microwave synthesizer to the laser pulse train, with the small offset frequency (i.e., the IF) providing the time delay for the sampling gate. Measurements in amplitude and phase are then performed simultaneously as the computer reads the output of the two channels of the lock-in amplifier, which uses the output of a low-frequency synthesizer, also synchronized to the laser electronics, to maintain a phase reference.

Two types of electro-optic probes are fabricated from Bismuth Silicate (BSO) and

Lithium Tantalate ($LiTaO_3$). These crystals allow the determination of three orthogonal electric field components above the antenna under test (BSO for the normal field and $LiTaO_3$ for the two tangential fields). The crystals have a tip area of $40\,\mu$m $\times$ $40\,\mu$m for the BSO and $20\,\mu$m $\times$ $10\,\mu$m for the $LiTaO_3$.

The device under test (DUT) is mounted on a computer-controlled x-y translation stage, and a typical scan over an array of several square inches takes between 30 to 60 minutes, depending on the exact size and desired resolution. The spatial resolution of the field-mapping technique has been demonstrated to be $8\,\mu$m, although it is not necessary to scan fields with this level of detail for the measurements described herein. In addition to the two-dimensional movement of the DUT, the optical components allow the probe to have freedom of movement in the vertical direction, in order to achieve a three-dimensional field-mapping capability. The minimum detectable voltage is measured to be about 0.5 mV, or -45 dBm, and the sensitivity is 40 mV$/\sqrt{\text{Hz}}$.

In terms of the effect that the electro-optic probes have on the field at the probing location (i.e., in terms of the invasiveness of the probe), it is expected that the dielectric crystals will disturb the field pattern much less than a standard metal waveguide or dipole probe. Nonetheless, the BSO and $LiTaO_3$ probes do have high values of relative permittivity, in excess of 40 for both crystals, and thus can be expected to have some influence on local fields [41]. However, it is also true that in numerous instances, for both guided [34, 42] and radiated fields [43], electro-optic measurements have been demonstrated to be in excellent agreement with known or expected field behavior and with computational results.

4.2 EO diagnostic measurement results for QO amplifiers

Figure 4.4 shows actual pictures of the EO probe station without (a) and with (b) an array present. In all measurements, the input side of the array faces down, towards the RF feed; consequently, the EO probe station measures only the output-side near-electric field

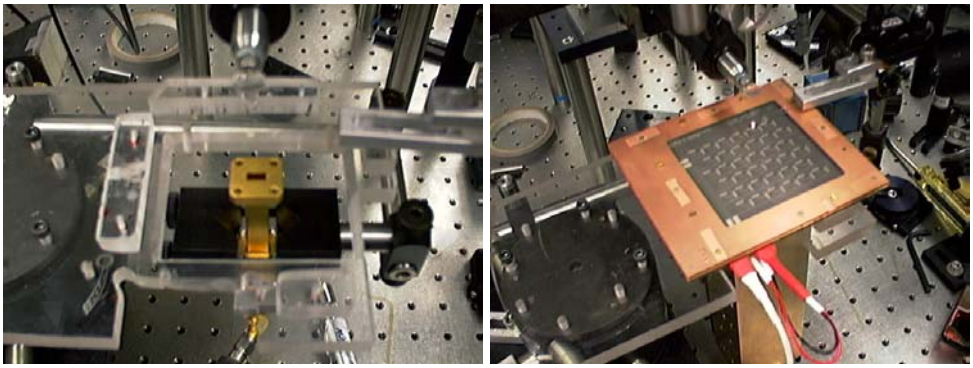

(a) Typical setup with WG excitation

(b) Typical setup with small hard-horn excitation

Figure 4.4. Configuration of EO probe station used for the diagnosis of array faults. (a) shows the EO probe station without an array (the WG feed for the array is visible). (b) shows the EO probe station with Array B in place.

of the array. The output side of the array lacks metalization and is visible in Figure 4.4(b). The EO probe crystal is positioned approximately 130 μm from the array output surface (see Figure 4.5 for scale). The RF feed horn is positioned beneath the array and is connected to an *HP* synthesized sweeper with a coaxial cable. This sweeper does not work above 20 GHz so a passive frequency doubler is required to increase the frequency to Ka-band. Due to cable losses and the frequency doubler, the maximum available power at the input of the RF feed horn is -2 dBm. Recall that the RF operation frequency of the EO probe station (f_0) must be an integer multiple of the laser pulse repetition rate ($f_r = 80$ MHz) and the IF offset ($IF = 3$ MHz). The sweeper frequency (f_s) is determined from f_0 as follows

$$f_s = Z\left[\frac{f_0}{2f_r}\right] f_r + \frac{IF}{2} \tag{4.1}$$

where $Z(x)$ returns the nearest integer value to x. Since each array operates optimally at slightly different frequencies (f_0) which are determined from the small-signal measurements summarized in Table 3.1, Array A and B are excited with sweeper frequencies (f_s) of 15.521 GHz and 15.6815 GHz, respectively.

The definitions of array, horn, and EO probe orientations are defined by convention.

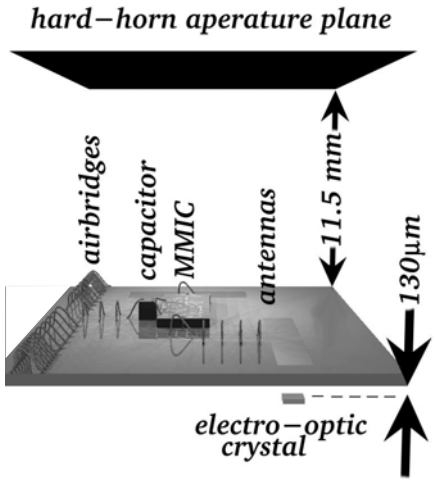

Figure 4.5. The relative dimensions of the array, EO probe tip, and horn aperture are drawn to scale in a perspective view.

An x-directed array orientation is equivalent to stating that the polarization of each input slot antenna in the array is parallel to the x-axis. The polarization of the feed horn is always oriented parallel to the array orientation and should be assumed as such for the remainder of this chapter. The EO probe orientation is defined by the field component that EO probe station is configured to measure. For instance, a y-orientation of the EO probe means the EO probe tip is oriented such that the EO probe station measures predominantly the y-component of the electric field.

The EO diagnostic measurements performed on the passive and active arrays are summarized in remaining sections. Note that all EO amplitude maps are plotted with the same scale; the normalized electric field varies from -20 dB to 0 dB and the corresponding color scale varies from black to white, respectively.

4.2.1 Feed horn characterization Both the phase and amplitude of a hard horn are designed to be uniform across its radiating aperture [15]. Uniform aperture distribution is necessary to uniformly excite the QO arrays and to achieve optimal QO amplifier array output power performance. The uniformity of the horn aperture is tested by measuring the near field of the horn aperture radiating into free space. By allowing the horn to

radiate into free space, any interactions (standing waves) between the array and the horn are removed from the experiment and the performance of the horn alone is characterized. This is achieved by placing the EO probe tip as near to the horn aperture as is possible without the array present. The EO probe tip polarization is then aligned with the polarization of the horn under test and an EO measurement is completed.

The measured phase of the three different horns used to excite the QO amplifiers is summarized in Figure 4.6. The EO phase map of the standard horn aperture, Figure 4.6(a),

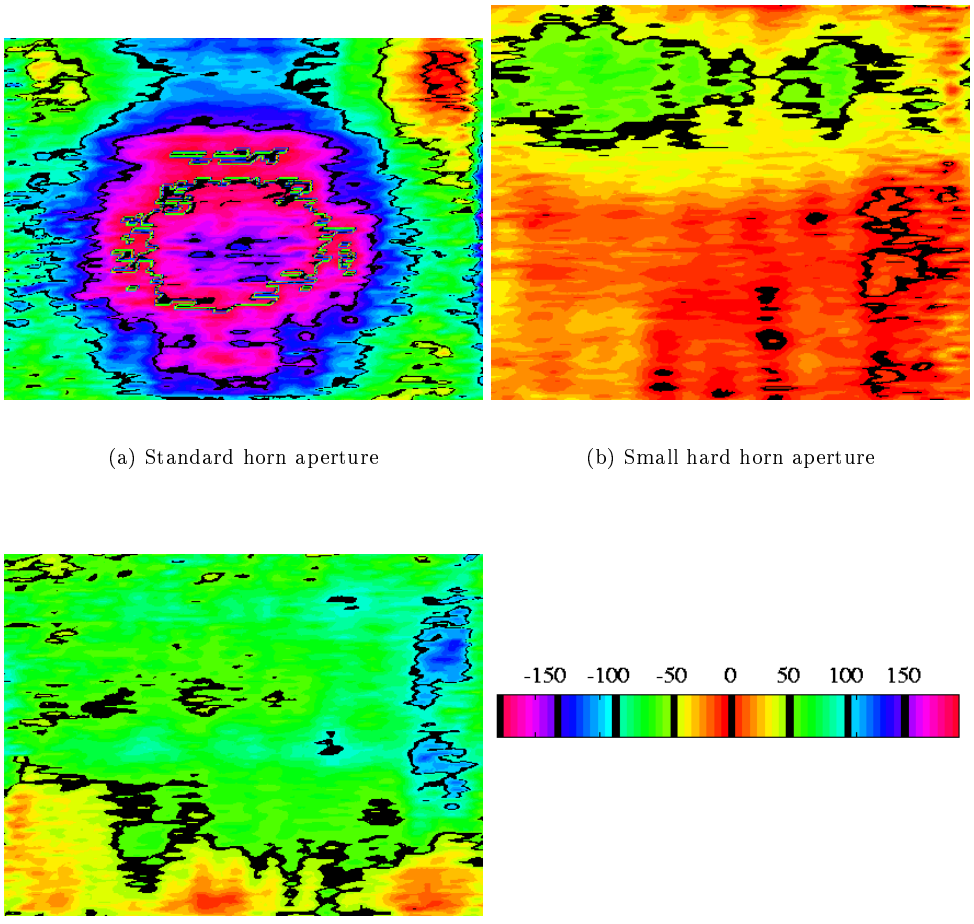

(a) Standard horn aperture

(b) Small hard horn aperture

(c) Large hard horn aperture

(d) Phase scale (°)

Figure 4.6. Measured EO phase maps [°] of three horn aperture feeds are shown. The standard linear-tapered far-field horn (a) aperture is 69 mm by 51 mm. The small hard horn (b) and large hard horn (c) apertures are 45 mm by 40 mm and 69 mm by 51 mm, respectively.

shows a large phase variation. This confirms the fact that the standard horn is designed for far-field gain and not near-field uniformity. Recall, the standard horn was used to excite the array in the far-field and was never intended for near-field use. On the contrary, the two hard horns show better phase uniformity. Ideally, the color of each hard horn phase plot should be uniform. Figure 4.6(b) shows a slight variation (green patch) which might indicate a problem with the small hard horn. Figure 4.6(c) shows a a similar variation which is concentrated near the lower half of the aperture. These variations may be due to some tilting of the horn when mounted in the EO probe station – at 31 GHz, a phase variation of 10° across the horn aperture corresponds to only 0.3 mm which is less than 1° tilt of the horn. Note that the horn should have been rotated 180° and re-mapped to confirm with certainty whether or not the horn was tilted.

To quantify the amplitude variation across each horn aperture, a cross section along the x-axis through the center of each aperture is taken from each EO data set and plotted in Figure 4.7. Figure 4.7 shows that there is at least a 5 dB amplitude variation across the

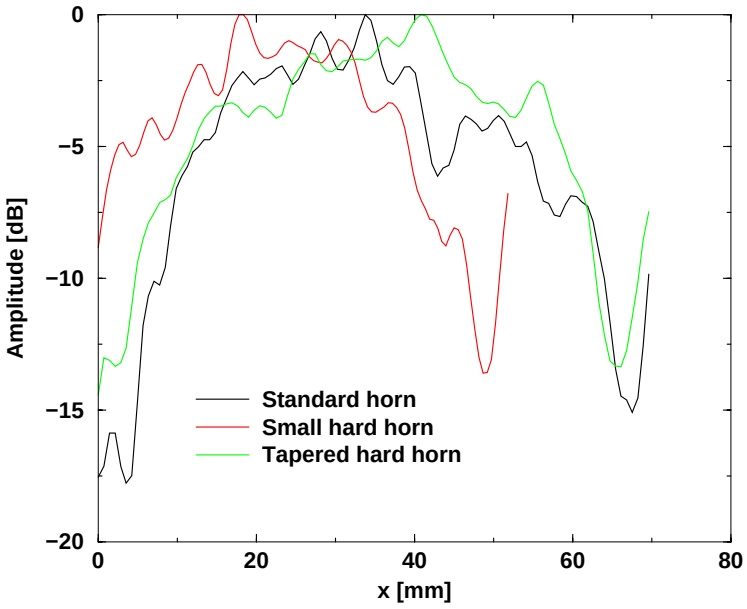

Figure 4.7. Measurement of co-polarized electric field amplitude [dB] for three different feed antenna apertures radiating into free space.

aperture of each feed horn radiating into free space which will certainly have a degrading effect on QO amplifier performance.

4.2.2 Passive array near-field measurements The passive array from Chapter 3 is mounted in the EO probe station. The array is oriented in the x-direction and the EO probe tip is oriented in the orthogonal y-direction. This setup measures predominantly the co-polarized electric fields of the output antennas and the horizontal CPW lines.

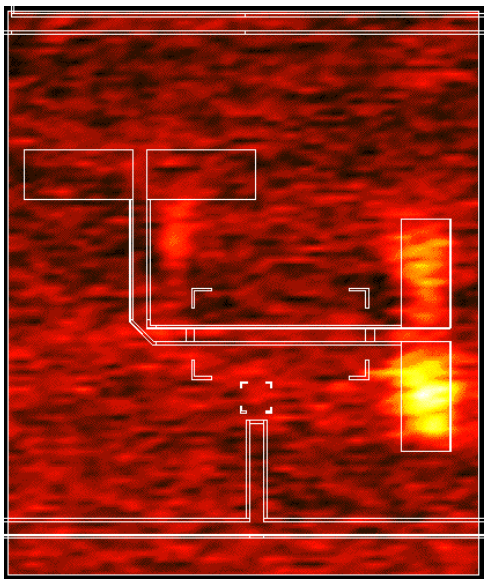

Figure 4.8: EO amplitude map for a unit cell in the passive QO amplifier array.

Figure 4.8 gives the result of the EO measurement of the passive array. The EO amplitude map shows little signal above the noise level. The near-field of the output antenna (lower right) is barely discernible. The reason for the low signal levels must be due to the fact that the RF input to the feed horn is too low. In future experiments, this could be improved by adding an external amplifier to the input of the feed horn – an expensive but practical solution.

The failure of this experiment is included to both demonstrate a limitation of the EO probe station and offer a reason to pursue this measurement in the future. Originally, the

goal of this experiment was to measure the electric fields along the CPW line and observe standing waves. Observation of standing waves would have been useful for determining how well an antenna is matched to the CPW line in an array environment. This would be an improvement in understanding over numerical models and the measurement of a single isolated antenna. Recall that the measurement of S_{11} for a single-isolated slot antenna, presented in Figure 3.10, did not take into account any mutual coupling effects and in addition, the numerical models of mutual coupling (see Section 2.7) are limited to a few elements. Understanding mutual coupling and its affect on QO amplifier power performance may be best understood through EO measurements over entire arrays.

4.2.3 Measurement of isolation between antennas The EO probe station is configured to measure the isolation between input and output antennas within the active arrays. Specifically, the active array and EO probe tip are both oriented in the y-direction. The input antennas should in principle have RF levels of the same order as the passive array (low levels). If the isolation between antennas is poor, a large fraction of the amplified power from each output antenna is coupled back into each input antenna. Therefore, the near field of the input antennas (which the probe is set to measure) should increase above the levels seen in the passive array, if poor isolation conditions exist.

A series of EO isolation measurements utilizing the large hard horn are summarized in Figure 4.9. Both active arrays (Array A and Array B) have similar near fields as in the passive array, in the sense that the the RF power levels are low. Hence, the output antenna does not couple enough power back into the input antenna to raise the RF levels significantly above the noise of the measurement. At best, this measurement only suggests that the coupling between input and output antennas is low.

As in the passive array experiment, another limitation of the EO probe station is documented. Further experiments are needed to be able to conclude that the isolation between input and output antennas is better than the design specification of 20 dB.

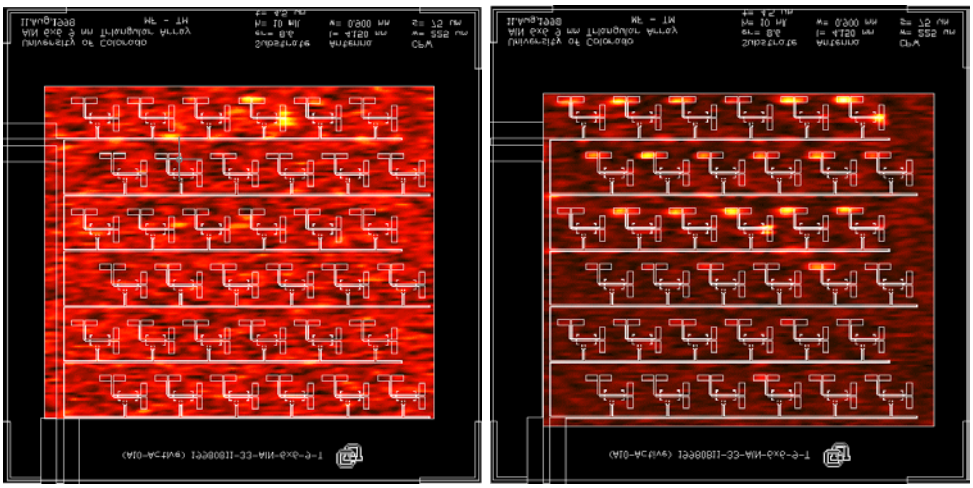

(a) Active Array A

(b) Active Array B

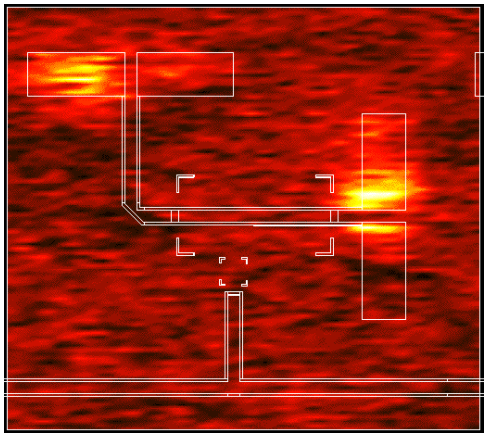

(c) Unit cell of active Array B

Figure 4.9. EO amplitude [dB] maps showing the y-polarized electric field magnitude, parallel to the input antenna polarization, of the active arrays under large HH excitation.

4.2.4 Bias-level effects on active array The bias level variation across the array was previously presented in Chapter 3. The DC voltage was measured as a function of position along the bias lines but the actual effect that this variation had on the RF output of the individual antennas was not determined. The EO probe station can remedy this by measuring the RF output of every unit cell.

Array B is placed in the probe station and two EO measurements are taken. The two measurements are taken at low and high DC power supply levels. Array B is oriented in the y-direction and the EO probe tip is oriented in the x-direction. Figure 4.10(a) shows

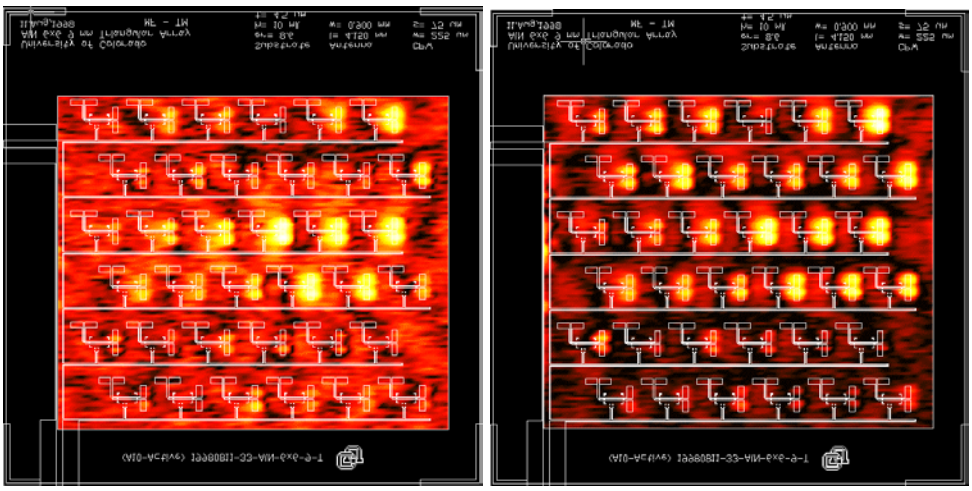

(a) Array B with bias of 3.42 V and 4.46 A (b) Array B with bias of 3.60 V and 4.50 A

Figure 4.10. Effect of array bias level on output antennas under large HH excitation is shown. The y-component (co-polarized with the output slot antennas) of the electric field is measured and the resulting EO amplitude map [dB] is shown for two different DC bias levels: (a) low bias and (b) high bias.

that only part of Array B is active at the lower bias level. As the bias level increases, more of the elements become active [see Figure 4.10(b)]. As expected, the variation in DC bias causes the decrease in gain of the MMICs which results in the decrease of power from each output antenna. Not all of the unit cells (top two rows) are active at the highest bias level due to the non-uniform hard-horn amplitude distribution (recall Section 4.2.1).

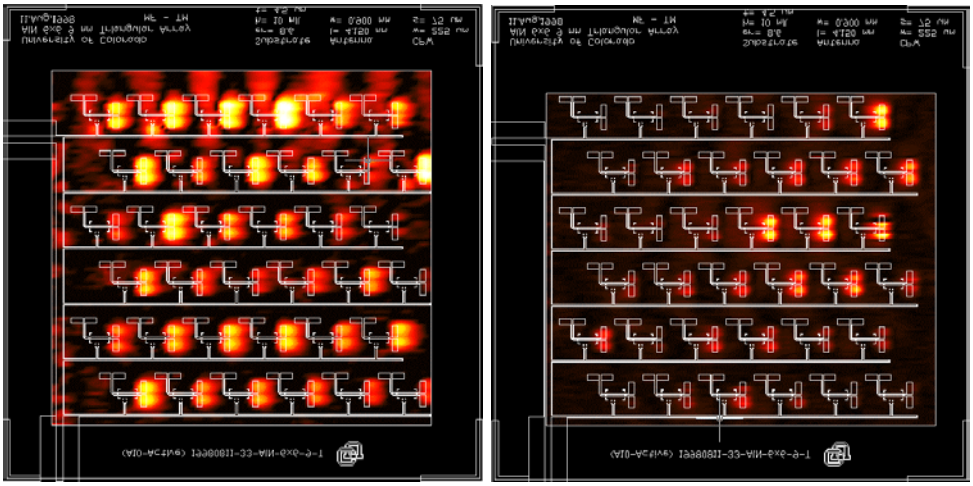

(a) Array A with bias of 4.17 V and 4.19 A (b) Array B with bias of 3.79 V and 4.52 A

Figure 4.11. Measured EO amplitude maps [dB] under large HH excitation. The probe is oriented to measure the x-component of the electric fields parallel to the output slot antenna.

4.2.5 Near field of active arrays with large hard horn feed Figure 4.11 shows both active arrays excited by the large hard horn. Comparing Figure 4.11(a) and Figure 4.11(b), it is observed that more of the unit cells are excited in Array A than in Array B. This is contrary to the expected result since Array B has the highest small-signal gain [recall Table 3.1(a)] under far-field illumination. Note that Figure 4.11(a) shows evidence of unwanted substrate modes in the lower edge of the array. Perhaps a non-uniform feed illumination breaks symmetry and encourages substrate modes. Recall that the far-field H-plane pattern measurement given in Figure 3.14(b) has unexpected side lobes at $\pm 90^\circ$ which can be explained by these substrate modes.

4.2.6 Near field of active arrays with small hard horn feed Contrary to the previous large HH experiment, more elements are excited in Array B than Array A (see Figure 4.12) when the small hard horn is used. The surprising result is that the highest output amplitude occurs on the far right side of the array which is farthest from the DC bus bar. Elements farthest from the bus bar are expected to have the lowest bias voltage

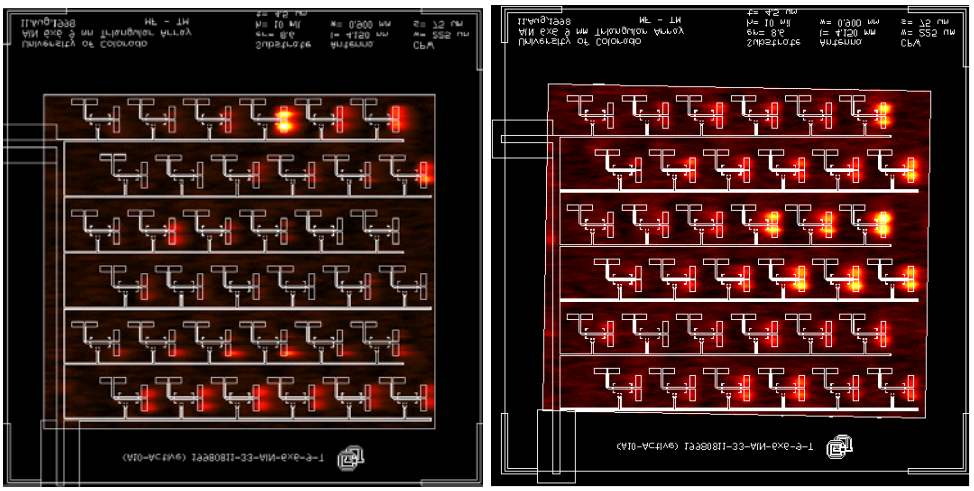

(a) Array A

(b) Array B

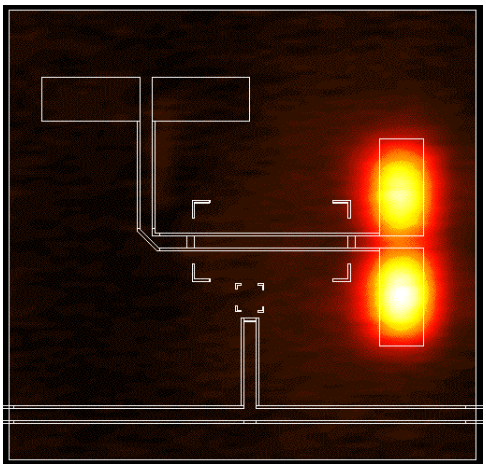

(c) Unit cell of Array B

Figure 4.12. Measured EO amplitude maps [dB] under small HH excitation. The probe is oriented to measure the x-component of the electric fields parallel to the output slot antenna.

and therefore, lowest gain. Perhaps the feed horn was misaligned with the array in this experiment.

Closer inspection, using a different log scale, clearly demonstrates that the relative excitation among unit cells is less uniform than expected. Figures 4.13(b) and (c) show two slices of the EO map (a). The x-slice plot (b) shows an amplitude variation which looks suspiciously like the horn aperture variation (first shown in Figure 4.6 and re-plotted here for clarity). The non-uniform electric-field amplitude of the hard horn adversely affects the excitation of the active QO amplifier.[3] The x-slice also clearly shows excess RF on the bias line at $x = 0\,\text{mm}$, comparable in amplitude to the nearest radiating output slot antenna. It is clear that the bias network needs to be redesigned.

4.2.7 Coupling measurement An attempt at measuring mutual coupling effects within QO amplifier arrays is presented in this section. Ideally, with no mutual coupling, if a single unit cell of an array is excited, adjacent unit cells will be unaffected and there will be no electric field induced in those adjacent unit cells. In reality, due to mutual coupling effects, the adjacent cells are affected and some induced electric field is present. The effects of mutual coupling can then, in principle, be studied by measuring the induced electric fields in the adjacent unit cells.

Figure 4.4(a) shows the implementation of the EO probe station that is used to excite a single unit cell and observe the induced electric field due to mutual coupling. Rather than exciting the entire array with a hard horn, a small waveguide (WG) aperture is used to excite a single unit cell within the array. The QO amplifier array is removed for discussion purposes in the figure to help visualize the location of the WG feed. The QO amplifier is actually present during all coupling measurements. The WG feed can be positioned at arbitrary locations under arbitrary unit cells within the QO amplifier. The polarization of the WG feed is aligned with the polarization of the input slot antenna (y-direction) for all

[3] Note that in these and future measurements, the horn should be rotated 180° to confirm that the amplitude variation is really due the horn feed alone.

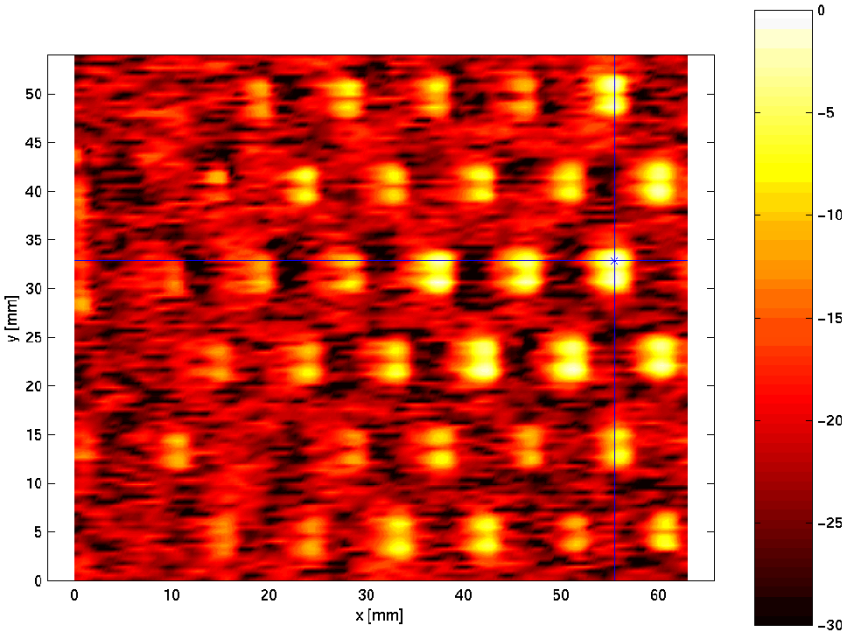

(a) x-directed electric field (dB)

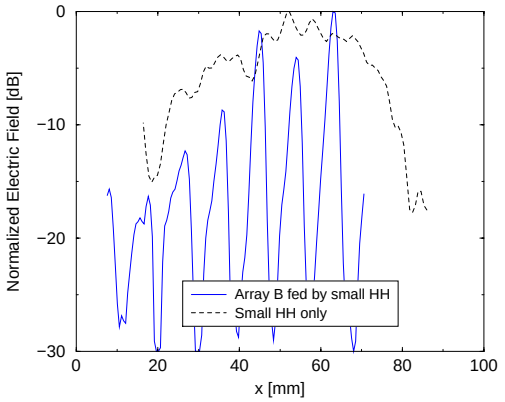

(b) x-slice of EO map; x=55 mm

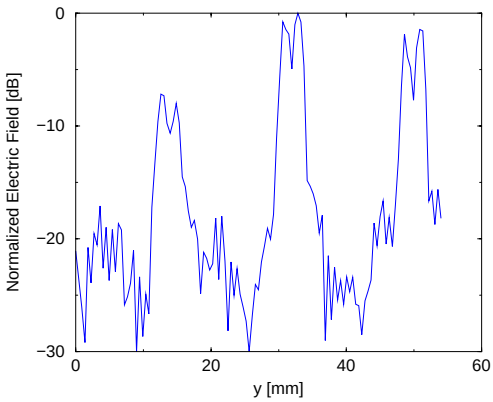

(c) y-slice of EO map; y=33 mm

Figure 4.13. EO amplitude map [dB] of Array B is re-plotted with a different scale. The horizontal line shown in (a) represents the position of the x-slice. The vertical line shown in (a) marks the position of the the y-slice. The intersection of the horizontal and vertical lines is the location of the maximum measured output field.

the measurements.

Both of the active arrays (Array A and B) are characterized by this technique (see Figure 4.14) under two different WG feed locations. In the first configuration, the WG feed is in the center of the array, and in the second one, the WG feed is near the corner of the array. The location and relative size of the WG feed is superimposed on each of the color maps. Note that the placement of the feed in relation to the input slot antenna is difficult to precisely align in practice. Figure 4.14 reveals that the electric fields decrease by at best 10 dB between unit cells; however, both arrays are designed to have isolation greater than 20 dB based on computer simulations (Section 2.7). The isolation is therefore worse than expected.

What is the dominant coupling mechanism which affects isolation? When the WG feed is at the center, Array B has less elements excited than Array A [compare Figure 4.14(a) and Figure 4.14(c)]. In both arrays, the induced fields tend to be confined along rows. Curiously, the row that is excited in Array A is not the same row in which the WG feed is located but rather the row below the WG feed. The output antenna therefore does not tend to couple into the nearest input antenna along the same row but rather into the input antennas below. This is further observed in Figure 4.14(b); when the WG is moved to the corner of the array where there are no rows below, only fields in the nearest unit cell along the same row are induced. In the case of Figure 4.14(d), the WG is placed in the upper right corner of the array. Unlike Figure 4.14(b), there is an input antenna below the output antenna and the unit cells are excited in a vertical fashion. The combination of these facts suggests that the dominant effect of mutual coupling occurs between the output antenna and the input antenna located directly below that same output antenna. Based on numerical simulation, these two antennas should have 30 dB isolation. There is a bias line which is located between the coupled input antenna and the nearby output antenna. The bias line promotes coupling between the two antennas.

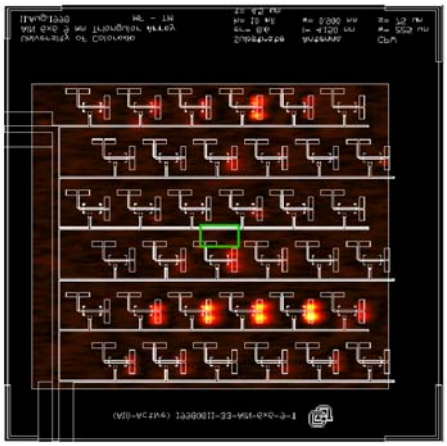

(a) Array A, WG feed in center.

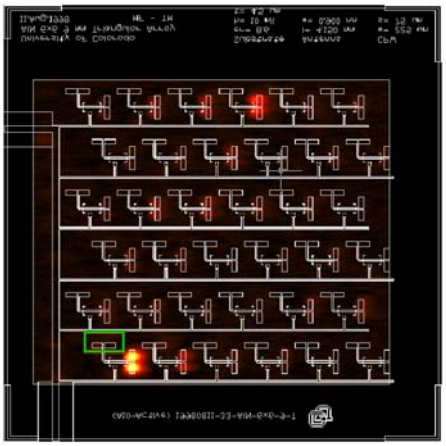

(b) Array A, WG feed in lower left corner.

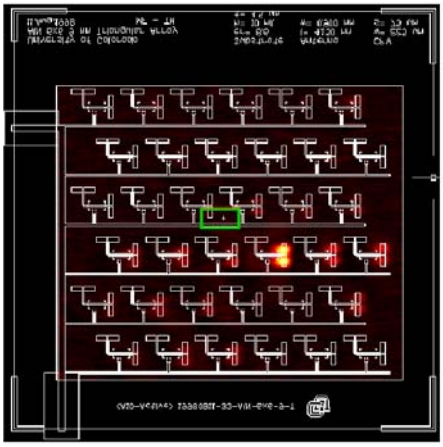

(c) Array B, WG feed in center.

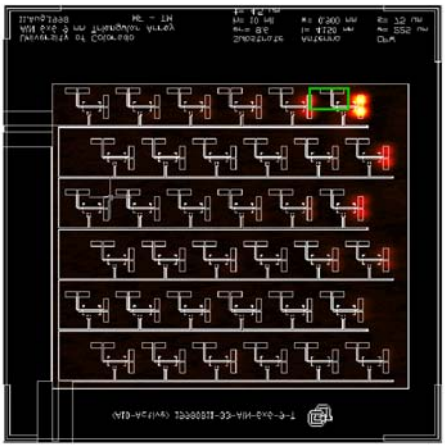

(d) Array B, WG feed in upper right corner.

Figure 4.14. Study of inter-element coupling based on EO amplitude [dB] measurements under waveguide (WG) aperture excitation is summarized. The aperture of the small waveguide feed is drawn to scale and is superimposed on each color map as a green rectangle.

Array A and Array B differ predominantly in their corresponding bias line designs. Array B has a bias line with more shorting capacitors and air bridges than Array A. Based on these EO measurements (Figure 4.14(a) and Figure 4.14(c)), Array B is better at reducing the effects of coupling than Array A. This fact suggests that a better bias line design is needed which further reduces the effects of mutual coupling between input and output antennas.

4.2.8 Calculation of far-field radiation pattern This section presents a method of calculating the far-field radiation pattern from near-field measurement data. The far-field radiation pattern can be determined from the magnetic surface current density ($\vec{M}_s$) of an aperture [16]. Specifically, the far-field electric field is given by

$$
\begin{aligned}
E_\phi &= \frac{-jk}{4\pi r} e^{-jkr} L_\phi \\
E_\theta &= \frac{jk}{4\pi r} e^{-jkr} L_\theta \\
L_\theta &= [L_x \cos\phi + L_y \sin\phi] \cos\theta - L_z \sin\theta \\
L_\phi &= -L_x \sin\phi + L_y \cos\phi \\
\vec{L} &= \int\int_{A'} \vec{M}_s \exp^{jkr' \cos\Psi} \, dA' \\
\cos\Psi &= \cos\theta \cos\theta' + \sin\theta \sin\theta' \cos(\phi' - \phi)
\end{aligned}
\tag{4.2}
$$

The magnetic current is directly proportional to the electric field (amplitude and phase) measured by the EO probe station. The far field is typically normalized to a peak value so $\vec{M}_s$ is replaced by the measured electric field data. Since the measured electric-field is discrete, the double integral is approximated by the corresponding double sum. The calculation of the far-field is simplified by the fact that the sources are located only in the plane of the array ($\theta' = 90°$). One limitation of the EO probe station is its inability to measure the absolute values of all three (x,y,z) electric field components simultaneously; consequently the cross-polarized components of the electric field are ignored in this calculation.

The calculation of the far-field pattern based on Eqn.(4.2) is performed using two different EO measurement data sets. The first data set utilizes the near-field data from the

measurement of the unit cell shown in Figure 4.12(c). The second uses data from the entire active Array B shown in Figure 4.12(b). Figure 4.15(a) demonstrates the ability of the EO probe station to predict the far field due to a single slot antenna in an array environment. Note that the E-plane would be omni-directional if not for the AlN substrate. Figures 4.15(c) and (d) show the calculated far fields of active Array B. The number of side-lobes agrees with the expected Array B radiation pattern but the absolute side-lobe levels do not agree. The disagreement is due to the fact that no polarizers are used in the EO measurements which makes a direct comparison with the actual far-field pattern measurements of Section 3.2.5 difficult. Note that the 3-dB beamwidth of the array is calculated to be 16.2° from the EO measurement data which is 6.4° larger than expected.

4.3 Conclusions and possible design improvements

The EO probe station proved to be valuable in determining the near-field of QO amplifier arrays and diagnosing problems. There is sufficient detail in the EO measurements to see if a CPW line is radiating or even to see if the mode of the slot antenna is anti-resonant. Complicated interactions between the various elements in an amplifier array were measured and visualized: hard-horn feed interaction with output slot antenna, single unit cell excitation with coupling to nearest neighbors, and output slot coupling RF onto nearby bias line, to name a few examples presented in this chapter.[4]

Table 4.2 summarizes problems with the QO array designs based on EO measurements and suggests possible design improvements. The DC bias has design flaws which result in excessive DC voltage variation and RF power coupling onto the bias lines. The problem of bias variation was discussed in Chapter 3 and based on Section 2.6, this can be improved by reducing bias-line resistance. The RF power on the bias lines is of more concern and is

[4]It is interesting to note that these interactions are difficult to study numerically with the current state of the art in computational electromagnetics. Therefore, the EO probe station could be even more useful if it were used to better understand these interactions. For instance, future experiments could be devised to study mutual coupling.

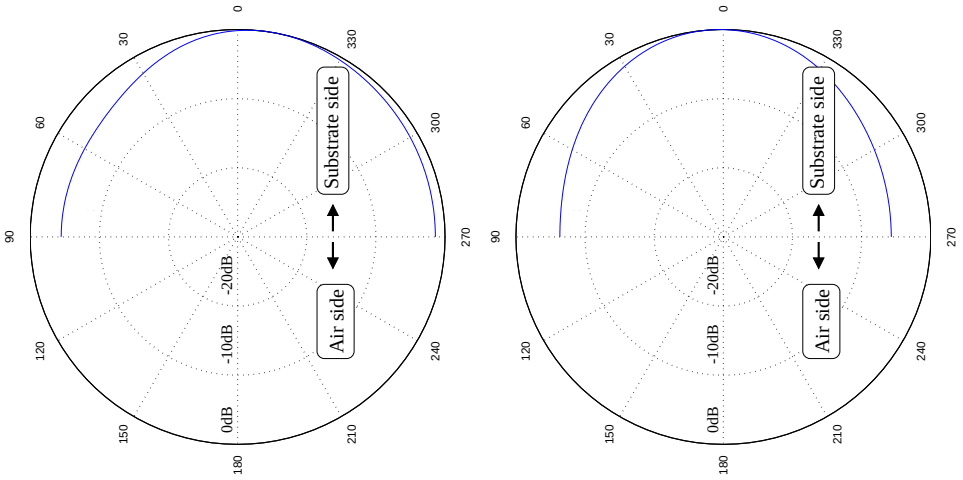

(a) E-plane of the single slot antenna.

(b) H-plane of a single slot antenna.

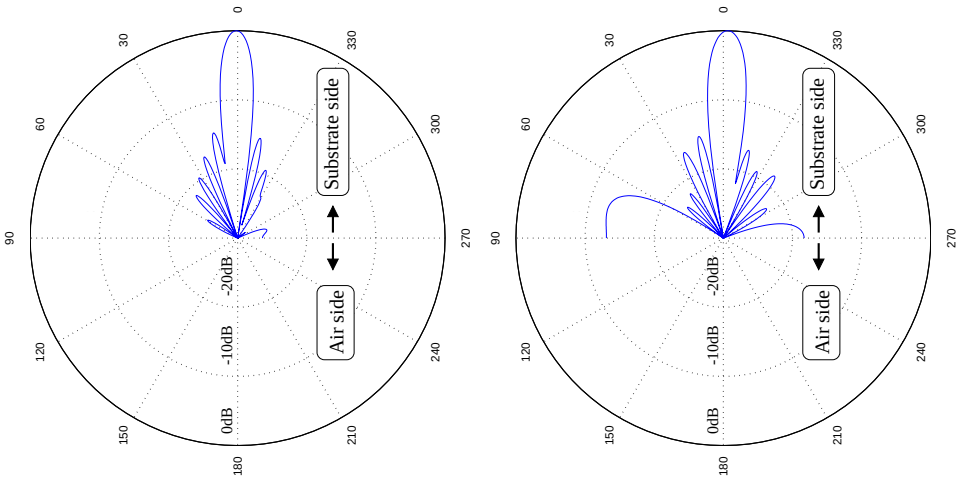

(c) E-Plane of Array B

(d) H-Plane of Array B

Figure 4.15. Normalized far-field radiation patterns [dB] are calculated from the measured near-field data without polarizers.

Table 4.2: Possible design improvements based on EO experiments.

Problem	Possible remedy
Non-uniform DC	Reduce ohmic losses by using thicker metalization
RF on bias lines	Move output slot farther away from bias line Add more shorting capacitors along bias lines Shield the bias line from RF
Non-uniform output antenna excitation across array	Improve hard horn Use far-field feed Use Gaussian lens feed system Use lower gain MMICs
Substrate modes	Reduce substrate thickness more Photonic band gap substrate? (Difficult with AlN)

a major reason why the array oscillates before the maximum gain of each MMIC is realized in actual array operation. Some solutions to remove the RF from the bias lines are to move the output antenna farther away from the bias line, add more capacitors along the bias line to short any RF to ground, or use lower gain MMICs. Moving the bias line farther away is not a good solution since the unit cell is already large and this leads to unwanted radiation side lobes. The addition of capacitors was tried and had limited success. More effort needs to be put into designing an effective RF shield for the bias lines.

The non-uniform amplitude problem is partially due to the hard horn feed. The present hard horns used for the measurements are too small. The hard horn aperture has a smaller area with uniform phase and amplitude than the physical area of the current arrays. There is as much as 5 dB variation in amplitude across the array due to the small size of the hard horn. The hard horn needs to be redesigned with a larger area of uniform phase and amplitude. Another solution may be to replace the hard horn feed with a Gaussian lens system which is capable of producing a larger uniform beam for excitation of the array but this makes the entire QO system larger.

The last problem of substrate modes is not easily removed. The use of thinner substrates may help reduce the amount of power lost to substrate modes. Substrate modes can never be eliminated by simply decreasing the substrate thickness since no cutoff frequency

exists for thin dielectric substrates. However, photonic band gap (PBG) substrates are known to suppress substrate modes at certain frequency bands [44]. PBGs are created by selectively placing holes in the substrate at regular intervals. AlN is not a suitable substrate for this PBG technique since it is a ceramic which is weakened by holes. If a PBG substrate were to be used the entire design process of Chapter 2 would have to be repeated using a new antenna design, a new study of coupling on the PBG substrate, determination of thermal properties, etc.

CHAPTER 5

A KA-BAND QO AMPLIFIER WITH A NEW MMIC AND BIAS NETWORK DESIGN

Based on the far-field measurements (Chapter 3) and near-field diagnostics (Chapter 4) of the QO amplifiers, discoveries were made which explained the performance problems of the first QO amplifiers presented in this thesis. Those discoveries suggest that some basic design alterations may be possible which should improve the QO amplifier stability, gain, and power performance (recall Table 4.2). In this chapter, the QO amplifier is redesigned, fabricated, and characterized. The goal is to make this QO amplifier stable at full bias, and therefore, achieve greater output power than the previous arrays.

5.1 Design

The QO amplifier design presented in this section is an evolutionary change from the previous QO amplifiers of Chapter 2. This new design builds upon previous successes and concentrates effort onto eliminating observed failures. The previous design succeeds in three areas: the slot antenna on AlN is well matched (Figure 3.10); the triangular $0.9\,\lambda$ array layout yields acceptable side lobe radiation levels (Figure 3.13); and the thermal properties of the AlN substrate keep the active array within safe thermal operating conditions for the MMICs under maximum bias conditions (Section 3.2.1). Therefore, the antenna design, triangular array lattice, and the AlN substrate need not be changed. The previous design has four main flaws: the prior *Alpha* AA028P3-00 MMIC amplifier is outdated by recent advances in MMIC technology that can achieve higher power at lower cost; the resistive ladder network

comprised of DC bias and MMIC impedance has at most 10% bias variation across the array (Figure 3.15); the DC bias lines fail to suppress RF coupling completely [Figure 4.14(d)]; and the hard-horn near-field feed causes a large non-uniform array excitation (Figure 4.13). Remedies to these observed design flaws are used to determine a new and improved design

The new design is summarized in Figure 5.1. As mentioned earlier, some parts of the QO amplifier remain unchanged from the previous designs (Arrays A and B): the same 254 μm (10 mil) AlN substrate is used; the second-resonance slot antenna is still 4.15 mm long and 0.9 mm wide; the CPW lines have dimensions of $W_{\mathrm{CPW}} = 225\,\mu$m and $S_{\mathrm{CPW}} = 75\,\mu$m; and the triangular array lattice utilizes a 9 mm unit cell size. The obvious changes to the array design are the new MMIC, dual bias, removal of vertical bus bar, addition of insulator, and addition of Cu shield. Each of these design changes will now be explained.

Of the currently available MMICs (recall Table 2.1 from Chapter 2), the *Alpha* AA032P1 MMIC is chosen to replace the *Alpha* AA028P3-00 MMIC. The *Alpha* AA032P1 MMIC is half the cost, has 8 dB more output power, and has 5 dB less gain than the previous *Alpha* AA028P3-00 MMIC. The new MMIC has a gain (S_{21}) of 14 dB which is equal to the maximum average gain contributed by the *Alpha* AA028P3-00 MMICs in the previous active arrays (recall Table 3.1 from Chapter 3). The previous arrays became unstable when the average MMIC gain increased above 14 dB. By choosing a lower gain MMIC with higher output power, the QO amplifier should be stable at full DC bias levels, and therefore, more output RF power should be achievable.

The DC bias is completely redesigned to correctly supply the new dual bias MMIC, to reduce array DC voltage variation, and to suppress RF coupling. Separate drain and gate lines are required by the *Alpha* AA032P1 MMIC and are shown as horizontal lines in Figure 5.1. Unlike the previous design which has a single vertical bus bar (recall Figure 2.3, page 30) that connects the bias lines for each row together on the substrate, each row in the new array has an independent set of bias lines (drain and gate) that separately connect

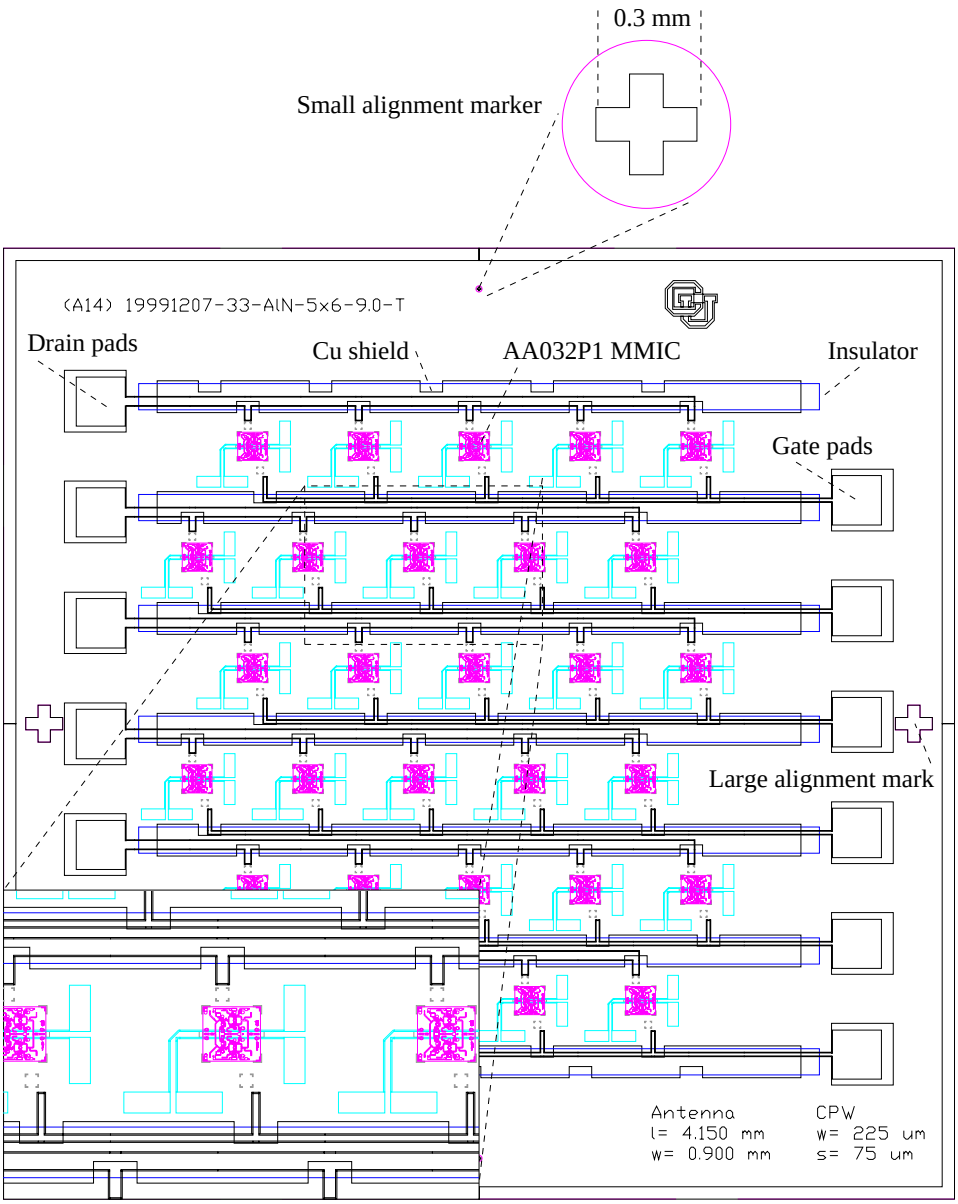

Figure 5.1. Final design of the improved amplifier array is shown. The unit cell dimensions are 9 mm by 9 mm. The unit cells are arranged in a triangular lattice. Each *Alpha* AA032P1 MMIC requires dual (drain and gate) DC bias. Each bias line is covered by a thin electrical insulator (blue rectangle) and a copper (Cu) shield to reduce coupling.

to the DC power supplies by means of the large drain and gate pads. The elimination of the vertical bus bar from the thin metalization of the substrate forces the variation in DC voltage to be constrained by only the number of elements in a single row and not by the total number of array elements. Since there are fewer elements (5) in a row as compared to the number in the entire array (30), the DC voltage variation can more easily be controlled and designed. Specifically, the drain line width (0.7 mm) is designed to have less than 5% DC voltage variation along a row using Eqn.(2.19). The width of the gate line (0.24 mm) is smaller since little current flows into the gate of each MMIC; the bias variation of the gate is well below 1% with this design.

To better suppress RF bias line coupling, a RF shield is fabricated on top of the individual bias lines. The bias line shield consists of a thin insulator that is placed on top of the DC bias lines on which a uniform metallic copper layer is deposited. The shield acts as a distributed capacitor which tends to short any RF on the DC line to ground, and therefore eliminate RF bias line coupling. In addition to the bias shield, discrete capacitors are still placed as near as possible to each MMIC and its bias line stub connection (as was done in Arrays A and B previously).

The remaining problem that needs to be addressed is the hard-horn feed and its inability to produce a uniform array excitation. Recall from Section 1.3 that an alternative to the hard-horn feed system is the Gaussian beam system which promises a uniform array excitation with low feed loss. Therefore, a Gaussian beam system is used in this chapter to characterize the new array design. However, before measurement results can be given, the details of the fabrication of the new array need to be summarized. For convenience, the new array (Figure 5.1) that is fabricated will be referred to as Array C for the remainder of this thesis.

5.2 Fabrication

Most of the fabrication steps required to make Array C are familiar and unaltered from the fabrication steps previously documented in Chapter 3, Section 3.1. Therefore, the material presented in this section concentrates on explaining the new fabrication details involved in making Array C. The main new fabrication challenges are the addition of the bias line shield and the improvement of the jig which provides DC bias while simultaneously holding the fragile AlN substrate securely.

5.2.1 The bias line shield There are three steps involved in the fabrication of the bias line shield: etching bias lines, CPW lines, and slot antennas; deposition of the insulator layer; and the deposition of the Cu shield layer. In all three cases, a photolithography step is required and positive AZ4210 photoresist (PR) is used.

The first step is to etch the gold (Au) from the AlN substrate to form the bias lines, slot antennas, and CPW lines. An identical procedure as described in Chapter 3.1.1 except with the different design mask for Array C yields the unit cell pictured in Figure 5.2. The

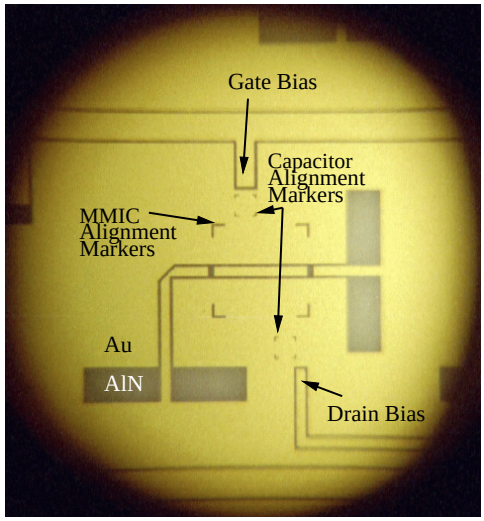

Figure 5.2: Photograph of a unit cell of Array C prior to bias line shield fabrication.

picture shows that the Au (yellow) metalization is removed from the AlN (grey) substrate to form the basic features of the Array C unit cell. The input and output antennas are now

visible along with the CPW transmission lines. The fat drain bias line and the thin gate bias line are visible above and below the MMIC and capacitor alignment markers.

The second step is to deposit the electrical insulator on top of the bias lines using the insulator mask show in Figure 5.3(a). The final step in the bias shield fabrication is to deposit a conductor on top of the insulator with the Cu shield mask [see Figure 5.3(b)]. Rather than

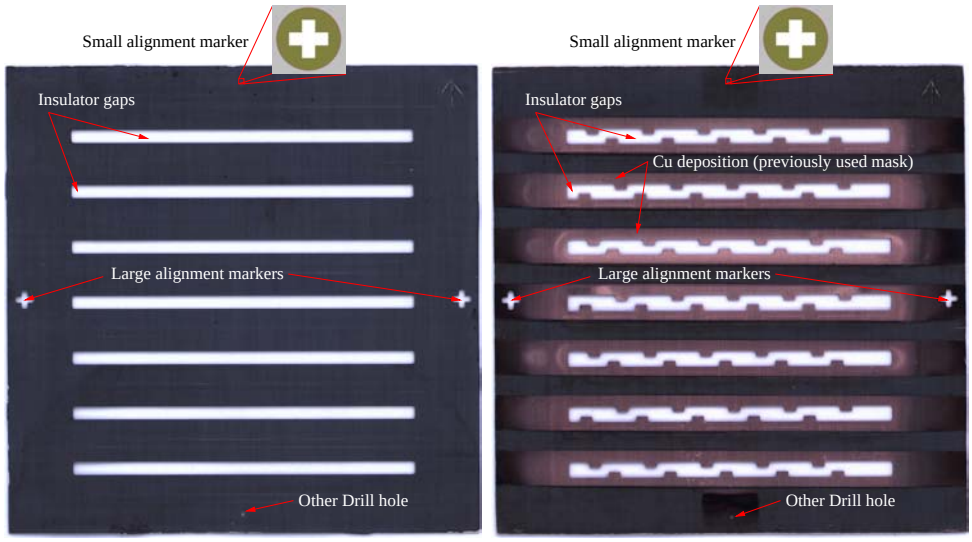

(a) Insulator (NR61) shadow mask (b) Shield (Cu) shadow mask

Figure 5.3. The two shadow masks required for the bias line shields; (a) the insulator mask, (b) the shield mask. The small alignment marker for masks (a) and (b) is actually a single 0.51 mm (20 mil) diameter drill hole. The alignment of either mask to the AlN substrate is accomplished by aligning the 0.51 mm (20 mil) hole with the small alignment cross etched into to AlN substrate prior.

printing these masks on clear mylar sheets, both the insulator and the Cu shield masks are milled from 0.38 mm (15 mil) thick *Rodgers* TMM6 substrate to make shadow masks. The reasons for the shadow mask (a mask with physical gaps) as opposed to the mylar mask (a mask with no physical gaps) are due to the way that the insulator and the copper are deposited and will become apparent shortly. TMM6 (as opposed to soft substrates or even thick metals) is chosen because of one advantageous reaction it has to milling; all milled gaps in *TMM6* have sharp crisp edges.

Both the insulator layer and the Cu shield layer must be aligned with the bias lines already etched onto the AlN substrate. Alignment of either shadow mask and AlN substrate is accomplished utilizing the small alignment AlN cross (see Figure 5.1) and the small 0.51 mm (20 mil) alignment hole of the shadow mask (see Figure 5.3). A custom shadow mask jig (shown in Figure 5.4) is necessary for mask alignment. The shadow mask jig consists of three plates. Rough mask alignment is accomplished by placing the AlN substrate on the bottom plate, the middle plate is placed around the AlN substrate, then the shadow mask is placed in the window formed by the middle plate. Fine alignment of the mask is completed using tweezers under a microscope looking at the small alignment markers. Once everything is aligned, the top plate of the shadow mask jig is bolted on top of the Bottom-AlN-mask-Middle stack. A final check is accomplished by looking through the top plate alignment window under the microscope which should confirm that the holes are aligned. For reference purposes, this procedure is referred to as the shadow mask alignment procedure for the remainder of this thesis.

Note that the shadow mask alignment procedure is tedious but yields acceptable results as demonstrated in Figure 5.5. The tolerance in the x-direction is allowed to be large (1 mm) but the critical alignment in the y-direction is much smaller (0.1 mm). The photograph shows the result of an actual shadow mask alignment process after the mask is removed and the positive photoresist remains. The alignment is measured to be within acceptable tolerances since $\Delta x = 0.2$ mm and $\Delta y = 0.1$ mm.

The insulator is now placed onto the AlN substrate in two stages summarized in Figure 5.6. Beginning with a clean AlN substrate [Figure 5.6(a)], positive AZ4210 photoresist is spun onto the substrate at 2000 RPM for 30 seconds and baked at 90 ° C for 20 minutes. The insulator mask [Figure 5.3(a)] is then aligned to the substrate using the substrate alignment procedure and exposed to UV light for 120 seconds. The substrate is removed from the jig and developed in AZ400K for 65 seconds which is followed by a postbake for 20 minutes

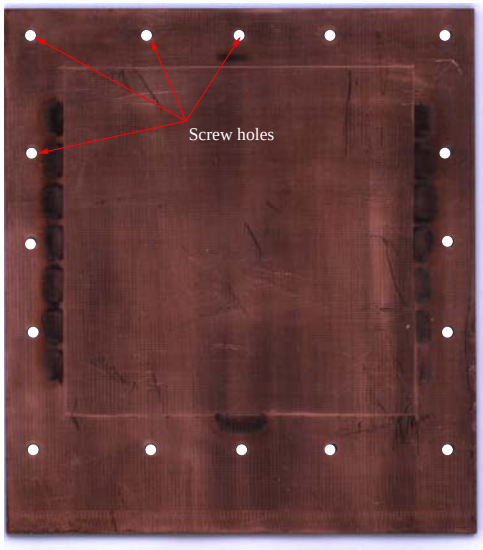

(a) Bottom

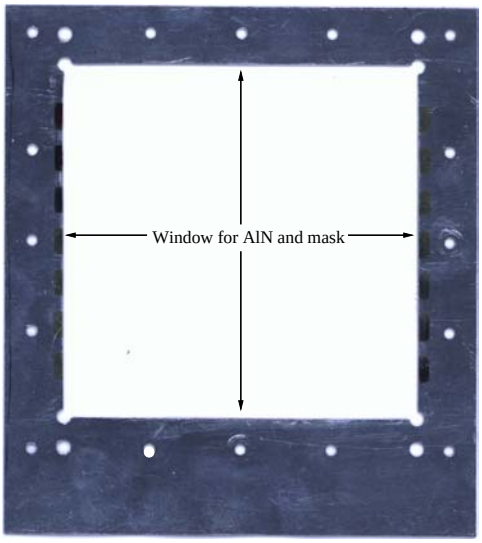

(b) Middle

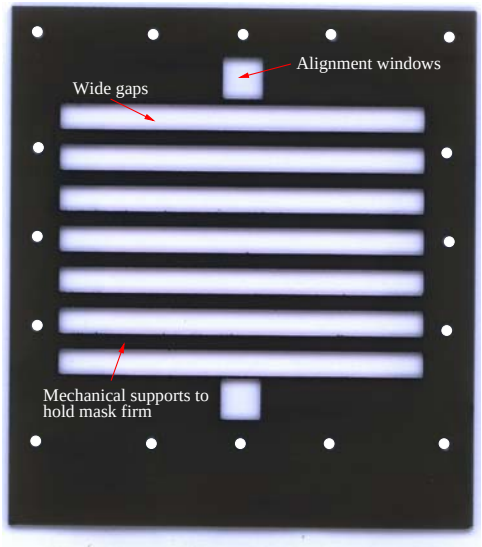

(c) Top

Figure 5.4. The shadow mask jig; (a) bottom layer is a rigid-solid FR4 backing plate on which the AlN substrate rests, (b) the AlN substrate and the desired shadow mask are roughly aligned in the middle window, (c) the top layer is bolted over the entire stack to mechanically secure the shadow mask onto the AlN substrate.

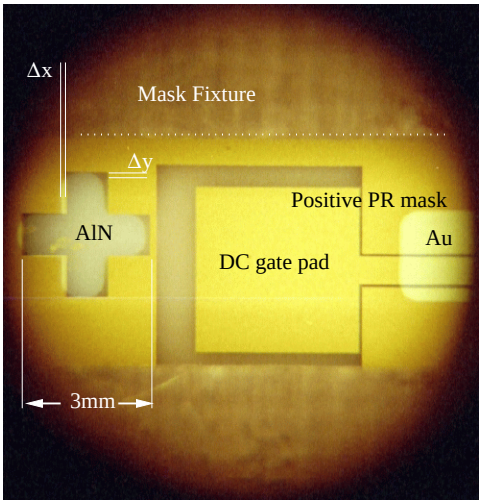

Figure 5.5. Photograph demonstrates the alignment tolerance of shadow mask. The large alignment cross (3 mm by 3 mm) is shown on the left side of DC pad. Δx and Δy are ideally zero when the mask and the AlN perfectly align with each other.

at 120 ° C. Finally, the substrate is ready for the insulator [see Figure 5.6(a)].

Many different electrical insulators were tried but proved to be unsuccessful. By accident, one particular material, *Norland* NR61 optical adhesive, proved to work.[1] *Norland* NR61 is a liquid that hardens when exposed to UV light. The problem with *Norland* NR61 is that it has to be painted onto the substrate with a fine needle by hand under the microscope (a process which takes approximately two days for 6 bias lines). Otherwise, the process works well because of surface tension of the NR61 which causes the NR61 liquid to repel from positive photoresist. Once the bias lines are painted with NR61, the substrate is placed under a UV lamp for 20 hours and then the substrate is baked in a 50 ° C oven for 7 hours. The thickness of the NR61 insulator is measured to be 50 μm.[2] The final result after removing the positive photoresist with acetone is shown in Figure 5.6(c).

[1] Jim Vian suggested that *Norland* NR61 be tried. He had been using *Norland* NR61 for a different purpose (mounting optical fibers). It had favorable mechanical properties which made it suitable for the bias line insulator.

[2] Ideally, the insulator thickness should be much smaller than 50 μm but was the best that could be accomplished by the author. Note that in [45] a thinner (20 μm thick) low-permittivity photosensitive Heraeus ink (KQ 110) was used to make dielectric bridges for CPW transmission lines and in [46] a more involved process (MCM-D) was used to achieve an even better 2 μm. Possibly, the Heraeus ink could be used to simplify future bias line shield fabrication and to improve RF performance by decreasing the insulator thickness.

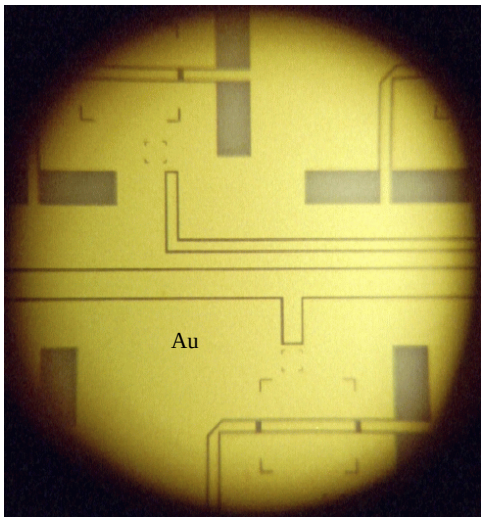

(a) Bare bias line

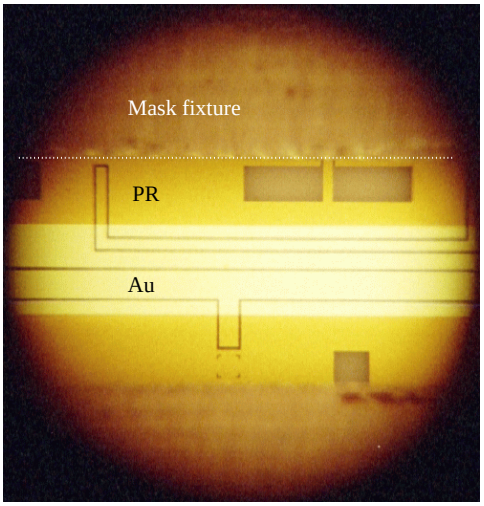

(b) After photoresist mask step

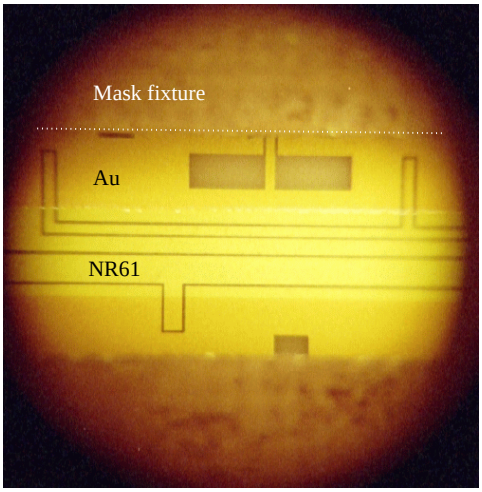

(c) After insulator deposition

Figure 5.6. Photographs of the insulator; (a) before the photoresist is deposited, (b) after the PR is deposited, (c) after NR61 insulator is deposited and PR removed.

The final step of placing copper onto the NR61 insulator is accomplished with the Cu shield mask [Figure 5.3(b)] and the steps are summarized in Figure 5.6. Again positive

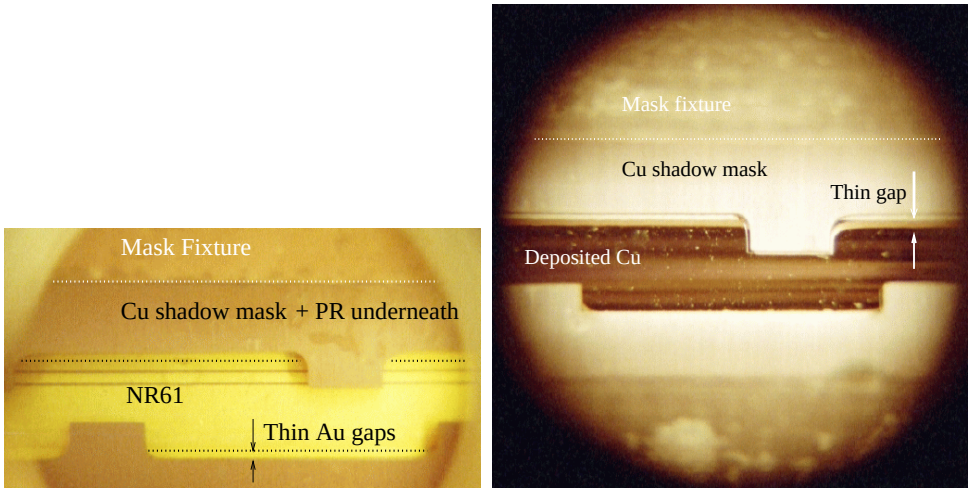

(a) Before Cu deposition (b) After Cu deposition

Figure 5.7. Photographs before and after the Cu deposition step. The mask fixture holds the Cu shadow mask on top (a) of the AlN substrate. The PR is not visible since it is aligned underneath the Cu shadow mask. After Cu deposition (b), the Cu on the insulator (NR61) is clearly visible due to the smooth NR61 insulator beneath.

photoresist is placed onto the AlN substrate, developed with the Cu shield mask, and the Cu shield mask is returned [as shown in Figure 5.7(a)] to the shadow mask alignment jig. At this point, the shadow mask alignment jig with the substrate is taken to Lockheed Martin where copper is sputtered onto the substrate [47]. The result is shown before the shadow mask is removed in Figure 5.7(b). Next the array is removed from the shadow mask alignment jig, the positive photoresist is removed with acetone and any excess copper is scrapped away with a needle point. The completed bias line shield is shown in Figure 5.8. The Cu shield on top of the NR61 insulator is visible on the upper and lower bias lines. The NR61 insulator boundary is delineated by the black dotted lines since the NR61 is transparent. The actual bias stubs extend beyond the NR61 insulator boundary for DC bias line to MMIC bond wire connections.

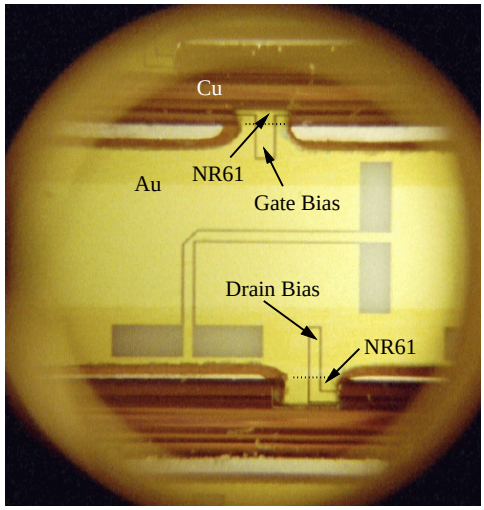

Figure 5.8: A photograph of passive unit cell after the bias line shield is completed.

5.2.2 Substrate and DC bias jig The assembly of the QO amplifier array (see Figure 5.9) begins by placing the AlN substrate, with completed bias shield, into the QO amplifier jig. The jig provides both mechanical support for the AlN substrate and DC bias through 4-terminal male *Berg* snap connectors. The front-side view Figure 5.9(a) shows each of the two *Berg* connectors for the drain and gate bias. The front-side features (slot antennas, bias pads, etc.) are visible in the backside view [Figure 5.9(b)] due to the slight transparency of the AlN substrate. This picture shows the array and jig before any MMICs or DC connections are completed. The following discussion explains how the DC connections are fabricated.

The QO amplifier jig (see Figure 5.10) consists of four parts: bias part, AlN cover, window, and AlN support. The four parts (a-d) are stacked on top of each other to form the assembled jig of Figure 5.9. Similar to the shadow mask alignment jig, the AlN substrate is placed on top of the AlN support part (d) with the *TMM6* window part (c) providing rough alignment and lateral support for the AlN substrate (details are shown in Figure 5.11). The AlN substrate rests on the support substrate and the *TMM6* window prevents the array from moving in the x- or y-directions. However due to thermal expansion, slight movement is

(a) Top down view (front side) (b) Bottom up view (backside)

Figure 5.9. Photographs of assembled QO amplifier prior to DC bias and MMIC attachment.

necessary to avoid cracking the AlN substrate and is achieved by making the *TMM6* window 0.4 mm larger on each side than the AlN substrate. The AlN cover part (d) is made from electrically non-conductive 1.57 mm (62 mil) thick FR4 substrate material which is placed on top of the (d-AlN-c) stack to completely support the AlN substrate mechanically. Finally, the bias part is placed on top to form the QO amplifier assembly.

The details of the bias part are shown in Figure 5.12. The bus bars (ground, drain, and gate) are made of 635 μm (25 mil) thick copper sheets which drastically reduce ohmic losses and DC bus bar voltage variation. The ground bus bar is on the top side of the FR4 insulator. The drain and gate bus bars are on the bottom side of the FR4 insulator. Figure 5.12(b) shows two gaps which serve to isolate the drain and gate bus bars from one another electrically. A bias wire is connected to a bus bar with snap U-clips which are held in place by mechanical force. The bias wires are color coded: ground is black; drain is red; and gate is green. The gate bus bar is connected to the inner two pins of its *Berg* connector which pass through both the ground bus bar and FR4 insulator. The inner two pins are

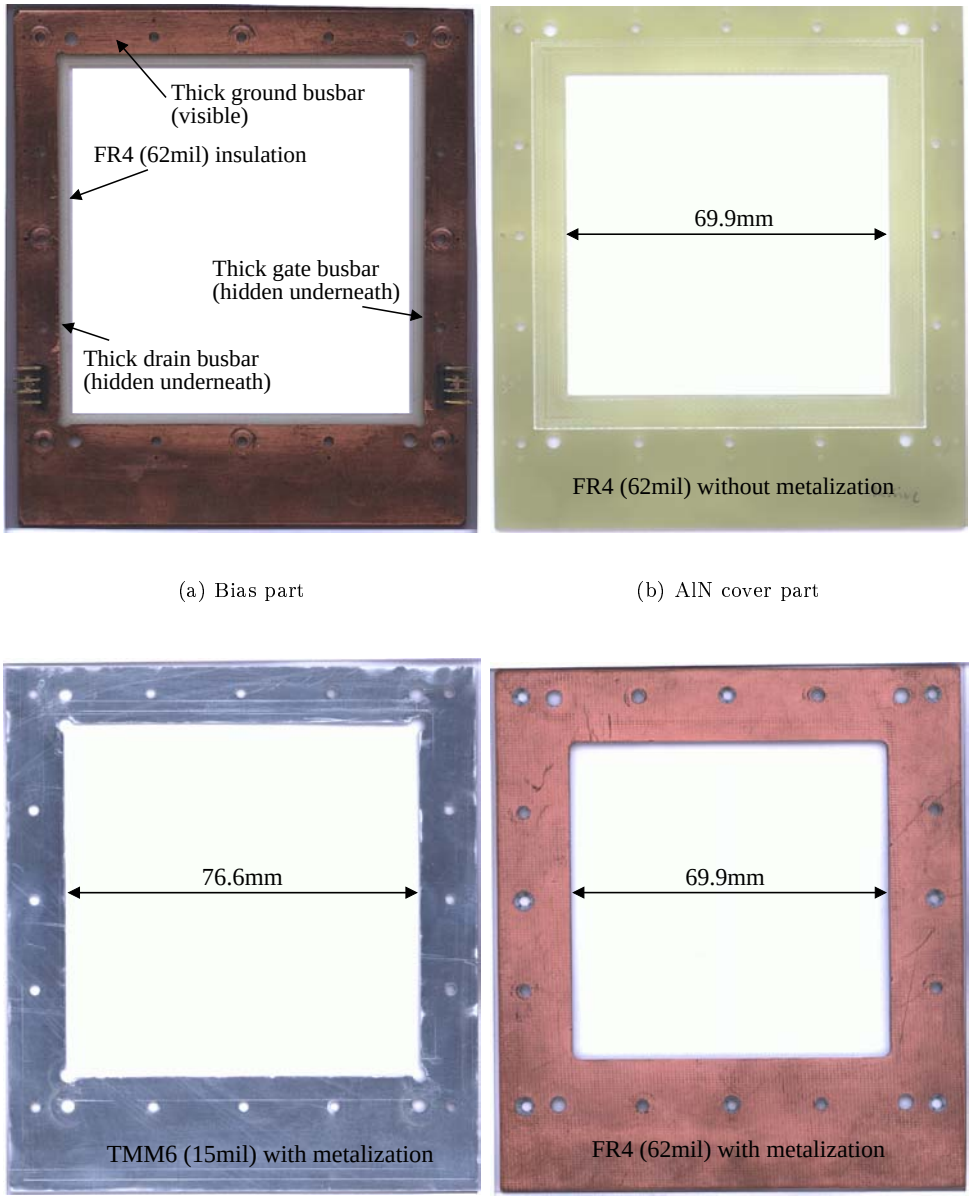

(a) Bias part

(b) AlN cover part

(c) *TMM6* Window part

(d) AlN support part

Figure 5.10. The QO amplifier jig has four main parts: (a) Bias; (b) AlN cover; (c) *TMM6* window; and (d) AlN support.

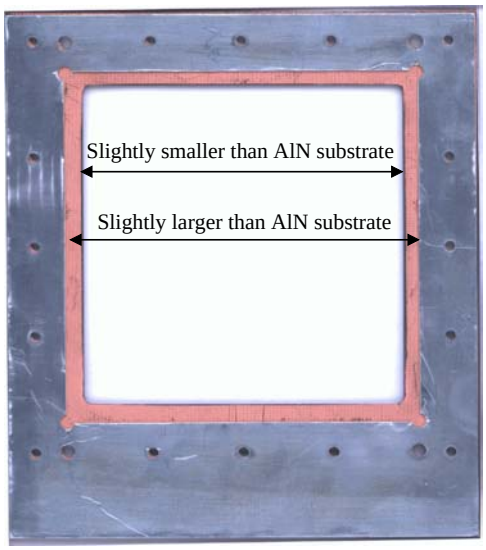

Figure 5.11. Mechanical support for the AlN substrate is achieved by placing the *TMM6* Window part [see Figure 5.10(c)] on top of the AlN support part [see Figure 5.10(d)].

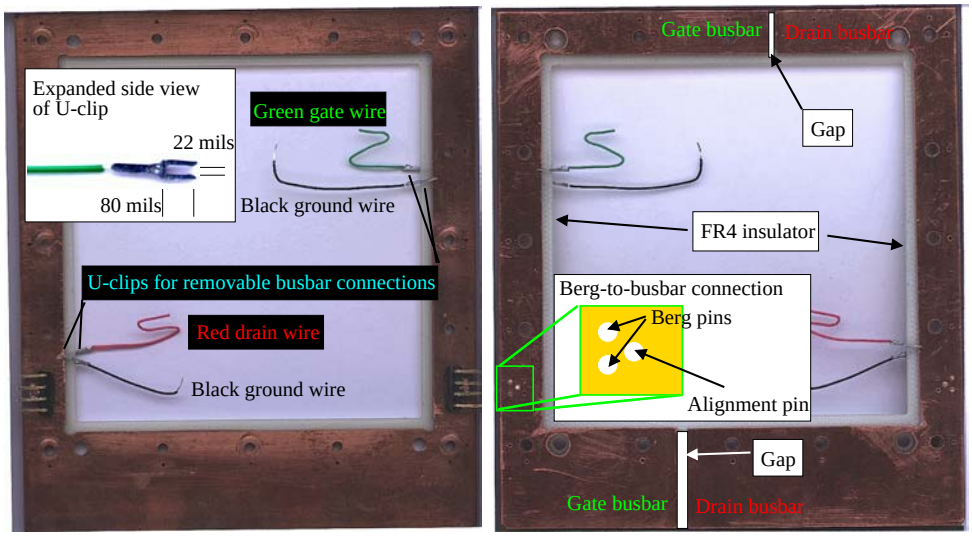

(a) Top down view (front side) (b) Bottom up view (backside)

Figure 5.12: The details of the Bias part are shown.

soldered to the bus bar as shown in the Berg-to-busbar schematic view in Figure 5.12(b). Similar attachment is made for the inner two pins of the drain *Berg* connector. The outer two pins of the *Berg* connectors are attached with solder to the ground busbar a shown in the lower expanded view of Figure 5.13.

The remainder of the QO amplifier assembly (Array C pictured in Figure 5.13) follows the same fabrication techniques described previously in Section 3.1. As shown in Figure 5.13, the bias wires, MMICs, and capacitors are connected to the AlN substrate with silver epoxy. The wire bonder is used to complete all RF electrical connections and the fabrication is complete.

Note that two passive arrays are also fabricated for calibration and measurement purposes. The first passive array (referred to as C9, for its 9 mm array spacing) is identical to Array C except that the MMICs are replaced with passive through lines. The second passive array (Array C7) has an array spacing of 7.5 mm. In total, one active (Array C) and two passive arrays (Arrays C9 and C7) are fabricated and will be characterized through measurements in the following section.

5.3 Performance characterization measurements

Results from experiments designed to characterize the performance of Array C are summarized in this section. In particular, measurements are performed to determine: single unit cell stability; interaction of the Gaussian beam with the slot array; polarizer loss; small signal gain of the array; saturated output power of the array; return loss of the QO array; the benefit of the Gaussian feed compared to the far-field feed; and the far-field radiation pattern.

5.3.1 Measured stability of the active unit cell QO amplifier array oscillation can occur if precautions in the design and fabrication have not been taken to prevent

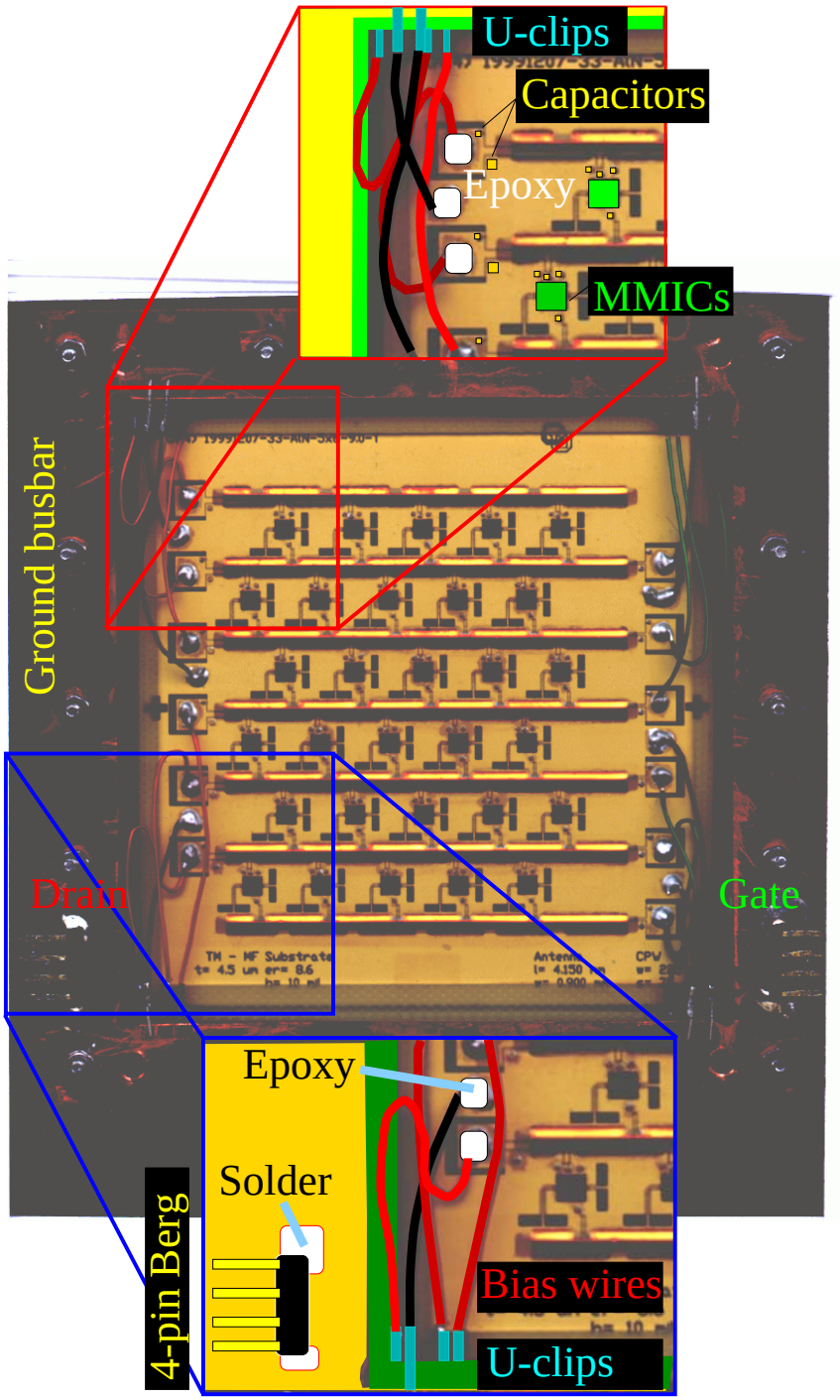

Figure 5.13. The final QO amplifier (Array C) is shown in its protective jig with all MMIC amplifiers, capacitors, and electrical connections completed. The outer two pins of each *Berg* connector are soldered to the ground busbar while the inner two pins are soldered to the backside (hidden) busbar. The U-clips for the drain wires attach to the lower (hidden in figure) busbar which are represented by short blue rectangles; similarly, the ground U-clips connect to the upper (visible in figure) busbar which are represented by longer blue rectangles.

RF feedback. To improve array stability, the bias shield was added to the design of Array C. In addition, during fabrication, four additional shorting capacitors per unit cell were mounted near each MMIC (recall Figure 5.13). It is difficult to predict at what bias level, if any, the MMIC will oscillate. Therefore, an experiment to examine unit cell stability is presented in this section.

A test array is fabricated identical to Array C except that only the center unit cell is populated with a single MMIC amplifier and four bias capacitors. The wire bond connections are made identical to the wire bonds in Array C. The test array bias is slowly increased to its maximum achievable level without oscillation. Note that the maximum rated drain voltage from the manufacturer is 6 V for the *Alpha* AA032P1-00 MMIC with a gate voltage of -1 V. To check for oscillations, an *HP 8565E* spectrum analyzer is connected to a horn located near the array. Table 5.1 summarizes the results of this experiment. The time

Table 5.1: The measured stability of a unit cell with a *Alpha* AA032P1-00 MMIC

V_{gs} [V]	V_{ds} [V]	I_{ds} [A]	Time [min]	Observations
-1.06	4	0.43	80	No oscillations
-1.09	4.63	0.427	60	No oscillations
-1.14	5.13	0.408	95	No oscillations
-1.09	5.13	0.425	25	No oscillations
-1.14	5.63	0.421	70	MMIC destroyed

column gives the number of minutes that the MMIC is biased at V_{ds}.

The MMIC failed after 5.5 hours with a drain voltage of 5.6 V. An oscillation was not observed with the spectrum analyzer; however, it is possible that either a short-lived destructive oscillation occurred before observation, or the MMIC was simply too hot at the 5.6 V bias. This experiment was repeated with another MMIC and failure again occurred near 6 V without oscillation. Based on the fact that two test MMICs both failed near 6 V without any observed oscillation, the maximum safe drain voltage is 5.5 V (0.5 V less than the published manufacturer specification) for stability and reliability of the unit cell.

5.3.2 Characterization of Array C utilizing a Gaussian lens feed system

The type of feed utilized to excite the QO amplifier affects both its gain and power performance. Based on prior near-field measurements (recall Table 4.2), the Gaussian lens system is a suitable alternative to the hard horn feed system (at least until the hard horn design can be improved). Therefore, the Gaussian feed system [12] is chosen to characterize the performance of Array C.

A schematic of the Gaussian lens system[3] used to characterize Array C is summarized in Figure 5.14(a) and an actual photograph is shown in (b). Two large lenses are placed symmetrically about the device under test (DUT). Each plano-convex hyperbolic lens is made from *Rexolite* with a diameter of 305 mm (12 inches). The distances d_{in} and d_{out} determine the waist diameter w at the surface of the DUT; for a 90 mm waist diameter (slightly larger than the area of Array C), $d_{\text{in}} = 166\,\text{mm}$ and $d_{\text{out}} = 566\,\text{mm}$. Within the waist diameter, the phase of the electric field is constant, but the magnitude theoretically varies 1 dB from the beam center to the edge of the array. The feed horns are corrugated and excite the fundamental Gaussian beam mode. A HP 8722 vector network analyzer is used to measure both the return loss and insertion loss of the DUT. Note that the insertion loss and return loss cannot be measured simultaneously because different calibrations are required for each. The 20 W external TWTA amplifier is typically used only during the large-signal power saturation measurements. The high power load serves to protect the vector network analyzer from high RF power levels. The use of the power meter in conjunction with the VNA improves the accuracy of the power measurement. Specifically, the ability of the VNA to ignore spurious reflections (time gating) improves the measurement of S_{21} while the power meter is best suited to measuring absolute power levels (P_{in}). From the power meter reading of P_{in} and the accurate S_{21} VNA measurement, the output power is calculated as $P_{\text{in}} + S_{21}$.

Before characterizing the QO amplifier, the interaction between the Gaussian beam

[3]The Gaussian beam system is located at Caltech (Pasadena, CA) in Dr. David Rutledge's lab. Dr. Blythe Deckman helped with the characterization of Array C.

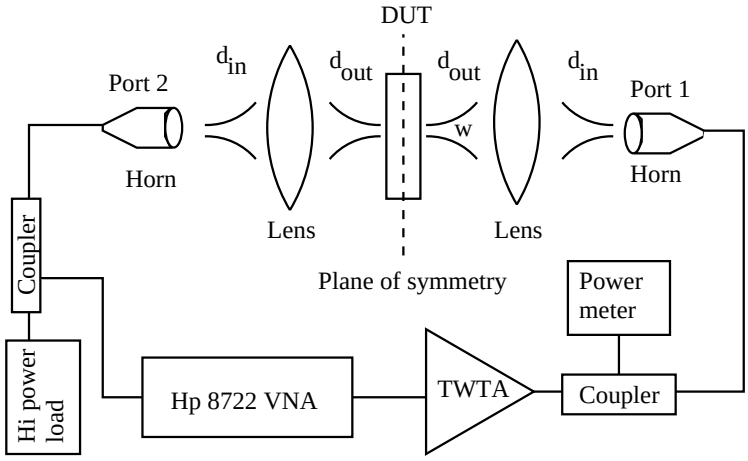

(a) Schematic

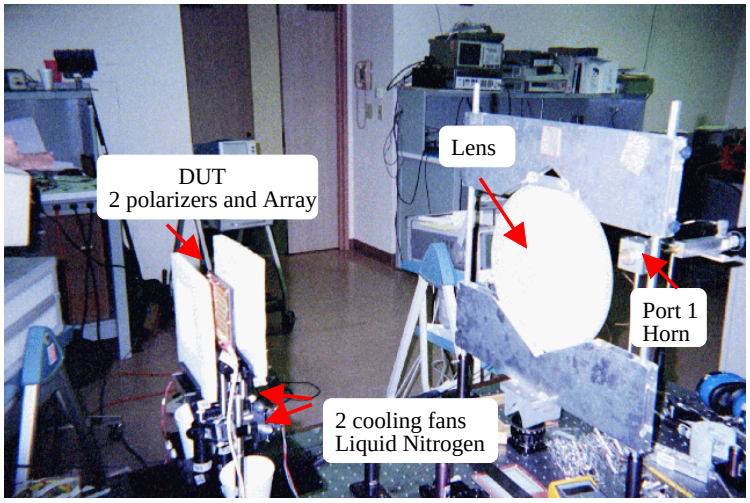

(b) Photograph

Figure 5.14. A schematic (a) and an actual photograph (b) of the Caltech Gaussian lens system used for characterizing Array C are shown.

and the array needs to be studied. A simple experiment is to measure the field variation at the aperture of the receive horn (port 2) with and without the DUT present using a small waveguide probe. In particular, the corrugated receive horn (port 2) is replaced with a small aperture probe on an adjustable stage. Figure 5.15 shows a plot of the measured probe power as a function of distance through the center (radial position of 0 mm) of the Gaussian beam with and without the DUT (Passive array C9). Based on the measured profile, it is observed that the array does not perturb the Gaussian beam significantly.

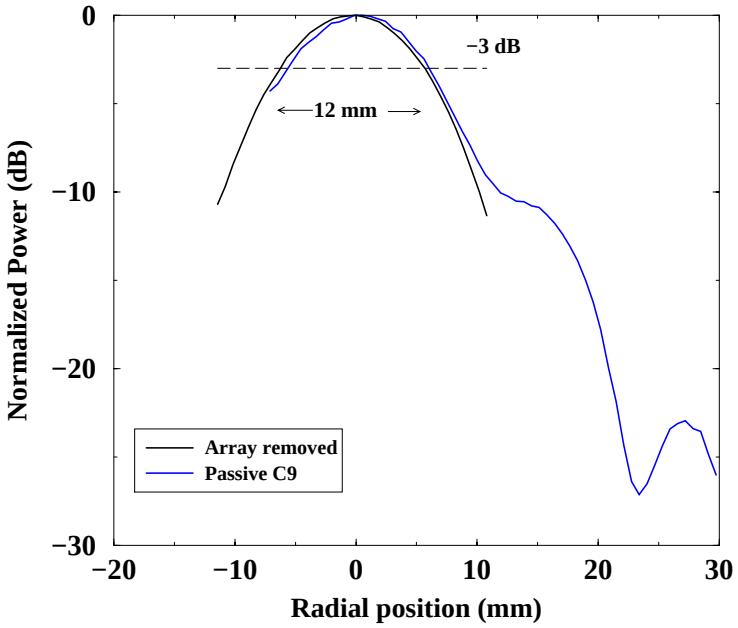

Figure 5.15. The normalized power is measured as a function of radial position with a small aperture probe located along the receive plane (plane where the port 2 receive horn is usually located).

The first measurement with the setup shown in Figure 5.14(a) is used to determine the polarizer loss. The DUT is a polarizer rotated 45° about the Gaussian beam propagation axis (perpendicular to the plane of symmetry thru the center of the Gaussian beam). Ideally, the insertion loss S_{21} for a 45° polarizer is -6 dB. The measurement of S_{21} shown in Figure 5.16 gives $S_{21} = -7.6$ dB at 31 GHz, a difference of 1.6 dB. Therefore, the measured polarizer loss is 0.8 dB at 31 GHz (lower than the 1.5 dB estimate using the far-field feed in

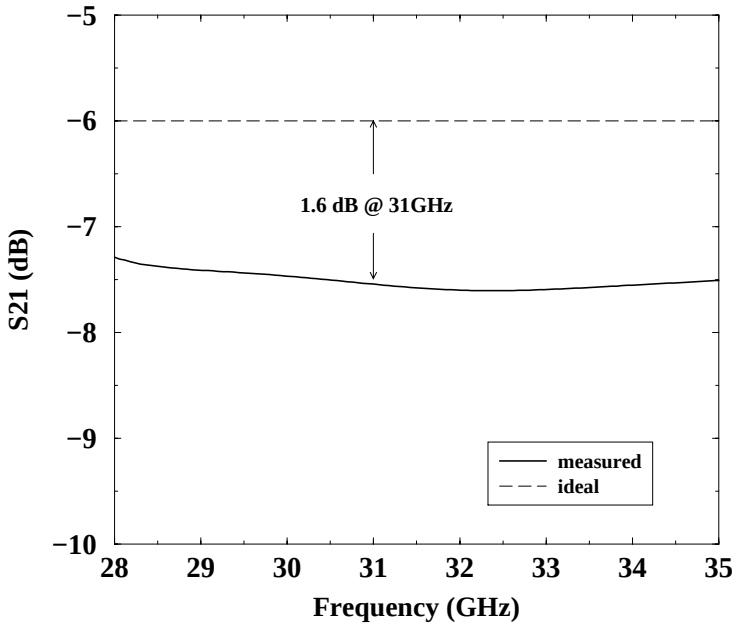

Figure 5.16. The measurement of polarizer loss is determined to be 0.8 dB at 31 GHz using the Gaussian lens setup. In particular, the insertion loss of a 45° polarizer is ideally -6 dB, but the measurement gives -7.6 dB.

Section 3.2.4).

To complete the performance characterization, Array C and the two polarizers are mounted in the Gaussian system as shown in Figure 5.14(b). Two cooling fans are positioned above two Styrofoam cups filled with liquid nitrogen beneath Array C to improve convective cooling. The positions of the polarizers and the DC bias levels are adjusted to achieve maximum amplifier gain (S_{21}). In particular, the active array bias levels are: $V_{gs} = -1\,\mathrm{V}$, $V_{ds} = 4.57\,\mathrm{V}$, and $I_{ds} = 7.91\,\mathrm{A}$. The bias is not increased any higher since the operating temperature is measured to be 96° C at this bias level. The small-signal measurement of S_{21} as a function of frequency is summarized in Figure 5.17. Note that the 20 W external amplifier is not used during the small-signal measurement. The small-signal performance parameters of Array C are summarized as follows: the small-signal gain is -8 dB; the gain over passive (G_a) is 3.7 dB; and the on-to-off ratio is 25.7 dB.

The large-signal power saturation measurement of Array C is completed with the

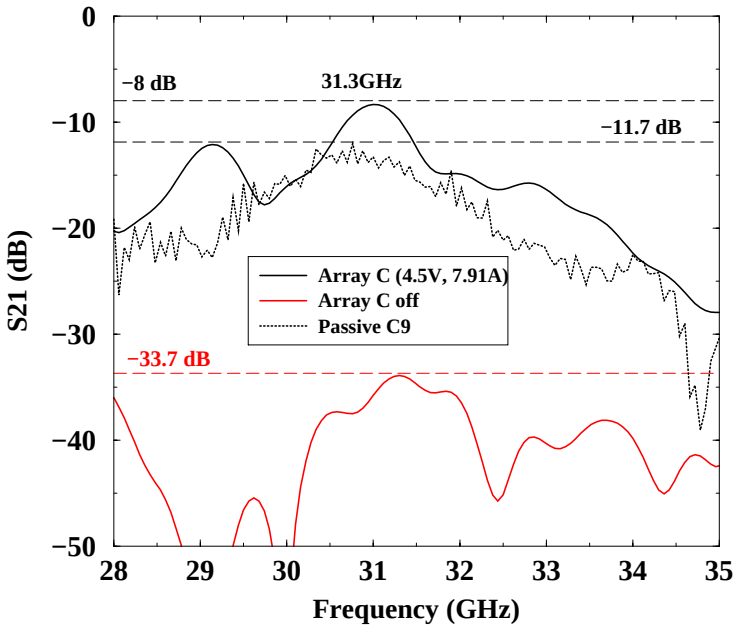

Figure 5.17. Small-signal measurement of S_{21} for the active Array C and the passive Array C9 in the Gaussian feed system.

addition of the 20 W external amplifier and is summarized in Figure 5.18. P_{out} is the output power radiated by the QO array and P_{in} is the power incident onto the surface of the array. The maximum output power of Array C is 28.4 dBm (690 mW) which occurred 3.3 dB above the linear region of the device with a large incident power of 38.1 dBm.

The large incident power required to saturate the QO amplifier array in the previous experiment suggests that a significant fraction of the incident power is scattered by the array. Unlike the far-field measurements of Chapter 3, the return loss (S_{11}) can be measured in the Gaussian system. A comparison of return loss between the arrays (C, C9, and C7) based on measurement is shown in Figure 5.19. The two arrays with the same array spacing of 9 mm (active Array C and passive Array C9) have nearly identical return loss as a function of frequency. Array C7 with the smaller 7.5 mm array spacing has 20 dB less return loss than the arrays with 9 mm array spacing. A significant decrease in return loss is achieved by decreasing the array spacing.

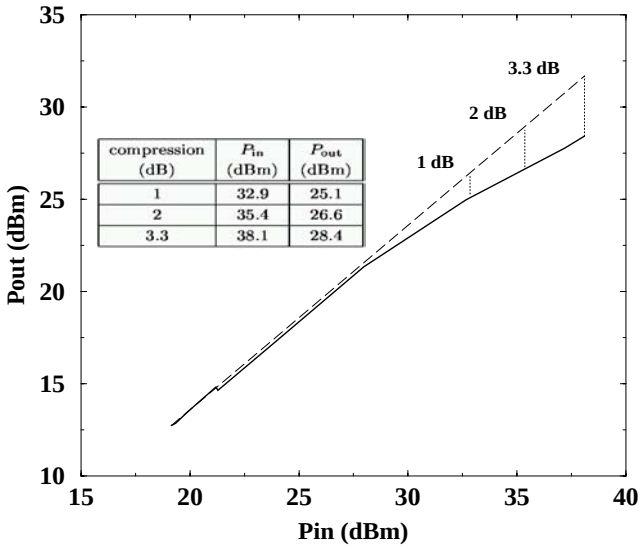

Figure 5.18. The power saturation measurement of QO array output power (P_{out}) as a function of incident power (P_{in}) is plotted for Array C at 31.3 GHz.

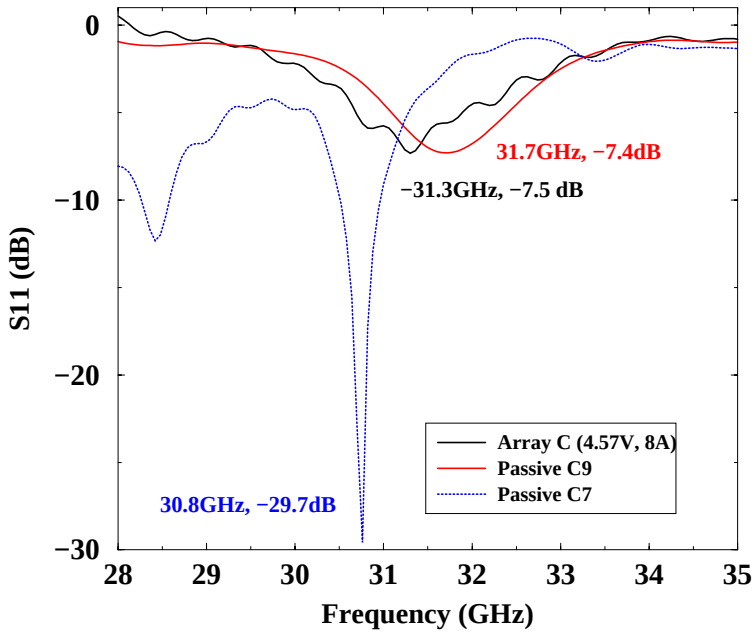

Figure 5.19. The return loss (S_{11}) is measured as a function of frequency for three arrays: active Array C; passive Array C9; and passive Array C7. Arrays C and C9 have the same 9 mm unit cell spacing, and C7 has a smaller 7.5 mm array spacing.

5.3.3 Characterization of Array C using the far-field feed system

Based on the Gaussian feed measurements, the amount of input power required to saturate Array C is greater than that which is possible with the far-field system. However, a comparison of small-signal measurements between the two feed systems (Gaussian and far-field) is possible. As in Chapter 3, S_{21} is measured and the results are plotted in Figure 5.20. The Gaussian

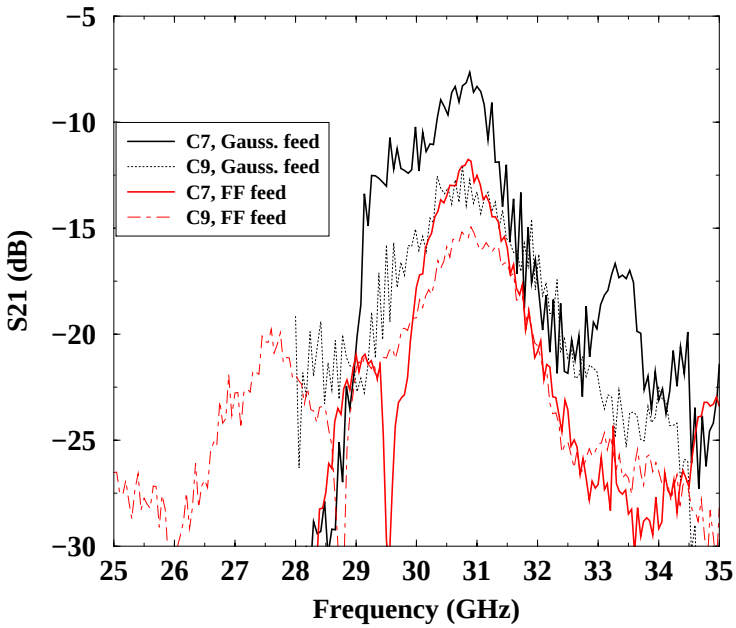

Figure 5.20. Small-signal gain measurements of the passive arrays (C9 and C7) are used to compare the effect of the Gaussian feed to the far-field feed.

feed improves the measured insertion loss of the passive arrays. In both the Gaussian and the far-field feed systems, the array with the 7.5 mm array spacing (C7) has at least 4 dB less insertion loss than the array with 9 mm array spacing (C9).

A small-signal pattern measurement using the far-field horn antennas is repeated for the active Array C. The measured E-plane pattern is compared with its theoretical pattern in Figure 5.21. The measured 3 dB beamwidth of 10.2° agrees with the theoretical value of 11.8°. The side lobe level is 3.4 dB higher than expected.

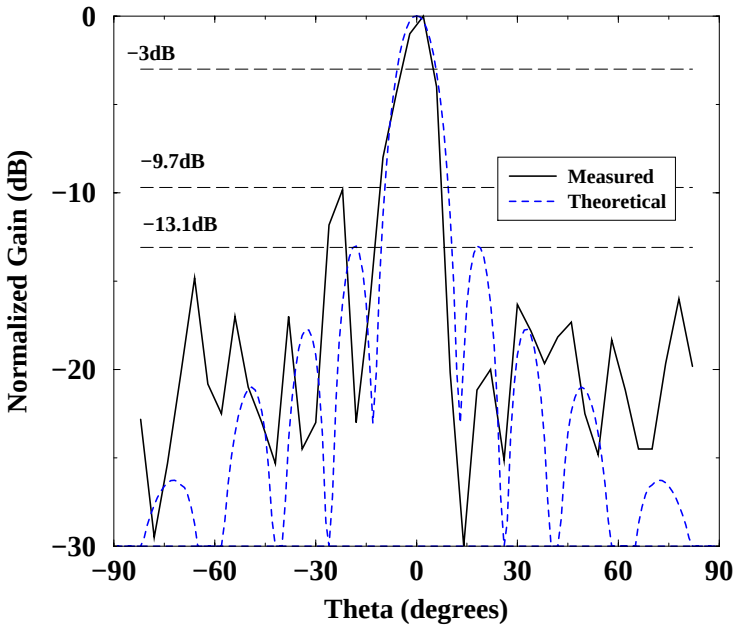

Figure 5.21. Active array E-plane pattern measurement is shown for Array C with a bias level of $V_{gs} = -1\,\mathrm{V}$, $V_{ds} = 4.70\,\mathrm{V}$, and $I_{ds} = 8.6\,\mathrm{A}$.

5.4 Discussion

Recall that the input and output ports of each *Alpha* AA032P1 MMIC in Array C are actually connected to the CPW transmission lines using $25.4\,\mu\mathrm{m}$ (1 mil) diameter gold bond wires. At Ka-band, these MMIC-to-CPW bond wire connections are highly inductive and tend to reduce the net gain contributed by each MMIC in the array. The MMIC-to-CPW bond wire has an inductance per unit length given by:

$$L' = \frac{\mu_0}{\pi} \ln(2h/a) \tag{5.1}$$

where a is the radius of the bond wire and h is the distance from the center of the bond wire to ground. Due to the bonding machine, the height of the bond wire is approximately $h \approx 0.2\,\mathrm{mm}$ with a total length of $l_{\mathrm{bond}} \approx 0.2\,\mathrm{mm}$. Consequently, $L' \approx 1.4 \times 10^{-9}\,\mathrm{H/mm}$ and the inductance of the MMIC-to-CPW bond wire is $L' \times l_{\mathrm{bond}} \approx 2.8 \times 10^{-10}\,\mathrm{H}$. The net gain of the MMIC including both the input and output MMIC-to-CPW bond wires is calculated at 31.3 GHz to be $S_{21} = 6.4\,\mathrm{dB}$ which is 4.4 dB lower than the ideal MMIC gain

of $S_{21} = 10.8\,\mathrm{dB}$. In comparison, the small-signal measurement (see Figure 5.17) determined the average gain contributed by the MMICs in Array C to be $G_a = 3.7\,\mathrm{dB}$ (7.1 dB lower than the ideal MMIC). Therefore, 4 dB of the measured 7.1 dB reduction in gain of Array C is due to fabrication of the MMIC-to-CPW transition.

A 4 dB improvement in gain is likely to be achieved by simply improving the MMIC-to-CPW bond wire transition. For Arrays A and B, the inductive transition was improved during fabrication with the addition of a second bond wire which reduced the transition inductance by half. However, the addition of a second bond wire is not possible for Array C due to the layout of the *Alpha* AA032P1 MMIC and difficulty with the wire bonder. Another solution might be to use a ribbon bonder, but one is not readily available. It is suggested that a shunt wire bond, placed optimally along the CPW, can be used to tune out the effects of the MMIC-to-CPW transition. Figure 5.22 shows a schematic of the circuit which includes the shunt wire bonds. Note that the inductance of the shunt bond wire is chosen to be the same as the inductance of the MMIC-to-CPW transition ($L_{\mathrm{shunt}} = L_{\mathrm{bond}} = 2.8 \times 10^{-10}\,\mathrm{H}$). The

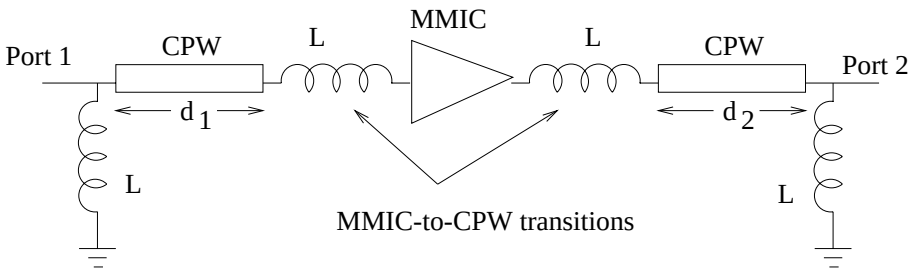

Figure 5.22. The shunt inductors are made using the wire bonder and are chosen to be of equal value to the inductance of the MMIC-to-CPW transition ($L = L_{\mathrm{bond}} = L_{\mathrm{shunt}}$). The locations ($d_1$ and d_2) of the shunt inductors are chosen to optimize S_{21}.

locations of the shunt bond wires are chosen such that S_{21} of the entire circuit is maximized at the operation frequency of Array C (31.3 GHz). With the addition of the shunt bond wires, the calculation yields $S_{21} = 9.8\,\mathrm{dB}$ with $d_1 = 1.1\,\mathrm{mm}$ and $d_2 = 0.82\,\mathrm{mm}$. Note that higher gain is not possible due to the short length of the CPW line connected to the output antenna (port 2). In principle, addition of shunt bond wires along the input and output

CPW lines can improve the gain of Array C. In practice, due to variations in MMIC-to-CPW bond wires between unit cells, it is difficult to precisely determine where to place each shunt bond wire optimally.

Other than the 4 dB decrease in gain due to the bond wires, an additional 3 dB reduction in gain remains undetermined. Based on the measurement of polarizer loss (recall Figure 5.16), each polarizer contributes 0.8 dB to the loss, and there are two polarizers in the system so the total polarizer loss is 1.6 dB. The final 1.4 dB loss is difficult to precisely determine. However, the final 1.4 dB loss is certainly due to a combination of output antenna radiation efficiency, antenna mismatch caused by the 50 μm tall bias line shield, the 90° CPW bend, and the MMIC gain decrease due to the high operating temperature of 96° C.

CHAPTER 6

SUMMARY AND CONCLUSIONS

"Science is facts; just as houses are made of stones, so is science made of facts; but a pile of stones is not a house and a collection of facts is not necessarily science."

– Henri Poincaire

6.1 Summary

The goal of this thesis is to design, fabricate, and characterize inexpensive Ka-band amplifier arrays with Watt level performance. Single-sided processing of aluminum nitride substrates and medium-power commercial MMICs are used to control both the material and manufacturing costs. The aluminum nitride substrate is chosen because of its high thermal conductivity which keeps the operating array temperature below the maximum safe limit ($\approx 100^\circ$ C). A total of four active Ka-band power-combining arrays are presented with varying degrees of success. The degree of success is determined by the design, the quality of fabrication, and the particular feed-collect configuration utilized.

A generalized model of spatial power combining is presented in Chapter 1 which demonstrates that the power combining efficiency of the spatial power combiner is independent of the number elements, unlike the corporate power combiner. Despite the benefit of independent power combining efficiency, the generalized model proves the importance of good feed design. The far-field feed is acceptable for characterizing the insertion loss of the array, but the far-field feed is inefficient at collecting all of the power radiated by the array.

As a consequence, both the near-field hard-horn and the Gaussian feeds are considered for comparison.

The practical details of spatial power combiner design involve more than just designing radiating elements and the array factor. In Chapter 2, the design of the amplifier array is explained in detail. CPW-fed slot antennas are used because of their high (13%) 2:1 VWSR bandwidth at 33 GHz and their ease of manufacture. The array layout is determined by the gain of the MMIC (19 dB), internal array mutual coupling, and the output radiation pattern of the array. The mutual coupling is calculated using the nearest-neighbor approximation with the aid of commercial electromagnetic CAD tools. In addition to thermal constraints, the DC bias network limits the practical size of the arrays to 36 elements due to ohmic loss, high DC power supply current, and the resulting DC voltage variations across the array.

An experimental study of array performance repeatability due to DC bias design and fabrication tolerances is summarized in Chapter 3. Three active arrays which utilize the 19 dB gain *Alpha* AA028P3-00 MMIC have slight variations in design and fabrication which lead to significant performance variations. In these arrays, the slot antennas and the array layout are identical. The first array has a highly resistive bias network which leads to one third of all MMICs functioning and poor RF performance. The second array decreases the DC bias variations with a thick supplementary copper bias line, and achieves 2.1 dB of small signal gain with a peak saturated output power of 316 mW. The third array also decreases the DC bias variations, but instead uses electroplated gold to increase the thickness of the bias line and decrease ohmic loss. Further effort is taken to remove RF from the bias lines with additional shorting capacitors and a dense set of wire bonds near the output antennas. As a result, the small-signal array gain improves to 6.5 dB and the third array achieves 513 mW (27.1 dBm) saturated output power. Based on the fact that the power from 36 *Alpha* AA028P3-00 MMICs are combined in free-space using 70% efficient slot antennas, the

saturated output power is expected to be 1.8 W (32.6 dBm).

Problems are discovered during the course of the characterization measurements. The hard-horn feeds, which are intended to improve feed efficiency, actually decrease the gain of the arrays by as much as 1.8 dB. The polarizers which are required to enforce unidirectional radiation of the slot antennas contribute 1.5 dB of loss. Each of the three arrays oscillate before the full gain of the MMIC is achieved which is indicative of higher levels of mutual coupling than expected from the numerical models. At most, the average gain contributed by the MMICs is measured to be 14 dB which is 5 dB less than the peak gain expected from a single MMIC.

A set of diagnostic measurements are performed to determine the specific causes of the observed problems based on near-field measurements (summarized in Chapter 4). The near-field measurements map the amplitude and phase of the electric field near the surface of the active array with high spatial resolution (as high as 8 μm possible). Based on the near-field measurements, it is determined that the DC bias lines still have RF coupling onto them and need to be better shielded to prevent array oscillations. The hard horn has a larger than expected electric field amplitude variation ($>$ 5 dB) across its aperture which contributes to the previously observed decrease in array gain; consequently, the hard horn needs to be redesigned. Until the hard horn is improved, the Gaussian lens system is required to uniformly excite the arrays with low feed loss. Overall, the diagnostic measurements suggest that modifications to the array design are possible which can improve its performance.

In an effort to improve the array performance, the amplifier array is redesigned in Chapter 5 with a new MMIC and bias network. The new *Alpha* AA032P1 MMIC has 14 dB gain and 25 dBm saturated output power (5 dB less gain and 8 dB more output power than the previously used *Alpha* AA028P3-00 MMIC). The fabrication of the array requires two additional photolithography steps to create the bias line shield. The bias line shield consists of a 50 μm thick electrical insulator (*Norland NR61*) and a thin copper conductor. The updated

array operates near the maximum safe temperature (100° C) without oscillation. With the Gaussian feed, the array achieves 7.1 dB less small-signal gain than expected (10.8 dB). 4.4 dB of the gain decrease is attributed to the fabrication of the MMIC-to-CPW transition which is highly inductive at Ka-band. It is suggested that the transition inductance can be decreased with the addition of shunt wire bonds (inductors) placed 1.1 mm and 0.8 mm away from the input and output ports of the MMIC along the CPW lines, respectively. Since this array achieves 691 mW (28.4 dBm) peak saturated output power, it is reasonable to expect that improvement of the MMIC-to-CPW transition could increase the output power of the array to 1.9 W (32.8 dBm).

In summary, the QO amplifiers presented in this thesis satisfy three of the original goals: low-cost, ease of manufacture, and thermal stability. The fourth and final goal of stable watt-level RF performance is satisfied, by a thin margin, with the demonstration of a $3000 half-Watt amplifier array on AlN with 6.5 dB of small-signal gain at 31 GHz. The fact that the observed peak power performance of each QO amplifier presented in this thesis is less than expected suggests the possibility of improvement in future QO amplifier designs.

6.2 Suggestions for future work

Based on observations gathered while completing this thesis, the pertinent issues which adversely affect the performance of QO amplifier arrays are now summarized to help improve future designs. Each polarizer contributes 1.5 dB loss to the net power output of the array. The quality of fabrication (overetch, inductive wire bonds, and tall-obtrusive bias line shield) decreases the quality of the antenna-to-MMIC match and thereby, contributes loss which is observed to be as high as 4.4 dB. The MMIC gain determines unit cell size, array stability, and array aperture efficiency. The thermal limit of the active array on AlN is reached with 30 *Alpha* AA032P1 MMICs. The insertion loss of each passive array is higher than expected considering that the individual CPW lines and slot antennas are confirmed

by measurement to be well matched.

Until recently, the best performance achieved from a QO Ka-band amplifier array was 4 W [4] utilizing the hard-horn feed. Within the past month, a significant increase to 24 W has been achieved [48] by the same research group. In that work, some of the issues previously mentioned are alleviated and the result is improved power performance, but at the expense of increased fabrication difficulty and cost. Mutual coupling is reduced by isolating input and output patch antennas (uni-directional) on opposite sides of a thick metal heat carrier. This approach has two benefits: no need for lossy polarizers and better thermal management using the thick metal carrier. Unlike the arrays presented in this thesis, their arrays can be scaled beyond 30 elements, due to the thermal properties of the thick metal carrier, to achieve higher power levels (tens of Watts) than are possible with a thin AlN substrate.

The approach taken in [48] yields amplifier arrays with impressive power output levels, but neglects the need for low-cost easily-manufactured Ka-band amplifier arrays. Therefore, improvement of the low-cost AlN amplifiers presented in this thesis is still a feasible approach for watt-level power levels, provided that the pertinent issues which adversely affect performance are alleviated in future designs. This thesis ends with a summary of four problematic issues which need to improve in future AlN QO amplifier designs and presents suggestions to alleviate them.

(1) The measured polarizer loss of 1.5 dB is unacceptably large. The obvious solution to polarizer loss is to not use any polarizers, but this would require the abandonment of slot antennas (bidirectional radiators) in favor of patch antennas (unidirectional radiators). One problem with this is that the patch antenna has a lower bandwidth than the slot antenna which makes the patch array more sensitive to variations in fabrication. Also, without polarizers, the ability to tune the array during the measurement stage is not a trivial consideration. However, if the patch array is well

designed and carefully manufactured, then the issues of bandwidth and tunability are not a dominant concern and the benefit of removing the large polarizer loss is worth the added effort.

(2) The fabrication of the MMIC-to-CPW transition is critical to the performance of the array. As much as 4.4 dB loss is attributed to this transition.

- One solution is to use a ribbon bonder, instead of the wire bonder, since the ribbon bonds have lower inductance.
- Another, more immediate, solution is to use shunt wire bonds located on both sides of the MMIC which can theoretically improve S_{21} of the array (recall Section 5.4).

(3) In an effort to improve the return loss of the array and decrease the insertion loss, the unit cell size should be chosen to be as close to the effective area, A_{eff}, of the unit cell antenna as is possible. By choosing the unit cell size in such a manner, the aperture efficiency of the array will increase based on the theory presented in Section 2.5.

- Figure 6.1 demonstrates, by experiment, the improvement in S_{21} that is possible when both the unit cell size is decreased and the number of unit cells is increased in a passive array on *Rogers TMM6*.
- The use of highly directive antennas could increase A_{eff} and the unit cell size.
- The isolation between input and output antennas needs to be improved to enhance array stability. In [48], the input and output antennas are separated by a thick ground plane and are connected by a through coupler which naturally enhances isolation. Perhaps, the choice of using slot antennas located on the same side of the substrate to simplify fabrication allows too much coupling and needs to be abandoned.

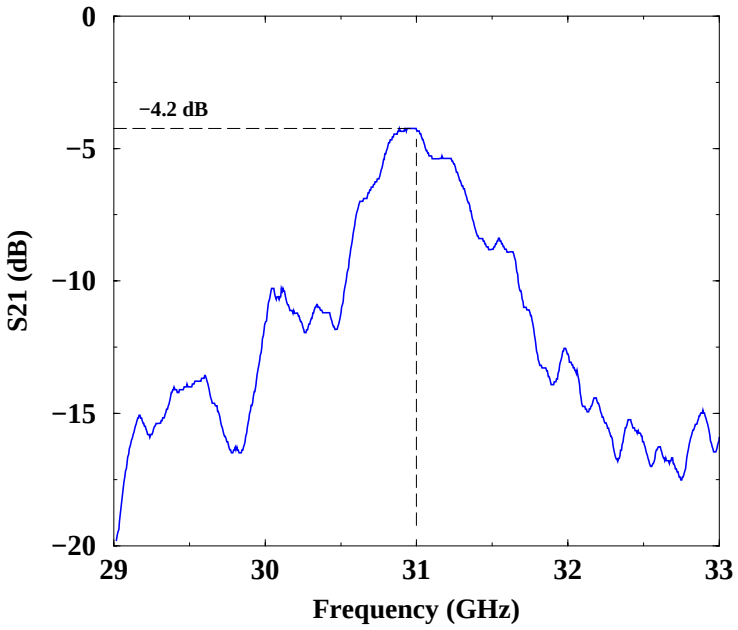

Figure 6.1. S_{21} is measured as a function of frequency for a passive array of CPW-fed slot antennas on 381 μm thick *Rogers TMM6* substrate. A 7×7 rectangular lattice with an 8 mm array spacing (square unit cell) is utilized.

- Rather than increasing the unit cell size until the coupling is below the maximum gain of the MMIC, the MMIC should be chosen such that its gain is less than the coupling in an array with unit cell size of A_{eff}. In other words, rather than increasing the unit cell size to decrease coupling, the unit cell should be small and the MMIC should be chosen accordingly (probably with 8 to 10 dB of gain).

(4) To reduce dependence on the computer models, the probe station could be used (with unidirectional antennas) to directly measure coupling and improve unit cell design.

BIBLIOGRAPHY

[1] Robert A. York, "Quasi-optical power combining," in *Active and Quasi-optical arrays for solid-state power combining*, Robert A. York and Zoya B. Popović, Eds., chapter 1. John Wiley, New York, 1997.

[2] D. Staiman, M. E. Breese, and W. T. Patton, "New technique for combining solid-state sources," *IEEE J. Solid-State Circuits*, vol. SC-3, pp. 238–243, Sept. 1968.

[3] J. Hubert, J. Schoenberg, and Z. Popović, "High-power hybrid quasi-optical Ka-band amplifier design," *IEEE MTT-S International Microwave Symp. Digest*, pp. 585–588, May 1995.

[4] John Hubert, Lee Mirth, Sean Ortiz, and Amir Mortazawi, "A 4-watt Ka-band quasi-optical amplifier," *IEEE MTT-S International Microwave Symp. Digest*, June 1999.

[5] C. M. Liu, E. A. Sovero, W. J. Ho, J. A. Higgins, M. P. De Lisio, and D. B. Rutledge, "Monolithic 40-GHz 670-mW HBT grid amplifier," *IEEE MTT-S International Microwave Symp. Digest*, pp. 1123–1126, June 1996.

[6] M. P. De Lisio, S. W. Duncan, D. W. Tu, S. Weinreb, C. M. Liu, and D. B. Rutledge, "A 44-60 GHz monolithic pHEMT grid amplifier," *IEEE MTT-S International Microwave Symp. Digest*, pp. 1127–1130, June 1996.

[7] E. A. Sovero, J. B. Hacker, J. A. Higgins, D. S. Deakin, and A. L. Sailer, "A Ka-band monolithic quasi-optic amplifier," *IEEE MTT-S International Microwave Symp. Digest*, pp. 1453–1456, June 1998.

[8] Constantine A. Balanis, *Antenna Theory*, pp. 73–78, 736–767, John Wiley & Sons, Inc, New York, 1997.

[9] E.F. Kuester, "Supplementary notes on antennas," University of Colorado, Boulder, Course ECEN 5134, 1997.

[10] George B. Arfken and Hans J. Weber, *Mathematical Methods for Physicists*, chapter 3, pp. 188–190, Academic Press, San Diego, 4 edition, 1995.

[11] S.C. Ortiz, T. Ivanov, and A. Mortazawi, "A CPW-fed microstrip patch quasi-optical amplifier array," *IEEE Transactions on Microwave Theory and Techniques*, vol. 48, pp. 276–280, Feb. 2000.

[12] Blythe C. Deckman, *Active Quasi-Optics and Measurements*, PhD thesis, California Inst. of Tech., Pasadena, CA, 2000.

[13] Stein Hollung, *Quasi-optical transmit/receive lens amplifier arrays*, PhD thesis, Univ. of Colorado, Boulder, CO, 1998.

[14] Nai-Shuo Cheng, Angelos Alexanian, Michael G. Case, and Robert A. York, "20 watt spatial power combiner in waveguide," in *1998 IEEE MTT-S International Microwave Symp. Digest*, Baltimore, MD, June 1998, pp. 1457–1460.

[15] Maha A. Ali, Sean Ortiz, Toni Ivanov, and Amir Mortazawi, "Analysis and measurement of hard horn feeds for the excitation of quasi-optical amplifiers," *IEEE MTT-S International Microwave Symp. Digest*, pp. 1469–1472, June 1998.

[16] K. C. Gupta, "Computer-aided design of microstrip antennas," University of Colorado, Boulder, Course Notes, pp. 27-28, 54-57, 1993.

[17] E.W. Bryerton, M.D. Weiss, and Z. Popović, "Efficiency of chip-level versus external power combining," *IEEE Transactions on Microwave Theory and Techniques*, vol. 47, no. 8, pp. 1482–1485, Aug. 1999.

[18] N. J. Kolias and R. C. Compton, "Thermal management for high-power active amplifier arrays," *IEEE Transactions on Microwave Theory and Techniques*, vol. 44, no. 6, pp. 963–966, June 1996.

[19] W. Batty, A.J. Panks, R.G. Johnson, and C.M. Snowden, "Electrothermal modeling and measurement for spatial power combining at millimeter wavelengths," *IEEE Transactions on Microwave Theory and Techniques*, vol. 47, no. 12, pp. 2574–2585, Dec. 1999.

[20] Adrian Bejan, *Heat Transfer*, p. 16, John Wiley & Sons, Inc, New York, 1993.

[21] H.G. Booker, "Slot aerials and their relation to complimentary wire aerials (Babinet's Principle)," *J. IEE*, vol. Pt. IIIA,(4), no. 93, pp. 620–626, 1946.

[22] Huan-Shang Tsai and Robert A. York, "FDTD analysis of CPW-fed folded-slot and multiple-slot antennas on thin substrates," *IEEE Transactions on Antenna and Propagation*, vol. 44, no. 2, pp. 217–226, Feb. 1996.

[23] H. S. Tsai, M. J. Rodwell, and R. A. York, "Planar amplifier array with improved bandwidth using folded-slots," *IEEE Microwave and Guided Wave Letters*, vol. 4, no. 4, pp. 112–114, Apr. 1994.

[24] E.F. Kuester and D.C. Chang, "Theory of waveguides and transmission lines," University of Colorado, Boulder, Course Notes for ECEN 5144, pp. 193-194, 1998.

[25] T.W. Nuteson, G.P. Monahan, M.B. Steer, K. Naishadham, J.W. Mink, K.K. Kojucharow, and J. Harvey, "Full-wave analysis of quasi-optical structures," *IEEE Transactions on Microwave Theory and Techniques*, vol. MTT-44, pp. 701–710, May 1996.

[26] D.E.J Humphrey and V.F. Fusco, "A mutual coupling model for microstrip patch antenna pairs with arbritrary orientation," *Microwave and Optical Technology Letters*, vol. 18, no. 3, pp. 230–233, June 1998.

[27] M. Malkomes, "Mutual coupling between microstrip patch antennas," *Electronic Letters*, vol. 18, pp. 520–522, June 1982.

[28] R.P. Jedlicka, M.T. Poe, and K.R. Carver, "Measured mutual coupling between microstrip patch antennas," *IEEE Transactions on Antenna and Propagation*, vol. AP-29, pp. 147–149, Jan. 1981.

[29] T. Huynh, K.F. Lee, and S.R. Chebolu, "Mutual coupling between rectangular microstrip patch antennas," *Microwave and Optical Technology Letters*, vol. 5, pp. 572–576, Oct. 1992.

[30] T. Marshall, M. Forman, and Z. Popović, "Two Ka-band quasi-optical amplifier arrays," *IEEE Transactions on Microwave Theory and Techniques*, vol. 47, no. 12, pp. 2568–2573, Dec. 1999.

[31] Richard C. Jaeger, *Introduction to Microelectronic Fabrication*, chapter 2, Addison-Wesley Publishing Company, New York, 1993.

[32] Mark Gouker, "Toward standard figures-of-merit for spatial and quasi-optical power-combined arrays," *IEEE Transactions on Microwave Theory and Techniques*, vol. 43, no. 7, pp. 1614–1617, July 1995.

[33] Zoya Popović and Amir Mortazawi, "Quasi-optical transmit/receive front ends," *IEEE Transactions on Microwave Theory and Techniques*, vol. 46, no. 11, pp. 1964–1975, Nov. 1998.

[34] K. Yang, G. David, S. Robertson, J.F. Whitaker, and L.P.B. Katehi, "Electro-optic mapping of near field distributions in integrated microwave circuits," *IEEE Transactions on Microwave Theory and Techniques*, vol. 46, no. 12, pp. 2338–2343, Dec. 1998.

[35] K. Yang, G. David, W. Wang, T. Marshall, M. Forman, L.W. Pearson, Z. Popović, L.P.B. Katehi, and J.F. Whitaker, "Electro-optic field mapping of quasi-optic power-combining arrays," in *Ultrafast Electronics and Optoelectronics Conference*, Technical Digest Series, Optical Society of America, Washington DC, 1999, pp. 30–32.

[36] K. Yang, T. Marshall, M. Forman, J. Hubert, L. Mirth, Z. Popović, L.P.B. Katehi, and J.F. Whitaker, "Active-amplifier-array diagnostics using high-resolution electro-optic field mapping," *submitted to IEEE Transactions on Microwave Theory and Techniques*, Jan. 2000.

[37] J. Nees and G. Mourou, "Noncontact electrooptic sampling with a GaAs injection laser," *Electronic Letters*, vol. 22, pp. 918–919, Aug. 1986.

[38] J.A. Valdmanis, "1-THz-bandwidth prober for high-speed devices and integrated circuits," *Electronic Letters*, vol. 23, pp. 1308–1310, Oct. 1987.

[39] S.L. Huang, C.H. Lee, and H.L.A. Hung, "Real-time linear time-domain network analysis using picosecond photoconductive mixer and sampler," *IEEE Transactions on Microwave Theory and Techniques*, vol. 43, no. 6, pp. 1281–1289, June 1995.

[40] T. Pfeifer, H.M. Heilinger, T. Löffler, C. Ohlhoff, C. Meyer, G. Lüpke, H.G. Roskos, and H. Kurz, "Optoelectronic on-chip characterization of ultrafast devices: measurement techniques and applications," *IEEE Journal of Quant. Elect.*, vol. 2, no. 3, pp. 586–604, Sept. 1996.

[41] H.J. Cheng, J.F. Whitaker, K.J. Herrick, N. Dib, L.P.B. Katehi, and J.L. Coutaz, "Electro-optic probes: high-permittivity crystals vs. low-permittivity polymers," in *Ultrafast Electronics and Optoelectronics*, OSA Technical Digest Series, Optical Society of America, Washington DC, 1995, vol. 13, pp. 128–130.

[42] X. Wu, D. Conn, J. Song, and K. Nickerson, "Invasiveness of $LiTaO_3$ and GaAs probes in external E-O sampling," *IEEE J. Lightwave Tech.*, vol. 11, pp. 448–454, Mar. 1993.

[43] K. Yang, G. David, J.G. Yook, I. Papapolimerou, L.P.B. Katehi, and J.F. Whitaker, "Electrooptic mapping and finite-element modeling of the near-field pattern of a microstrip patch antenna," *IEEE Transactions on Microwave Theory and Techniques*, vol. 48, no. 2, pp. 288–294, Feb. 2000.

[44] R. Gonzalo, P. Maagt, and M. Sorolla, "Enhanced patch-antenna performance by suppressing surface waves using photonic-bandgap substrates," *IEEE Transactions on Microwave Theory and Techniques*, vol. 47, no. 11, pp. 2131–2138, Nov. 1999.

[45] E. Rius, J.P. Coupez, S. Toutain, C. Person, and P. Legaud, "Theoretical and experimental study of various types of compensated dielectric bridges for millimeter-wave coplanan applications," *IEEE Transactions on Microwave Theory and Techniques*, vol. 48, no. 1, pp. 152–156, Jan. 2000.

[46] E.A. Soliman, S. Brebels, G. Vandenbosch, and E. Beyne, "Antenna arrays in MCM-D

technology fed by coplanar CPW networks," *IEEE Transactions on Microwave Theory and Techniques*, vol. 48, no. 6, pp. 1065–1068, June 2000.

[47] T.J. Gillespie, C.H. Marshall, M. Contreras, and J. Keane, "Copper indium diselenide (CIS) process, control and manufacturing," *Solar Energy Materials and Solar Cells*, vol. 59, pp. 27–34, 1999.

[48] Sean Ortiz, John Hubert, Lee Mirth, Erich Schlecht, and Amir Mortazawi, "A 25 Watt and 50 Watt Ka-band quasi-optical amplifier," in *IEEE MTT-S International Microwave Symp. Digest*, Boston, MA, June 2000.